

University of Naples

“Federico II”

Department of Industrial Engineering



PhD school in

Aerospace, Naval and Total Quality Management Engineering

Cycle XXVI

***“COSMO-SkyMed polarimetric data for soil moisture  
retrieval: capability of SAR data for landslide monitoring”***

*Candidate*

Eliana Barbera

*Tutors*

Prof. A. Moccia

Eng. F. Caltagirone

*Coordinator*

Prof. L. de Luca

Academic year

2013- 2014

# CONTENTS

<b>INTRODUCTION</b> .....	4
<b>CHAPTER 1 Synthetic Aperture Radar</b> .....	6
1.1 Synthetic Aperture Radar principles.....	6
1.1.1 Sar data acquisition.....	7
1.1.2 SAR penetration depth.....	8
1.2 SAR System Parameters.....	9
1.3 SAR Equations .....	13
1.4 SAR Complex Images .....	17
1.5 Complex Coherence.....	20
1.6 Radar backscattering coefficient.....	21
1.7 Speckle.....	22
1.8 Polarisation and surface scattering .....	24
1.8.1 Polarimetric phase information .....	24
1.9 COSMO-SkyMed SAR System .....	25
<b>CHAPTER 2 Properties of soil surfaces</b> .....	32
2.1 Surface Roughness.....	32
2.2 Soil Moisture and dielectric constant.....	35
2.2.1 Soil Moisture.....	35
2.2.2 Dielectric constant.....	38
2.3 Soil moisture retrieval techniques.....	39
2.3.1 The Dubois Model.....	40
2.3.2 The Water-cloud Model.....	42
<b>CHAPTER 3 Study area and experimental results</b> .....	44
3.1 Data set: Description .....	44
3.2 Data set: Processing and Analysis .....	49
3.2.1 Data set processing .....	49
3.2.2 Data set Analysis.....	56
3.2.3 Data set Coherence Analysis.....	59
3.3 Soil moisture maps.....	63
3.4 Study on radar sensitivity .....	70
<b>CHAPTER 4 Further Developments</b> .....	89
4.1 Slope stability model .....	89

<i>4.2 COSMO-SkyMed Seconda Generazione</i> .....	93
<b>CONCLUSIONS</b> .....	96
<b>REFERENCES</b> .....	100

## **INTRODUCTION**

*In the last years the interest in the study and monitoring of the Earth has been gradually growing, and many institutions have planned missions for these purposes.*

*Synthetic Aperture Radar (SAR) is one of the most promising approaches to acquire images of every part of the world in short time. The characteristics that make the SAR a very powerful instrument are its capability to operate independently of weather conditions, at day and night, and to reach target that are inaccessible to ground measurement.*

*There are many fields of interest for Earth Observation (both civilian and military), such as the detection and surveillance of ships or marine traffic, monitoring of agricultural fields, study of the winds in tropical storms and study of oceanic current, monitoring the damage caused by earthquakes, floods, tsunamis, inundation or other natural disasters, and more over.*

*Natural disasters, in particular landslides, frequently affect our country, Italy. The hydrogeological risk is very high during rainy periods, and a space observation can be useful as support to civil protection in times of emergency, but also in the next phase of damage assessment. The knowledge of soil moisture behaviour is critical in different environmental and land activities; for example is the basis for prediction of river floods, rainfalls, avalanches and landslides. Given the link between specific soil parameters (such as moisture and surface roughness) and permittivity, it is possible to accurately measure these parameters with SAR data, starting from the measurements of the dielectric constant. The main problem is to separate the individual effects of the various parameters on the backscattered signal. However, this is possible using polarimetric data, in fact this data permits to minimize the effect of vegetation and surface roughness by using polarization ratios: combining cross- and co- polarizations ratios it can be possible to determine the soil moisture regardless of surface roughness.*

*This research is funded by the Italian Space Agency in the framework of Cosmo-SkyMed Seconda Generazione project; it is focused on soil moisture retrieval by using polarimetric data. I analysed some Cosmo-SkyMed first generation polarimetric data (provided by courtesy of Italian Space Agency), in order to demonstrate the capability of the new generation of high resolution SAR system, and to suggest some possible upgrades or improvements for the new generation of ASI satellites.*

*So, in the following chapter the operating principles of SAR are presented; in the second chapter I*

*introduce the properties of soil surfaces, with particular attention to the soil moisture parameter and the model useful to its retrieval. The third chapter is devoted to explain the data set available and the analysis done in order to evaluate a soil moisture map; in the forth some possible further developments will be proposed for the new generation of ASI SAR system. The conclusions and the obtained results are discussed in the last section.*

## CHAPTER 1

### *Synthetic Aperture Radar*

Spaceborne imaging radars started in the late 1960's and 1970's with a series of missions orbiting around the Earth. The beginning of remote sensing opened several new fields on observing, studying and monitoring planetary surface and environments. For this purpose Synthetic Aperture Radar (SAR) have been widely used in the last decades; they operate in the active microwave region (see Fig. 1.1) acquiring physical and electrical information of the target by analysing the reflected waves of electromagnetic field.

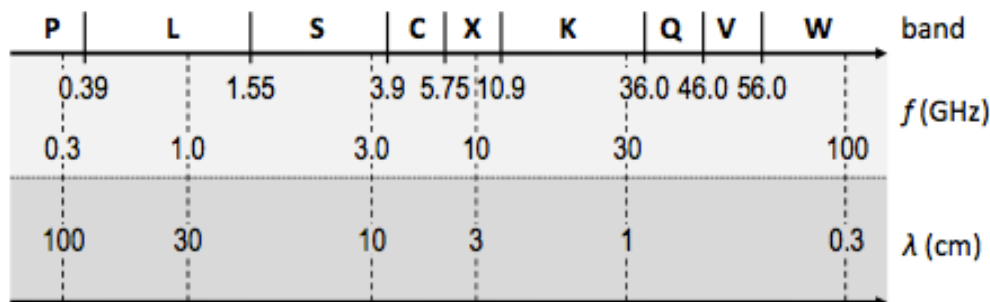


Fig. 1.1: Section of the microwave electromagnetic spectrum.

In the Earth observation the microwave SAR sensors provide the capability of acquiring images not affected by weather conditions thanks to the long wavelength adopted; moreover, since SAR are active sensors (i.e. the sensor illuminates the target), can take image in daylight or at night.

This chapter is intended to recall the basic principles of Synthetic Aperture Radars.

### **1.1 Synthetic Aperture Radar principles**

The radar sensors acquire images in two dimensions, first illuminating the target with a microwave pulse, and then receiving the backscattered signal.

Some radars use the same sensor to transmit and receive the microwave signal; this case is known as monostatic configuration. Other radars use spatially separated transmitter and receiver; the receiver collects the backscattered signal sent by the transmitter to illuminate the scene: this scenario is called bi- or multi- static configuration (Skolnik M.I., 1981).

A Sar image can be described by a 3-dimensional reflectivity function of the density distribution of scattering targets. This 3-dimensional reflectivity function, projected in a two-dimensional range-azimuth image, depends on the frequency, the imaging geometry and the polarization of the

acquisition. Hence these parameters characterize the information held in the SAR images (Henderson F.M. and Lewis A.J., 1998).

The microwave spectrum, in which SAR sensors operate, ranges between 0.3GHz and 100GHz (as reported in Fig. 1.1); civil observations usually operate at P-, L-, S-, C-, or X- band.

The SAR systems can also acquired polarized images: they use a linearly polarized antennas in a single-, dual- or quad- polarimetric mode, acquiring horizontal or vertical polarized backscattered signal.

It is easy to understand that in a single-mode the signal is transmitted in a single polarization and received in the same polarization. In other way the dual-pol mode (or the quad-pol mode) receive the signal at two (or four) polarizations. Informations acquired through the polarimetric modes are held into the scattering matrix.

### 1.1.1 Sar data acquisition

SAR sensor illuminates a surface on the Earth in a side-looking geometry (see Fig. 1.2).

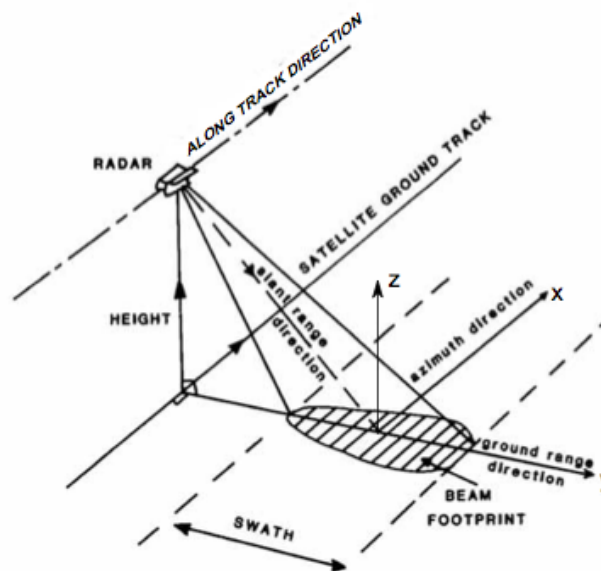


Fig. 1.2: SAR data acquisition scenario.

The sensor move along a path at an altitude  $H$  above a reference plane  $(x,y)$ , and transmits at the same time a pulse over the footprint of the antenna's illumination, with a rate given by the Pulse Repetition Frequency (PRF) and receive the echoes of each pulse scattered back from the target.

The SAR receiver separates the single echoes within the echoes flow, each reconnecting to the specific transmitted pulse. Once separated, the single echoes are arranged in a 2D matrix in the processing phase, which has the two-way signal time and the pulse number for coordinates. The pulse number is referred to satellite position along its flight path, the delay to slant range.

The typical pulse's wavelengths are about 3cm (X-band), 6cm (C-band), 9cm (S-band) and 24cm (L-band), while the PRF are in the range of (1-19) kHz.

Each pulse is transmitted pass through the swath with the velocity of light, and at the same time the scene is scanned in the along-track direction at the speed of the sensor. So, there are two different scanning mechanisms, which differ by some order of magnitudes; then these two mechanisms can be treated as independent (start-stop approximation). As a consequence it can be possible to arrange the received echoes in a raw data matrix, that has for coordinates R (distance of the scatterer from the SAR) and x (azimuth, position of the scatterer along the sensor path).

In the range direction the radar principles govern the characteristics of the image, and so, the duration of the transmitted pulse give the range resolution. On the other hand the azimuth resolution is limited to the antenna footprint size, that is given by  $R\lambda/L$  and is of order of several km (L represents the length of the physical antenna in the direction of flight – order of 10m). The azimuth spatial frequency bandwidth, instead, is of order of  $2/L$ .

In this way it can be able to concentrate raw data in an azimuth resolution of half physical antenna length, independently of range, wavelength and sensor velocity.

### **1.1.2 SAR penetration depth**

Once of the main features of the radar system is the ability, of the microwave radiation, to penetrate the material. This capability is referred to the penetration depth that is a function of the frequency, the moisture content, the density and also the polarization (Ulaby F.T. et al. 1981-A; Hajnsek I. et al., 2003).

For these reasons, on the one hand, a short wavelength (i.e. X- or C- band) will interact with the first layer in a dry soil, and hence the received information will be related only with this part of the surface. The other way, lower frequencies (as L- or P- band) permits to penetrate deeper in soil. Usually this variation in penetration depth is the order of tenths of the wavelength up to half a wavelength.

Therefore, as demonstrated by Ulaby F.T. (1981-B) the penetration depth decreases at frequencies from 1.3GHz to 10GHz, when the moisture content increases; on the contrary the penetration depth at frequencies  $>4$ GHz decreases quickly below 1cm if increases moisture content.

If the observed scene presents a vegetation canopy, the penetration depth will depend also from some parameters related to the vegetation part: the geometry of canopy, the dielectric properties of the vegetation and also the volume of vegetation fraction. Some studies have demonstrated that the penetration depth, in case of low vegetation water content (as in the case of crops before the harvest), is higher than the case with green and luxuriant vegetation (Ferrazzoli P. et al., 1992).

## 1.2 SAR System Parameters

Basic geometry of a SAR is represented by a platform moving with velocity  $V$  that carries a side-looking radar antenna, at altitude  $H$ , which illuminates the target on the surface with an electromagnetic pulse (Fig. 1.3), and whose aperture aims to perpendicular respect with the flight direction.

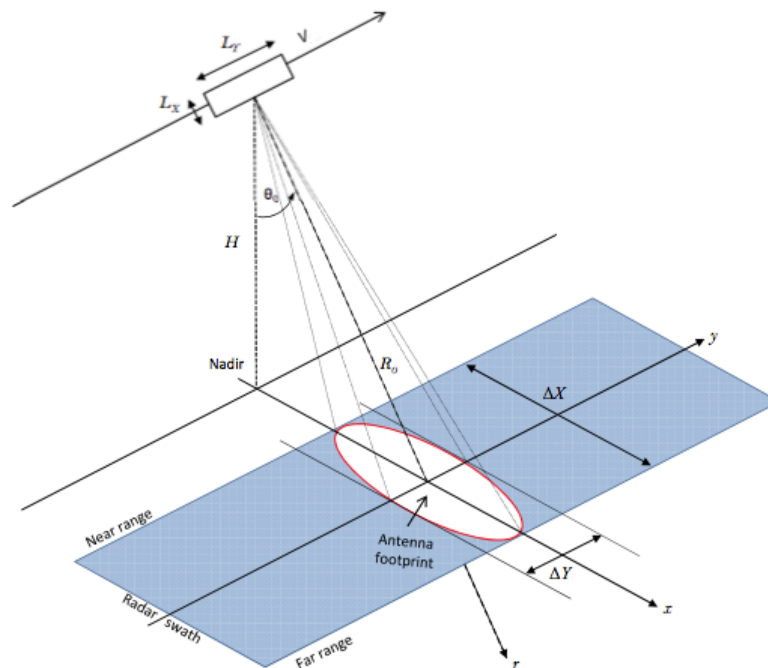


Fig. 1.3: Basic geometry of an airborne SAR

The direction of flight is called the azimuth direction ( $y$ ), while the range direction is identified by the direction perpendicular to the flight path;  $\theta_0$  is the incidence angle. The radial axis is denoted as slant-range ( $r$ ), while the area illuminates by the antenna beam in azimuth ( $y$ ) and ground-range ( $x$ ) direction, is named antenna footprint. From the antenna dimensions ( $L_x, L_y$ ), we can define the antenna footprint

by means of the aperture dimensions  $(\theta_x, \theta_y)$  as follows:

$$\theta_x \approx \lambda / L_x \quad (1.1)$$

$$\theta_y \approx \lambda / L_y \quad (1.2)$$

where  $\lambda$  is the wavelength of the transmission signal. We can relate the wavelength  $\lambda$  with the radar carrier frequency  $f_0$  and the speed of light, by:

$$\lambda f_0 = c \quad (1.3)$$

Considering  $R_0$  as the distance between the centre of the antenna footprint and radar, it can be possible define the range swath ( $\Delta X$ ) and the azimuth swath ( $\Delta Y$ ):

$$\Delta X \approx \frac{R_0 \theta_x}{\cos \theta_0} \quad (1.4)$$

$$\Delta Y \approx R_0 \theta_y \quad (1.5)$$

During the acquisition the distance  $R$  between the target and the platform varies symmetrically around a central value  $R_0$ ; the  $R_{min}$  and  $R_{max}$  values indicates, respectively, the distance at near range (nearest to the nadir point) and at far range.

The start-stop approximation can be used to demonstrate this assumption. In this approximation the signal is transmitted and received by the SAR sensor, which stands in the same azimuth position along its flight path. After backscattering by a target, the signal was received and the system moves in a new position and the process can be repeated. The sensor images the target in a time interval  $T$  (called *integration time*), so at generic time  $t_a$  the range between the platform and the scatterer is given by:

$$t_a \in \left[-\frac{T}{2}, \frac{T}{2}\right] \quad R(t_a) = \sqrt{R_{min}^2 + (Vt_a)^2} = R_{min} \cdot \left[1 + \left(\frac{Vt_a}{R_{min}}\right)^2\right]^{1/2} \quad (1.6)$$

If we assume  $\frac{Vt_a}{R_{min}} \ll 1$ , we can linearize by using Taylor approximation  $(1+x)^\alpha = 1 + \alpha x$ , and we obtain:

$$R(t_a) = R_{\min} \left[ 1 + \left( \frac{Vt_a}{R_{\min}} \right)^2 \right]^{1/2} \approx R_{\min} \left[ 1 + \frac{1}{2} \left( \frac{Vt_a}{R_{\min}} \right)^2 \right] = R_{\min} + \frac{V^2}{2R_{\min}} t_a^2 \quad (1.7)$$

This is a parabola equation, hence the slant range variation follow a parabolic law, with  $R_{\min}$  as minimum.

The spatial resolution is another critical parameter for SAR imaging, and is described as the capability to separate two near targets. To realize an elevated spatial resolution it is necessary to produce short pulses with a high energy. In the SAR systems this aim can be achieved transmitting a long pulse with an energy distributed along the whole long pulse; the techniques useful to achieve the resolution that should have with a short pulse, is called pulse compression (Skolnik M.I., 1981).

This technique foresees a linearly modulated pulse of duration  $T_p$ . The frequency of this pulse move over a band  $B$  centred on a carrier frequency  $f_0$ ; a signal like this is called chirp (see Fig. 1.4).

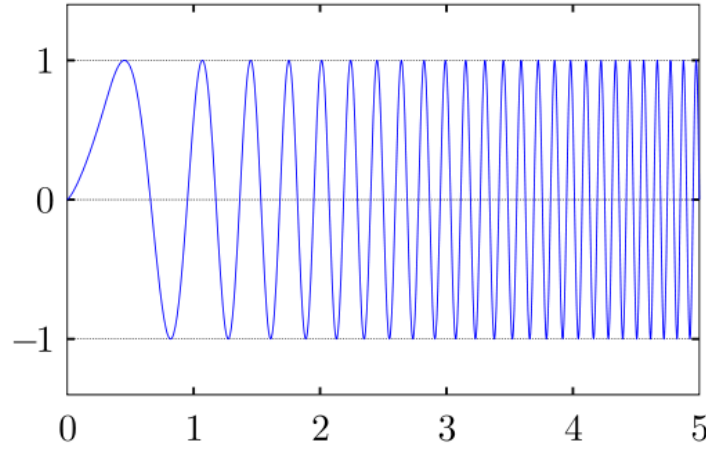


Fig. 1.4: Chirp waveform

Subsequently this pulse was compressed to an effective duration of  $1/B$  (Moreira A. et al., 1996). For the slant range the resolution it will be:

$$\delta_r \approx \frac{c}{2B} \quad (1.8)$$

Starting from the previous equation we can calculate the ground range resolution as the variation in ground range associated with a slant range of  $\delta_r$ . If  $\theta$  is the incidence angle, the ground range

resolution will be:

$$\delta x \approx \frac{\delta_r}{\sin \theta} \quad (1.9)$$

In case of real aperture radar we can separate two targets only if the distance between them is larger than the radar beamwidth (otherwise we receive the echoes at the same time). In this scenario, if we calculate the azimuth resolution in a precise time, for a range  $R_0$ , we will have (Reigber A., 2001):

$$\delta y = \Delta y = R_0 \theta_y = \frac{R_0 \lambda}{L_y} \quad (1.10)$$

From this relation is clear that high resolution in azimuth can be achieved with large antennas. To overcome the structural limitations represented by a very large antenna, the synthetic aperture concept has been developed (Brown W.M., 1967; Elachi C., 1987, Curlander J.C. and McDonough R.N., 1991) simulating a long antenna by the movement of a short antenna along the flight direction: this technique allows to synthesize a long (but virtual) antenna.

In this scenario the size of the antenna footprint ( $\Delta y$ ) will give the maximum length of the synthetic aperture; in this way the azimuth resolution will be:

$$\delta y = \frac{L_y}{2} \quad (1.11)$$

From the eq. (1.11) is clear that the azimuth resolution is not depends on the wavelength or range, but only on the physical size of antenna. For a SAR that is orbiting around the Earth, the corresponding azimuth resolution is given by (Oliver & Quegan, 2004):

$$\delta y = \frac{R_{\oplus}}{R_{\oplus} + H} \frac{L_y}{2} \quad (1.12)$$

where  $R_{\oplus}$  is the Earth's radius ( $R_{\oplus} = 6.371 \cdot 10^3 km$ ) and  $H$  is the satellite's orbit altitude. Today SAR systems can reach resolutions of several meters for low frequencies (as in the L-band), or resolutions of one meter and better for high frequencies (as in the X-band).

### 1.3 SAR Equations

If we assume an area on Earth surface (whose extension depends on sensor height, tilt and electrical size of antenna) illuminated by a sensor, which is moving with velocity  $V$ , we can describe the geometry of this system with cylindrical coordinates (Fig. 1.5)

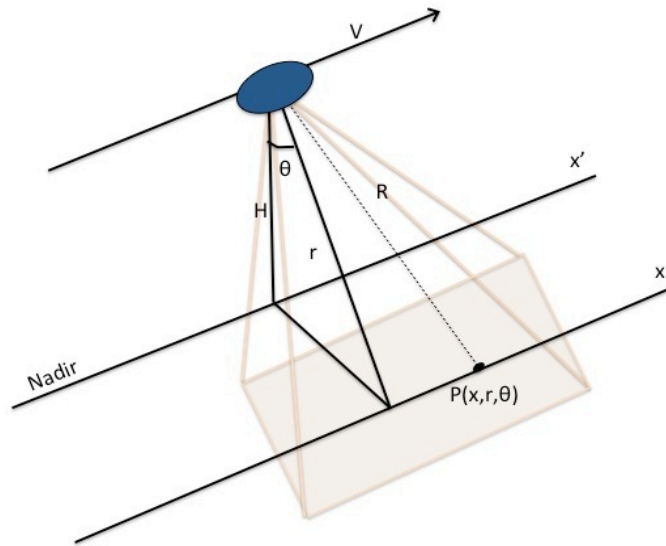


Fig. 1.5: Geometry of SAR acquisition.

In this system of reference,  $r$  (slant range) is the distance between the line-of-flight and the scattered point  $P(x, r, \theta)$ , the position of the point along the axis of flight is indicated with  $x$  (azimuth), and  $\theta$  is the elevation angle, the angle between the line of sight and the ground. The sensor transmits microwave pulses that periodically illuminate the target and return, after the round-trip time backscattered from the target.

In the previous section it has been shown the range resolution for a chirp pulse in the eq. (1.8) for an unmodulated pulse; we can rewrite this relation for a frequency-modulated pulse as:

$$\delta_r = \frac{c}{2B} = \frac{c}{2} \frac{2\pi}{\alpha\tau} \quad (1.13)$$

where  $B$  is the chirp bandwidth,  $\tau$  is the pulse width, and  $\alpha$  is the modulation factor (Iodice A. et alii, 2011-A).

The use of a chirp pulse involves a gain in range resolution given by:

$$\rho_{range} = \left( \frac{\pi c}{\alpha \tau} \right) \quad (1.14)$$

The signal transmitted back by the target (after being heterodyned), if the transmitted pulse is a chirp, will be:

$$f_{R_x}(x'-x, r'-r) = W^2 \left( \frac{x'-x}{X} \right) p \left( \frac{2r'}{c} - \frac{2R}{c} \right) \exp \left\{ -j \frac{4\pi}{\lambda} R \right\} \quad (1.15)$$

where  $R = \sqrt{(x'-x)^2 + r^2}$ . In this relation  $x'$  represents the sensor position,  $f$  is the carrier frequency,  $\omega = 2\pi f$  is the angular frequency,  $X$  is, for example, the synthetic antenna dimension, and  $W$  is a function that represents the antenna radiation pattern. After substituting:

$$t - t_n = 2 \frac{r'}{c} \quad (1.16)$$

the point-spread function of a SAR signal, or in other words the received signal expressed in function of space coordinates, will be:

$$f_{R_x}(x'-x, r'-r) = W^2 \left( \frac{x'-x}{X} \right) p \left( \frac{2r'}{c} - \frac{2R}{c} \right) \exp \left\{ -j \frac{4\pi}{\lambda} R \right\} \quad (1.17)$$

This equation is also known as SAR pulse response; from this is possible to write the SAR raw signal through a weighting function  $\gamma(x, r)$ :

$$h(x', r') = \iint dx dr \gamma(x, r) f_{R_x}(x'-x, r'-r) \quad (1.18)$$

The  $\gamma(x, r)$  function takes into account the acquisition geometry of each scene's scattering point, but also the electromagnetic properties of them (Franceschetti G. et alii, 1992).

A way to improve the results of the reflectivity function  $\gamma(x, r)$ , is to analyse the raw data in frequency domain.

Let us consider equations (1.17) and (1.18); we can write:

$$\tilde{\gamma}(x', r') = \gamma(x, r) \exp \left\{ -j \frac{4\pi}{\lambda} R \right\} \quad \Delta r = R - r \quad (1.19)$$

and:

$$g(x'-x, r'-r, r) = W^2 \left( \frac{x'-x}{X} \right) p \left[ \frac{2(r'-r-\Delta r)}{c} \right] \exp \left\{ -j \frac{4\pi}{\lambda} \Delta r \right\} \quad (1.20)$$

At this point the equation (1.18) turn in:

$$h(x', r') = \iint dx dr \tilde{\gamma}(x, r) g(x'-x, r'-r, r) \quad (1.21)$$

Now, considering the function  $G(\cdot)$ , the space-variant SAR Transfer Function, we can write the Fourier Transform for the raw signal:

$$H(\xi, \eta) = \iint dx dr G(\xi, \eta; r) \tilde{\gamma}(x, r) \exp \left\{ -j(\xi x + \eta r) \right\} \quad (1.22)$$

The  $G(\cdot)$  function can be written as:

$$\Psi(\xi, \eta, r) = \frac{\eta^2}{4b} - \frac{\frac{\xi^2}{4a} \frac{r}{r_0}}{\left( 1 + \frac{\eta\lambda}{4\pi} \right)} \quad (1.23)$$

To simplify calculations, assuming the results obtained by Franceschetti G. and Lanari R. (1999) for an asymptotic evaluation of equation (1.23): let us assume the antenna pattern is independent from the range coordinate, and let us assume the substitution  $b = \frac{2\alpha}{c^2}$ , and  $a = \frac{2\pi}{r_0\lambda}$  (where  $r_0$  is the centre scene slant range). Considering now the phase term:

$$\Psi(\xi, \eta, r) = \frac{\eta^2}{4b} - \frac{\frac{\xi^2}{4a} \frac{r}{r_0}}{\left( 1 + \frac{\eta\lambda}{4\pi} \right)} \quad (1.24)$$

The transfer function can be written as:

$$G(\xi, \eta, r) = \text{rect} \left( \frac{\eta}{bc\tau} \right) W^2 \left( \frac{\xi}{2aX} \right) \exp \left\{ -j\Psi(\xi, \eta, r) \right\} \quad (1.25)$$

The amount of energy released by a target in its environment (see Natale A., 2011 for the derivation from the Fourier transform of H in the case of r-invariant), once considering  $\tilde{\gamma}(x', r') = \delta(x' - \bar{x}, r' - \bar{r})$ , is written as:

$$i(x,r) = \text{sinc}[aX(x - \bar{x})] \text{sinc}\left[b \frac{c\tau}{2}(r - \bar{r})\right] \quad (1.26)$$

From this equation we can get an idea of the wide region, of the reconstructed signal, in which the target releases its energy:

$$D > 2\lambda \left(\frac{PRF}{c}\right) r_0 \tan \theta_0 \quad (1.27)$$

These relations represent the range resolution obtainable with a chirp waveform transmission, the first, and the azimuth resolution for the considered SAR system. Both are obtained starting from the SAR spatial resolution (i.e. the width of the sinc-function equal to 3dB). Furthermore in equation (1.27) the relation that link the dimension of antenna in azimuth direction and the footprint, is given by:

$$X \cong \frac{r_0 \lambda}{L} \quad (1.28)$$

Now, looking at equation (1.26), we can determine the spatial bandwidths, in range and in azimuth:

$$\left\{ \begin{array}{l} B_{range} = \frac{2}{c} B_{chirp} \\ B_{azimuth} = \frac{2}{L} \end{array} \right. \quad (1.29)$$

In addition to these relations there is a limitation on the PRF:

$$\frac{1}{T_r} > PRF > \frac{2|v|}{L} \quad (1.30)$$

The superior limit is related to  $T_r$ , that is the time in which the signal of entire scene is received. If we called  $S$  the swath,  $T_r$  is expressed by:

$$T_r \cong \tau + \frac{2S \sin \theta_0}{c} \cong S \frac{\sin \theta_0}{c} \quad (1.31)$$

The superior limit of PRF represents also a lower limit on the size of antenna in the across-track direction:  $D > 2\lambda \left(\frac{PRF}{c}\right) r_0 \tan \theta_0$ .

The inferior limit (i.e., the PRF must be larger than the azimuth temporal bandwidth) is imposed however, in order to avert a large computational load (Rees G., 2001), and is reflected as a lower limit on resolution of azimuth.

## 1.4 SAR Complex Images

When the SAR acquires an image it creates a 2-D array of pixels (columns and rows), in which at each pixel is associated a small area of the scene; the size of these pixels depends on the SAR system features. The surface reflectivity (also known as backscattering coefficient,  $\sigma^0$ ) of each scatterer located within the pixel is saved as complex number, containing information about amplitude and phase. The backscattering coefficient is dependent on several parameters, some of these related to the radar acquisition system characteristics (as incidence angle, polarization and frequency), other related to the observed surface properties (as roughness, dielectric properties, topography, local incidence angle, moisture content, etc.).

The knowledge of the backscattering coefficient, and hence of the SAR geometry acquisition, is pivotal to well interpret SAR data; in Fig. 1.6 the geometry of SAR acquisition is schematised.

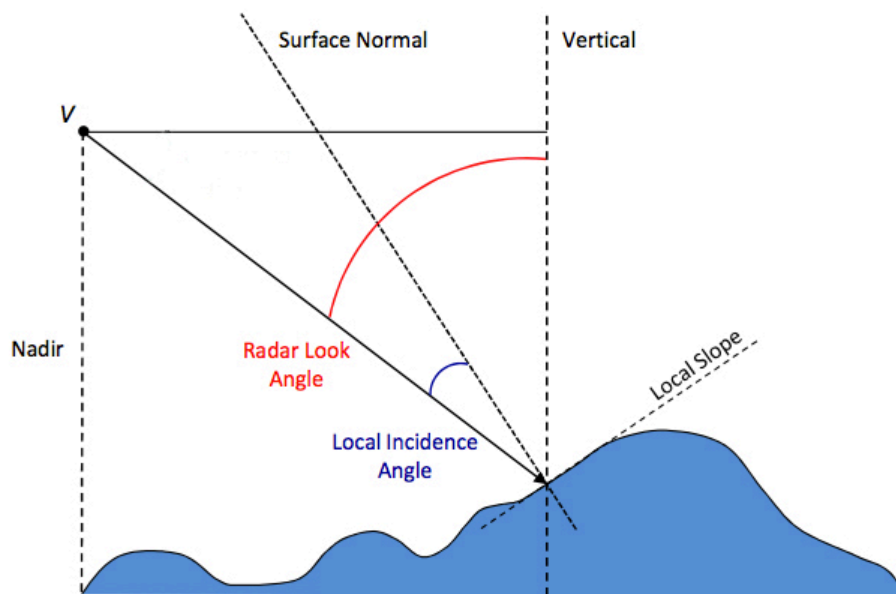


Fig. 1.6: Geometric effects of local slope variations.

Because of the spatial projection, the information about the structure of the scene is lost. Due to the acquisition geometry, each point at the same distance to the sensor (in range direction) is mapped into the same position, regardless of the different heights; as a consequence a geometric distortion exists in the SAR images.

The radar look angle (rla) is the angle between the range direction and the vertical antenna to the ground. In a flat planar scenario (each point is at the same height on surface), the variation of this

parameter over range causes a geometric distortion, but otherwise the relation between the scene and the corresponding image is given only by the  $r$ .

Also the topography can contribute to a geometric distortion; in fact, if topographic variations are present on the surface, the acquired images will show a geometrical distortion due to difference between slant range and the horizontal distance. The geometric distortions are classified in two main categories, foreshortening and layover, to which is also added radar shadow (Curlander J.C. and McDonough R.N., 1991).

In areas with great height variations, respect flat areas, the cross-track slant range distance for two points located on front mountains slopes are smaller. Consequently a cross-track compression of backscattered information occurs.

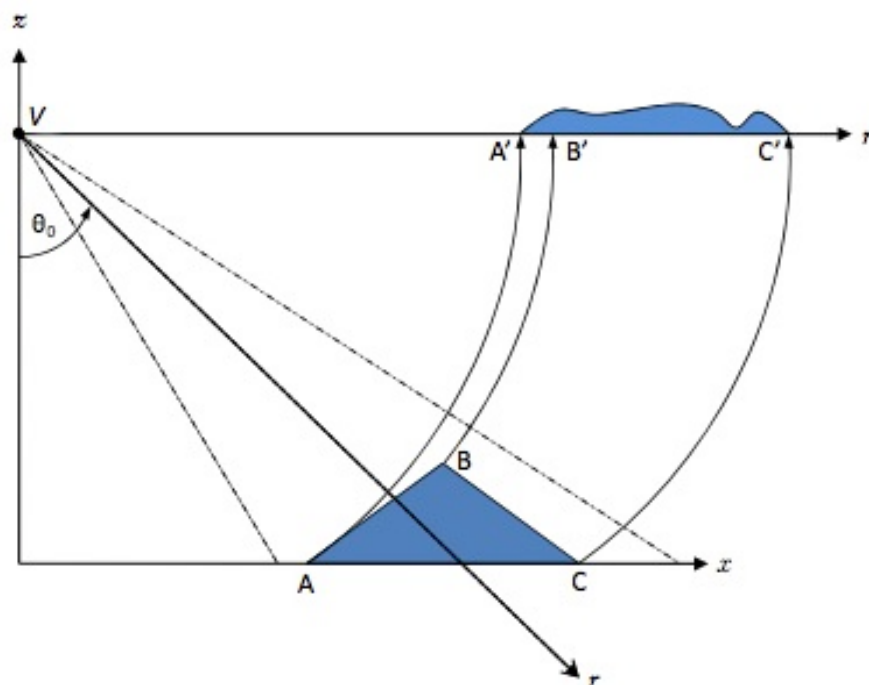


Fig. 1.7: Geometric distortion: foreshortening.

Looking at Fig. 1.7 it can note that the points A, B and C have the same distance from each other if projected on the ground, but these distances vary in the radar scene. This effect occurs because the SAR sensor presses the mountain image making it thin, because of the smaller distance with the top.

In the extreme scenario in which the slope is very steep, the points A and B are reversed in slant range image (see Fig. 1.8); this effect is known as layover.

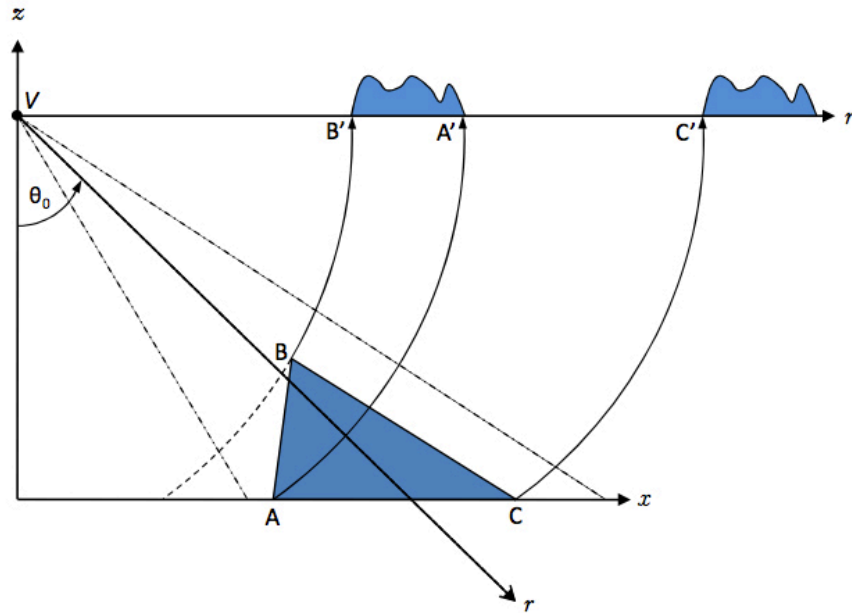


Fig. 1.8: Geometric distortion: layover.

The last geometric distortion is represented by a dark area in SAR images (zero signal), that are generated when the slope is steeper than the complementary of  $\theta_0$ ; this geometry produces a shadow areas and the effects is called radar shadow (see Fig. 1.9).

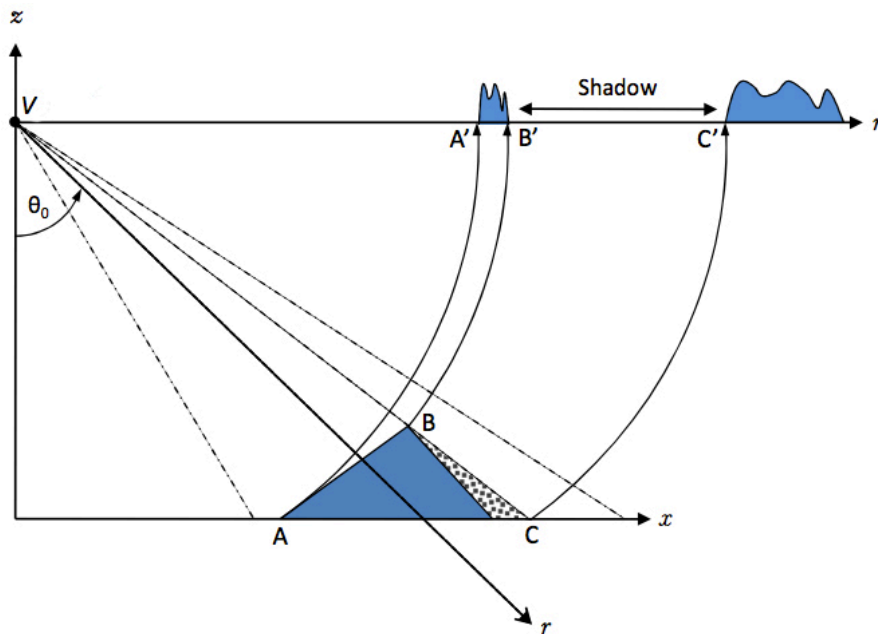


Fig. 1.9: Geometric distortion: radar shadow.

## 1.5 Complex Coherence

Another parameter that characterises the surface reflectivity is the complex coherence. Physically it is defined as the relationship between waves in a beam of electromagnetic radiation; practically is a measure of correlation between two images (phase term speaking).

Two wave trains of electromagnetic radiation are defined coherent when they are in phase, i.e. they vibrate simultaneously.

Some fundamental definitions on partially polarized waves are now recalled.

If we note with  $(\vec{e}_1, \vec{e}_2)$  the base polarization vector, we can write, for a scattered wave, the instantaneous electric field as:

$$\vec{E} = E_1 \vec{e}_1 + E_2 \vec{e}_2 \quad (1.32)$$

$E_i$  (with  $i=1, 2$ ) can be defined as a zero mean random process, in the case of a Gaussian area, as follows:

$$E_i = a_i \exp[j\delta(i)] \quad (1.33)$$

In this relation  $a_i$  is the amplitude and  $\delta(i)$  is a function uniformly distributed over  $(-\pi, \pi)$  (Goodman J.W., 1976). The covariance matrix,  $[J]$  also called coherency matrix, characterises a stationary electric field, and can be written as:

$$[J] = \begin{bmatrix} \langle E_1 E_1^* \rangle & \langle E_1 E_2^* \rangle \\ \langle E_1^* E_2 \rangle & \langle E_2 E_2^* \rangle \end{bmatrix} = \begin{bmatrix} j_{11} & j_{12} \\ j_{21} & j_{22} \end{bmatrix} \quad (1.34)$$

The  $j_{ii}$  elements of matrix  $[J]$  can be expressed as a function of the variance of  $E_i$  elements (i.e.  $j_{ii} = \langle a_i^2 \rangle$ ).

In the orthogonal base polarizations the SAR can measure these variances as a mean scattered intensities. The complex degree of coherence (or the normalized correlation coefficient) is given by:

$$\gamma = \frac{j_{12}}{\sqrt{j_{11}} \sqrt{j_{22}}} = \frac{\langle j_1 j_2^* \rangle}{\sqrt{\langle j_1 j_1^* \rangle \langle j_2 j_2^* \rangle}} = D e^{i\beta} \quad (1.35)$$

where  $\beta$  is the mean phase difference and  $D$  is the degree of coherence (Born M. and Wolf E., 1985).

A SAR system is defined coherent if it preserves the phase of the received signal.

The values of  $\gamma$  can range between 0.0 (no information contained in pixel) and 1.0 (no noise presents in pixel). For environmental applications a value around 0.5 or greater is expected.

Different parameters can afflict  $\gamma$  values:

- Properties of surface under study (vegetation, moving surfaces, etc.)
- Local slope (coherence decreases with steeply sloped surfaces)
- Time gap between passes in acquiring scene (greater the gap, lower the coherence)
- Technical issue of generation
- Baseline (large baselines provides low coherence)

Coherence can tell us more information about the surface type (vegetated versus rock versus urbanized) or can tell us when some change, visible only in the phase image, happened over the scene.

### ***1.6 Radar backscattering coefficient***

The SAR systems are at the same time an imaging and a measurement instrument. This means that it is necessary a calibration procedure to compare data which have different acquisition parameters (for example different SAR system sensors or acquisition mode). Thanks to a radiometric calibration it is possible to link the information held into a pixel with the physical observable. This procedure requires two steps: the first on the image itself, considering the relationship within the image, named relative calibration; the second related to the absolute observable held in image, in order to compare different imaging geometries, named absolute calibration (Freeman A., 1992).

Two main parameters are taking into account the intensity information for a SAR image: the radar brightness,  $\beta^0$ , that is the average radar cross section per pixel unit, (Wang H.P. et al., 2006); the backscattering coefficient,  $\sigma^0$ , that is the average radar cross-section per unit on the ground (in dB).

The brightness can be defined in terms of the digital number DN, and the absolute calibration constant,  $K$  (calculated by precision measurement):

$$\beta^0 = 10 \cdot \log_{10} \left( \frac{DN^2}{K} \right) \quad (1.36)$$

Considering the pixel projection on the ground and normalizing the brightness to the corresponding ground area, it is possible to define the backscattering coefficient as follows:

$$\sigma^0 = \beta^0 \cdot \sin \theta \quad (1.37)$$

As already seen,  $\theta$  is the incidence angle, which corresponds to the radar look angle in the case of flat terrain (but it changes rapidly if topographic variations are present). It can be determined from the imaging geometry as:

$$\theta = \arccos\left(\frac{H - \bar{z}}{R_0}\right) \quad (1.38)$$

In this relation  $H$  is the SAR system altitude,  $\bar{z}$  is the average terrain elevation and  $R_0$  is the slant range distance to the target.

The capacity of a SAR sensor to discriminate variations in  $\sigma^0$  is an index of quality measurements; this ability is called radiometric resolution.

### 1.7 Speckle

SAR images are shown as noise-like characteristics, for distributed targets, which appear as granulation, called speckle. This is a typical effect that afflicts system working at wavelength smaller than resolution and is due to the interference of the single scattering process happening within an image pixel.

We can think of distributed targets as a large number of scatterers arbitrarily distributed (see Fig. 1.10), whose total scattered field is given by the coherent superposition of the contributions of each of these discrete scatterers (Lee J.S., 1981; Lopes A. et al., 1990; Nezry E. et al., 1991; Lee J.S. et al., 1994).

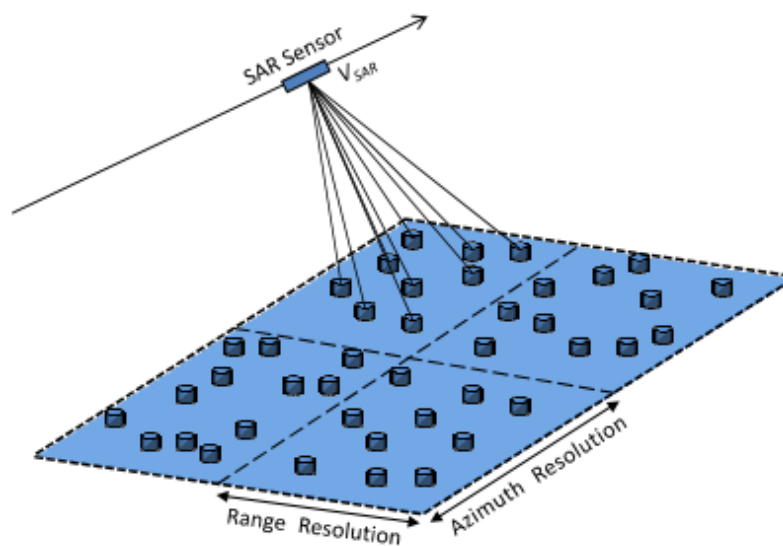


Fig. 1.10: Distributed targets scheme.

Within the resolution cell the individual backscattered signal of each scatterer is coherently summed giving a complex value that is measured by the sensor; the total returned modulation of the transmitted EM wave will be:

$$Ae^{i\phi} = \sum_{n=1}^N A_n e^{i\phi_n} \quad (1.39)$$

In this equation  $A$  represents the amplitude,  $\phi$  represents the phase while the number of discrete scatterers, within the resolution cell, is indicated with  $N$ . The total scattered fields will vary in amplitude and phase as a consequence of the spatial variations of  $N$  from pixel to pixel, as we can see in Fig. 1.11.

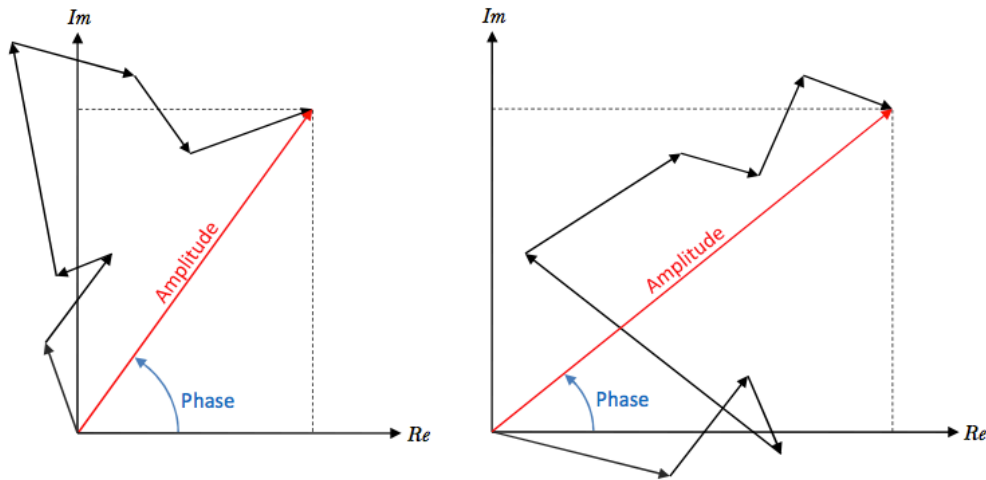


Fig. 1.11: Sum of discrete scatterers within the one resolution cell (pixel).

To well clarify, speckle is a consequence of the interference (constructive and destructive) between the complex backscattered signals from the target within each pixel and not strictly a noise. Therefore if we acquire a scene more times with the same configuration, we will have the same speckle pattern. This effect, that afflicts the radiometric resolution, can be minimized making a multi-look (average) while losing spatial resolution.

During the last decades different approaches have been developed (Frost V.S. et al., 1982; Nezry E. et al., 1991; Lee J.S. et al., 2009; Lee J.S. et al. 1999b; Lee J.S. et al. 2006; Touzi R. and Lopes A., 1994; Lee J.S. et al., 1991). To realize this average, or multi-look, some of them contemplate, in one way to split up in segments the synthetic aperture, process them as single image, and then make an average (frequency domain approach); or in other way to average adjacent pixels into the SAR image (spatial domain multi-look).

## ***1.8 Polarisation and surface scattering***

The scattering of an electromagnetic wave from a randomly rough surface is a problem deeply studied in the last decades, which has not received a solution because of lack of theory about. Nevertheless for most type of applications is sufficiently an approximate solution, and with this purpose, several empirical models have been developed.

For land applications the main problem involves the separation between the soil moisture and surface roughness effects within the scattered radiation. In this case polarimetry is pivotal because allows a direct separation of the two effects within the scattering problem.

To well estimate the surface parameters it is necessary to choose the right approximate solution for the scattering model; for radar remotely sensed data the widely used models involve the assessment of backscattering coefficients from single or dual channel data.

The measurements of surface roughness are essential to estimate with accuracy the soil moisture parameter from some scattering models; if the information about the roughness is not available, this parameter will be considered as a disturbing effect and can be minimised as occurs in numerous models (Hajnsek J., 2001).

Unfortunately it is not possible to estimate independently the roughness information by using single polarisation SAR system. A fully polarimetric data set provides a larger number of observables, and also the amount of surface parameter (and its estimation quantity) increases.

Some problems that are involved in the polarimetric data are related to the secondary or multiple scattering effects. In fact the multiple scattering becomes stronger when the roughness is higher, relatively to the wavelength, generating an adequate scattering component  $|HV|$ . Moreover the backscattered signal is also afflict by dihedral scattering (due to small correlation length, and with a contribution  $|HH| > |VV|$ ), or diffuse scattering ( $|HV|$  contribution). Also the contribution of vegetation can provide an effect of biased estimation of the roughness and moisture parameters.

### ***1.8.1 Polarimetric phase information***

In order to raise the number of observables, we can consider the polarimetric phase information of correlation coefficients (or polarimetric coherence, sensitive to surface parameters) between different polarisations. This coefficient of correlation is written in the form:

$$\gamma_{HHVV} := \frac{\left| \langle S_{HH} + S_{VV}^* \rangle \right|}{\sqrt{\langle S_{HH} S_{HH}^* \rangle \langle S_{VV} S_{VV}^* \rangle}} \quad (1.40)$$

This equation is evaluated respect to the sensitivity to dielectric constant or soil moisture condition within a definite roughness range (Borgeaud M., 1994).

For the surface roughness the correlation coefficient can be written as follows in a form that is independent from soil moisture and local incidence angle (Hajnsek J., 2001):

$$\gamma_{(HH+VV)(HH-VV)} := \frac{\left| \langle (S_{HH} + S_{VV})(S_{HH} - S_{VV})^* \rangle \right|}{\sqrt{\langle |S_{HH} + S_{VV}|^2 \rangle \langle |S_{HH} - S_{VV}|^2 \rangle}} \quad (1.41)$$

In the surface parameters estimation from polarimetric SAR data, the principal limit involves the presence of vegetation. Considering that a large amount of surfaces are covered by vegetation, this limitation allows us to understand the importance of radar remote sensing for a wide spectrum of geophysical and environmental applications.

### ***1.9 COSMO-SkyMed SAR System***

The COSMO-SkyMed (CONstellation of small Satellites for the Mediterranean basin Observation) project began in the '90s thanks to the collaboration between Italian Space Agency (ASI), Italian Ministry of Defence (ItMoD) and aerospace industries, with the aims to answer at a proposal for an Earth observation system focused on the Mediterranean region.

This project represents the first Earth observation satellite system in the world to be conceived and developed since the beginning for full dual applications (where a civilian requirement joins a military one). The major advantage of duality lies on the possibility to share technological, financial and human resources needed to develop and manage highly complex systems.

The COSMO-SkyMed programme is based on institutional requirements (coming from governmental organisation such as Civil Protection and Defence), linked to the management of environmental risks and prevention, as well as management of international crises. A wide range of scientific and commercial applications hold these requirements: as for civilian applications, the satellite allows to continuously monitoring phenomena such as landslides, floods, earthquakes, volcanic eruption, and fires as well as identification and monitoring of dumps and marine pollution events and terrain mapping. As for military applications, observations are related to both strategic intelligence

(information collection for crisis management, verification of international treaties on disarmament and operational planning), and tactical purposes in support of military operations.

Commercial and scientific applications include agriculture, forestry, mine and cadastral monitoring and census, and development of bi- and three- dimensional cartography, etc.

The COSMO-SkyMed system is a constellation of four SAR satellites, the first of these launched from Vandenberg, California, on 7 June 2007 by using a Delta II rocket, which was followed by the second platform in December 2007. The third and the fourth were launched in 2008 and 2010 (staggered at 90° on a given orbit, see Fig. 1.11). These satellites move into a helio-synchronous orbit inclined of 98.7° to the equatorial plane (so as to assure the maximum exposition of the solar cells to the radiation).

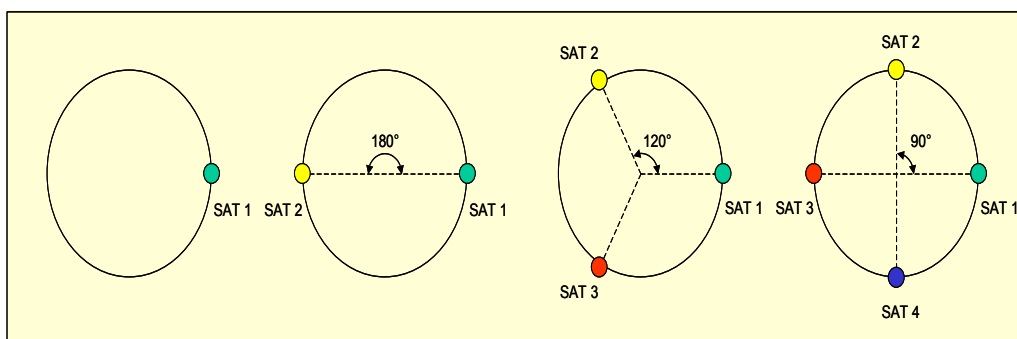


Fig. 1.11: Disposition for entry orbit.

This would allow to minimise the so called “revisit time”, i.e. the time between two consecutive satellite overflights on any area of interest, and ensure a global and unlimited access to each world region. Thanks to the number of satellites and their orbit parameters (see Tab. 1.1), this time ranges on the average from a maximum of 12 hours at equatorial latitude down to a minimum of 30 minutes to polar latitudes, with an intermediate value of 6 hours above the Mediterranean area.

<b>Number od satellites</b>	4
<b>Type of system</b>	Dual (for Civilian and Defence users)
<b>Orbit</b>	Polar helio-synchronous
<b>Inclination</b>	97.86°
<b>Orbits/day</b>	14.8125
<b>Nominal altitude</b>	619.6km
<b>Satellite phasing</b>	90°
<b>Shooting capabilities</b>	Up to 450 images per day per satellite
<b>Revisit time</b>	From 30 minutes to 12 hours, depending on latitude
<b>Nominal life-cycle of a single satellite</b>	5 years

<b>Ground segment</b>	Expandable up to 5 C-UGSs and 5 D-UGSs
<b>Satellite launch mass</b>	1860kg
<b>Solar panels</b>	Surface 16m <sup>2</sup> ; maximum power: 3.6kW at 42V
<b>Stabilisation</b>	Three axes
<b>On-board memory</b>	1200 Gbits
<b>Telemetry, Tracking and Command (TT&amp;C)</b>	S-band
<b>Downlink</b>	2 x 155Mbps
<b>Sensor</b>	X-band radar with active antenna
<b>Polarization</b>	Selectable among HH, VV, HV or VH
<b>Shooting modes</b>	ScanSAR Hugeregion (swathwidth 200km; resolution 100m)
	ScanSAR Wideregion (swathwidth 100km; resolution 30m)
	Stripmap Himage (swathwidth >40km; resolution 3÷5 m)
	Stripmap Ping-Pong (swathwidth >30km; resolution 15m)
	Spotlight 2 (10x10 km area; resolution 1m)
	Spotlight 1 (sub-metric resolution; only for Defence users)

Tab. 1.1: COSMO-SkyMed system main parameters.

The main operational modes (or image acquisition techniques, Fig. 1.12) of a SAR system are called Stripmap, Scansar and Spotlight. In the Stripmap mode, the radar antenna, positioned with its longer side along the satellite trajectory direction, observes an area on the Earth surface at right or at left of the orbit ground track (nadir), while the orbital motion of the platform allows the satellite to observe a strip of the same surface (see Fig. 1.13).

A SAR Stripmap image is limited in the transversal dimension (range), while the longitudinal dimension (azimuth) has no geometrical constraints, since it only depends on the acquisition duration.

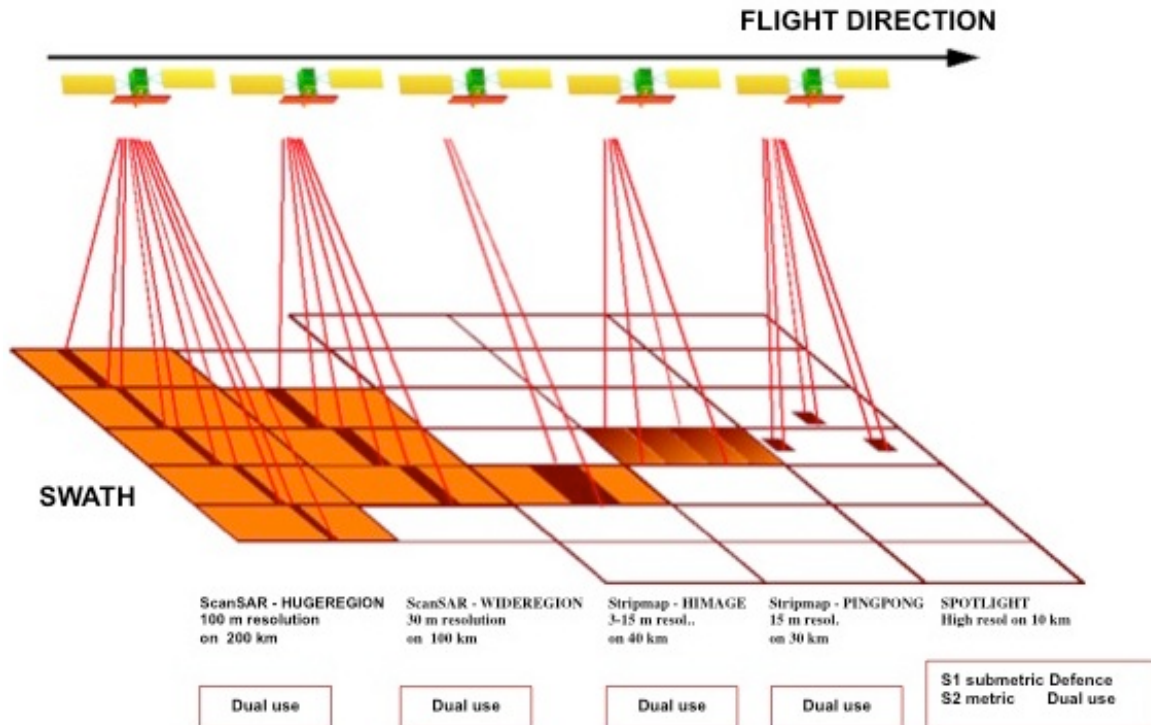


Fig. 1.12: COSMO-SkyMed image acquisition modes.

The Stripmap mode allows also multipolarimetric image acquisition. This technique includes switching between horizontal and vertical polarisation during image acquisition, which allows increasing information content (the same target may actually generate different returns, and consequently provide different information, depending on the signal polarisation).

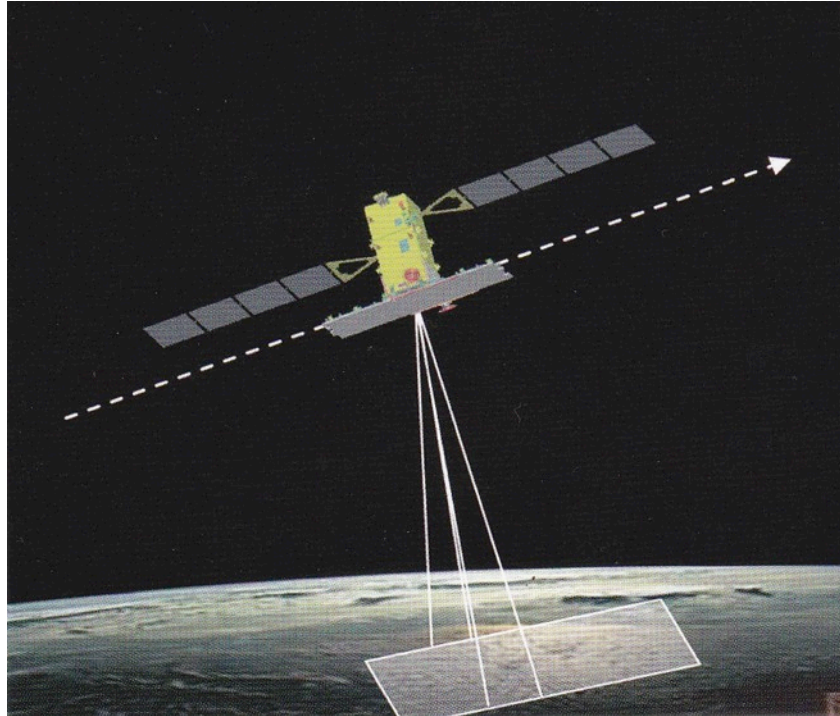


Fig. 1.13: Stripmap image acquisition technique.

The Scansar mode was developed to enlarge the observed zone. It consists in Stripmap techniques applied in sequence to several adjacent swaths (see Fig. 1.14), and requires a quick aiming capability of the antenna so as to locate its footprint in the various swaths accordingly to a defined sequence.

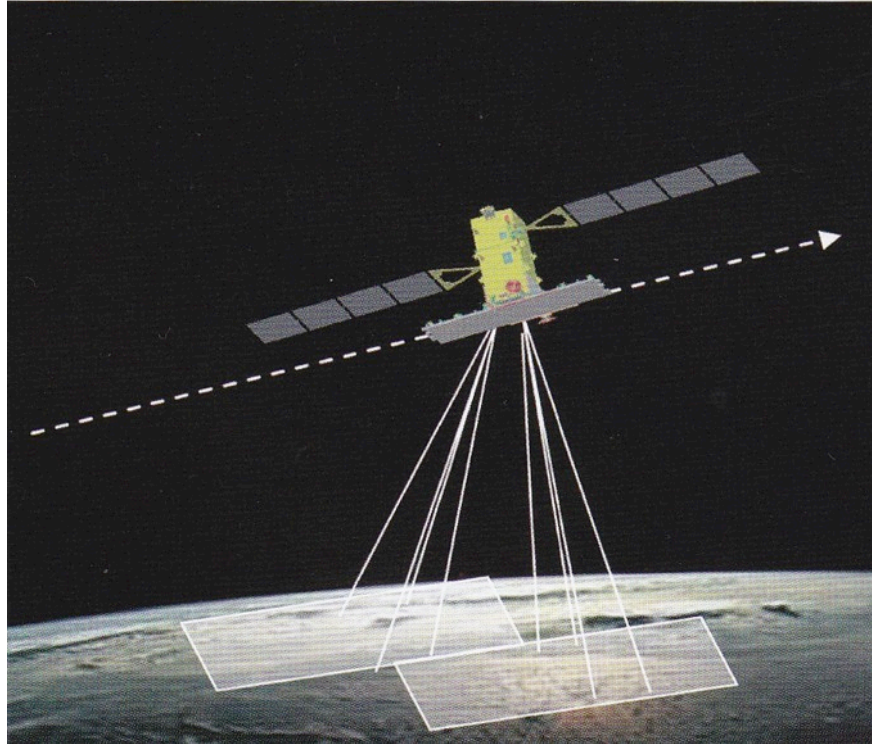


Fig. 1.14: Scansar image acquisition technique.

The image so obtained covers an enlarged area (for example 200 km x 200 km), but with a lower resolution (i.e. 100 m x 100 m). Such mode is especially used to observe large Earth surface (seas, deserts, open grounds) to assess the overall morphology.

The Spotlight mode is used to further improve images resolution by maintaining the antenna footprint on the area of interest. Since the platform motion would move the footprint position on Earth surface (as in the Stripmap mode), a continuous re-aiming of the antenna is required (Fig. 1.15).

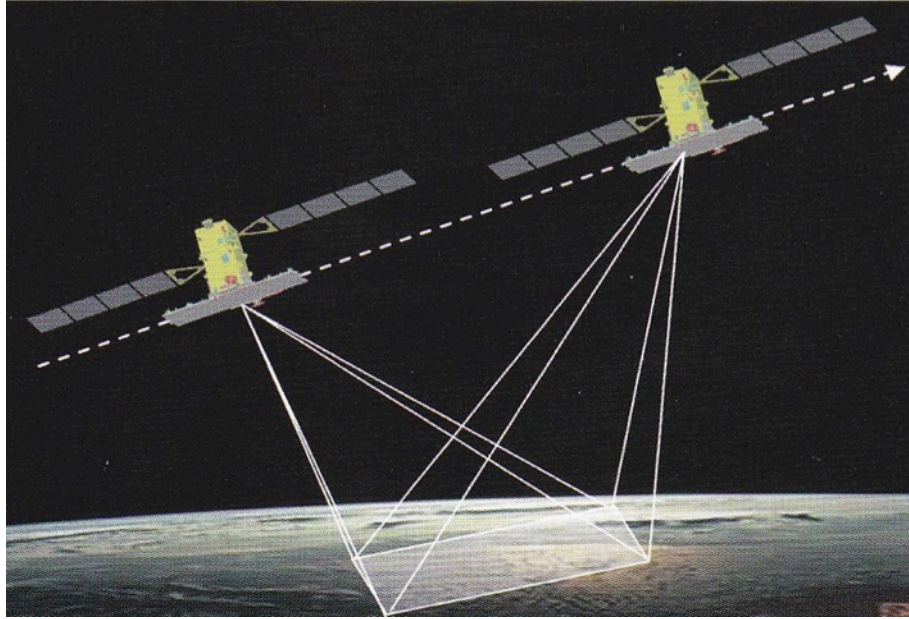


Fig. 1.15: Spotlight image acquisition mode

Thanks to peculiar data processing techniques, this mode allow obtaining a very high image resolution: 1m x 1m in the Spotlight 2 mode, and even higher (submetric resolution) in the Spotlight 1 mode, which is accessible only to the authorized Defence users of COSMO-SkyMed. In this case the observed area is smaller, for example, 10km x 10km.

Aiming the antenna beam and manoeuvring the satellites allows choosing, for all described modes, the observed area inside a larger zone, which is called access region.

## **CHAPTER 2**

### ***Properties of soil surfaces***

This chapter introduces the geometric and dielectric properties and the main parameters that characterize the soil surface. It describes how these parameters are measured and the importance of measuring them.

If we consider the surface of the Earth, the soil can be identified as a thin layer of porous media over the land surface, whose characteristics vary over space and time. It is easy to note that this description is however subjective, i.e. it depends on the purpose and the modality with which the study is conducted. For this reason, different people consider as relevant different parameters for determining the properties of the soil itself, such as materials, time, weather, vegetation, topography, morphology, etc.

The soil is composed for the most part of an organic component, derived from biologic decomposition process of flora and fauna, and of an inorganic component, derived from the alteration and erosion process of rocks (Jenny H., 1994).

Usually the first 2.5, 5, 10 or 15 cm of the soil column represents the interesting layer for geosciences topics (Bulfin M. & Gleeson T., 1967; Snell F.D. et al., 1950; Bond J.J. & Willis W.O., 1971; Mortland M.M., 1954; Shaver T.M. et al. 2002). Instead the interesting soil surface for radar applications is linked with the radar penetration depth, which is depending on the radar band, the soil texture and moisture, as well as density too (Ulaby F. T. et al, 1982).

#### **2.1 Surface Roughness**

In this section we will introduce some notions on the geometric properties of soil surfaces and on its main parameters.

The structure of the soil can be defined as the disposition of the solid particles and of the pore space between them (Low A.J., 1954), and is determined in the same way by the forces acting on its disposal and by the size distribution of its constituting particles.

Several physical and biological processes may contribute to the rearrangement of particles: action of earthworms, movement of water, swelling, burrowing animals, freezing, decomposition of plants roots.

The result of these processes is that shapes, sizes and disposition of the aggregates change, also under weather effects. These effects are manifested in a surface roughness, which can range from sub-millimetre (for example Aeolian deposition) to mountain dimension. In general we can classified the surface roughness in the deterministic surface and in randomly rough surface. The deterministic surfaces are identified by periodic irregularities in their profile, while the randomly rough surfaces, the most common in nature, have random irregularities. To describe this last class of surfaces it may be used a statistical distribution of irregularities that deviate from a defined reference level (Davidson M.W.J. et al., 2000). In literature, these irregularities of the surface profile are also called micro-relief and can be split up in categories depending on the creation, the size and the impact of soil:

1) Single particles and micro aggregates, unevenly distributed	Relief size < 2 mm
2) Large aggregates, unevenly distributed	Relief size (2-100) mm
3) Grooves and furrows, evenly distributed	Relief size (100-200) mm
4) Surface profile caused by geological processes.	Relief size >100m

All of these kinds of reliefs have a different impact on soil erosion process (Lal R., 1991).

Emerson W.W. (1959) proposed a hypothetical model showing that the microstructure of the tiny soil element is formed by quartz grains (linked by electrostatically) and by clay aggregates. Weather changes, rainfall, freezing, wind, and surface runoff, can modify the micro-relief.

All these characterizations are dependent on the soil type, the acquisition time of roughness measurement, the region and also on the crops types seeded. Moreover a different kind of tillage too, may affect the surface roughness in different ways.

For the description of the rough surface nature two characteristics are usually used: the difference of height respect to the reference surface and the height variation along the entire surface.

In the last two decades several studies, that have involved remotely sensed data acquired by microwave sensors, have been devoted to the surface roughness description (Davidson M.W.J. et al., 1998; Allain S. et al., 2003; Davidson M.W.J. et al., 2000; Bryant R. et al., 2007). These models, based on the correlation function, involve the surface correlation length,  $l$ , and the root mean square (rms) height,  $h$ , in order to parameterize the natural surface (Oh Y. et al., 1992; Fung A.K. et al., 1992; Cloude S.R., 1999; Satalino G. et al., 2001; Hajnsek I. et al., 2003).

It can be possible to describe the vertical surface roughness by mean of the rms height,  $h$ , i.e. the standard deviation of the surface height variation:

$$h = \sqrt{\frac{\sum_{i=1}^n (z_i - \bar{z})^2}{n-1}} \quad (2.1)$$

where  $z$  is the height variations in cm. By considering the horizontal structure of the surface roughness is possible to describe the surface correlation function  $p(x)$ , and hence the correlation length  $l$ . If we consider a discrete case with a spatial shift given by  $x' = (j-1)\Delta x$ , and if we indicate with  $z_{j+i-1}$  a point on the surface that is shifted by the point  $x^i$ , the normalized surface correlation function can be written as (Fung A.K. et al., 1996):

$$p(x') = \frac{\sum_{i=1}^{n+1-j} z_i z_{j+i-1}}{\sum_{i=1}^n z_i^2} \quad (2.2)$$

The value  $l = \infty$ , for which the normalized correlation function assumes values greater than  $1/e$ , is called surface correlation length,  $l$ . This parameter increases if increases the correlation between neighbour point:

$$p(l) = \frac{1}{e} \quad (2.3)$$

A perfectly smooth surface should have value  $l = \infty$ .

The  $h$  and  $l$  parameters, independent from each other, are useful to describe natural surfaces in a two-dimensional way. Ground measurements have demonstrated that the natural soils present very large variations that make difficult to develop a model, in particular for the correlation length.

Several studies have been developed for  $l$  variability classification, for example Baghdadi N. et al. (2007) developed a list of experimentally derived values of  $l$  for different kind of soils and for specific land uses. Two questions emerged from these studies, are the subjects of different discussions; the first is: for an accurate measurement of the surface correlation length, what should be the extension of the distance measurement? And the second is: to estimate an electromagnetic model, what should be the shape of the correlation function?

The first question was answered by Oh Y., Kay Y.C. (1998) and Oh Y., Hong J.Y. (2007); in their work have shown a decrease of  $l$  parameter with the length of profile. Moreover they calculate a limit on the profile length measurement of  $200l$  for a mean value of  $l$  estimated with a  $\pm 10\%$  precision. As a consequence there is a distortion on the correlation length values at short profile length that underestimate the value of  $l$ , and this error increases with the profile length decrease (Alvarez-Mozos J. et al., 2008).

Another study shows that, because the link between different tillage states and the sizes of clumps, for a 1m profile there is a correlation between  $h$  and  $l$ . As a result, a model to reduce the number of unknown about roughness surface problem can be developed (Davidson M.W.J. et al., 2000).

Usually, because the estimation problem in retrieving the surface correlation length, only the rms height is used to describe randomly rough surface, hence in most electromagnetic (EM) models the  $l$  parameter is neglected (Chen K. and Fung A.K., 1995). The relation between the scattered EM wave and the surface correlation length is expressed through the product with the wavelength number  $k$  ( $k = 2\pi / \lambda$ ) as  $kh$ , which decreases with increasing  $\lambda$ .

Several studies have been dedicated to the surface roughness retrieval in the last century; for a comprehensive summary we may look at Jester W. and Klik A. (2005).

## ***2.2 Soil Moisture and dielectric constant***

In the following sections main concepts about the relation between soil moisture and EM scattering measurement are explained.

### ***2.2.1 Soil Moisture***

We can think of the soil as a matrix that encloses the time and spatial variations of the main three phases that compose the soil itself: air, water, and particles.

Looking at soil particles, we can make a distinction considering the sizes of each grain, from the clay (particle diameter lower than 0.002mm), across the silt (particle diameter between 0.05mm and 0.002mm), until to the sand (particle diameter between 2mm and 0.05mm).

The part of the soil water in the soil matrix is related to the porosity of a portion  $V_g/V_t$  (volume of gas/bulk density of a quantity of soil) occupied by soil air and another  $V_l/V_t$  (volume liquid/total volume of a quantity of soil) occupied by soil water. We can express the quantity of water in a soil in:

$$\text{Water content, volume fraction} \quad R = V_l / V_t \quad (2.4)$$

$$\text{Water content, mass basis} \quad R = m_v / m_s \quad (2.5)$$

$$\text{Degree of saturation} \quad S = V_l / (V_l + V_g) \quad (2.6)$$

In these relations  $m_v$  is the volumetric soil moisture and  $m_s$  is the dry mass of the soil. If we call  $\rho_b$  the soil bulk density, and  $\rho_w = m_v / V_l$  the density of pure water (that remain unaltered when is absorbed by soils), we can calculate the volume fraction,  $R_v$ , combining the eq. (2.4) and the eq. (2.6), i.e. as a ratio of the depth of water to the depth of the soil column:

$$R_v = R_m \frac{\rho_b}{\rho_w} \quad (2.7)$$

This equation is often used to estimate the gain and the loss of water in the field (Gardner W.H., 1986). The soil moisture values can vary from zero to a maximum value representing the pore space saturation. Two intermediate stages are used in some hydrological applications; the field capacity (that represents the water content retrieved when a very wet soil has drained for 2 days), and the permanent wilting point (that represents dryer stage, i.e. the moisture content of a soil when the plants wither for lack of water).

In hydrological studies these stages are used as indicators for the soil moisture layer, as the limits at which the water is accessible to plants; a greater presence of clay in the soil can raise these limits.

It is to be considered too that a sandy soil will have a lower degree of saturation than a clay soil, because of the space between the sand grains (relatively large) that drain water quickly. For this reason, the distribution of the grains within a soil influences in a decisive manner the aeration of the soil itself, fluid retention, and the movement of water in its interior. Then the distribution of the grains is often more important than their own size (Scheffer F. and Schachschabel P., 2002).

The water can be held in the soil (soil water retention) through two mechanisms: the surface absorption and the capillary forces. Water can be sucked into the pores by capillary forces; however can be absorbed into the surface area of particles by swelling. Different materials can absorb water differently,

for example quartz grains don't have a large water absorption capacity, instead the clay particles are particularly able in this process.

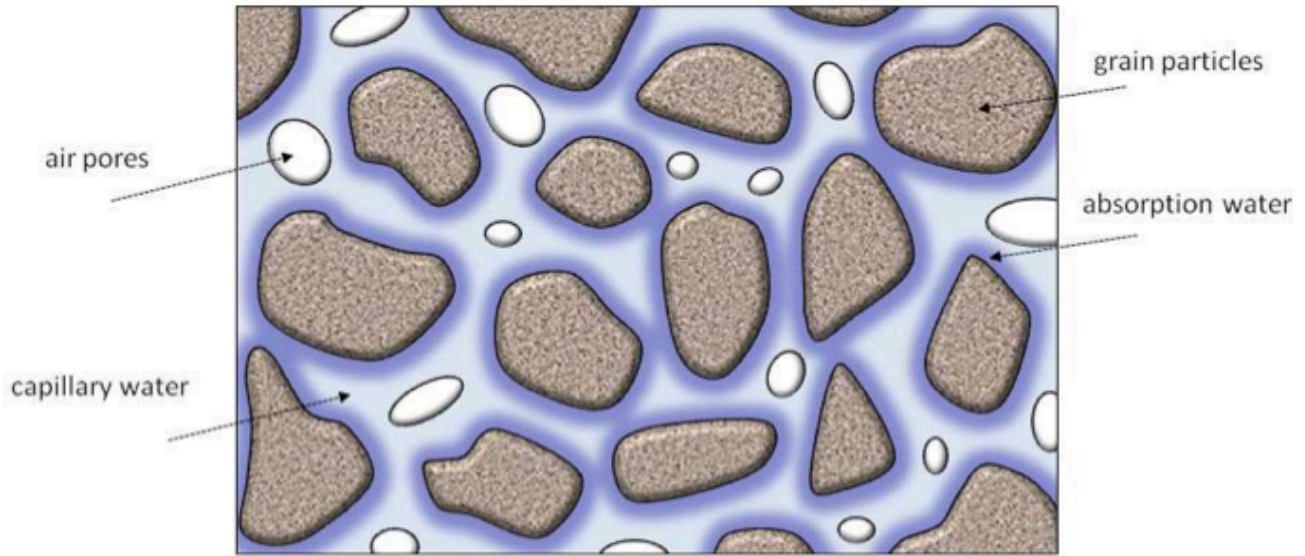


Fig. 2. 1: Main forces acting in the vadose zone to keep water in soil.

It is possible to show the different absorption capacity of different soil by looking at the water retention curve (Fig. 2. 2): we can note that the sandy texture, at lower suction, releases more water than the clayey texture. Usually the points on the curve at 1 and 150m of suction are used as reference, and correspond to the water content at permanent wilting point and at field capacity. At given suction different properties of soil regulate the quantity of water absorbed: texture, organic content, nature of clay minerals, and structure (Stewart B.A. and Summer M.E., 1992). As a consequence, only when we know the soil properties, we can measure the moisture characteristics.

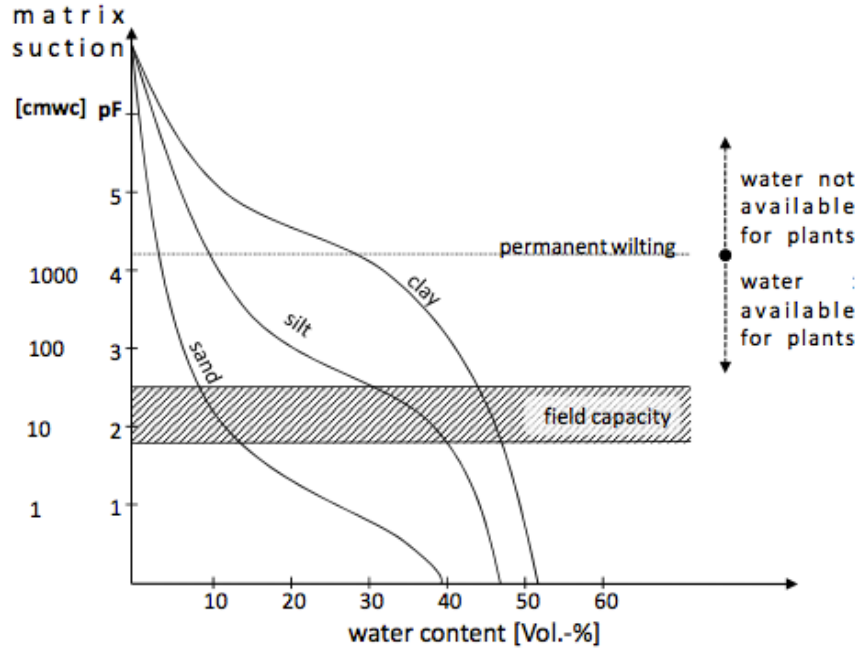


Fig. 2. 2: Water content and suction for a sand, silt and clay soil (Koyama C.N., 2012).

### 2.2.2 Dielectric constant

The dielectric constant is a complex parameter that describes the behaviour of a non-conductor in an electrical field. It depends on temperature, ferromagnetism, frequency, salinity, etc. This constant can be considered as the response of a medium to an electromagnetic field, and it is composed of an imaginary and a real part (Stratton J.A., 1941; von Hippel A., 1995), as follows:

$$\varepsilon = \varepsilon' - j\varepsilon'' \quad (2.8)$$

The first term at the right side,  $\varepsilon'$ , is the permittivity of a material; the second term,  $\varepsilon''$ , is the dielectric loss factor. This last term represents the capacity of a material to transform the energy of an absorbed wave into another form. We can say that most natural surfaces correspond to  $\varepsilon' \gg \varepsilon''$  (Stratton J.A., 1941).

It is possible to define a penetration depth of a wave into a medium, assuming an exponential attenuation for the electromagnetic energy (Ulaby F.T. et al., 1981-A).

$$\delta_p = \frac{\lambda \sqrt{\varepsilon'}}{2\pi \varepsilon''} \quad (2.9)$$

By definition  $\delta_p$  is about  $1/e$  (Euler's Number  $e \approx 2.7183$ ) of the input value (Ulaby F.T. et al., 1982), and increases with decreasing dielectric constant (for a fixed wavelength).

In general the dielectric constant value vary from 1 up to 80 (for a free liquid water) at low frequencies (Ulaby F.T., 1986), and for this reason the microwave spectrum is very sensitive to the moisture content.

In the last decades different empirical models that relate the dielectric constant to properties of soil have been developed. In all these models a polynomial expression that depends on the volumetric water soil content is used (von Hippel A., 1995; Hallikainen M.T. et al., 1985; Peplinski N.R. et al., 1995).

For a frequency between 1GHz and 10GHz, several studies (Topp G.C. et al., 1980; Hoekstra P., Delaney A., 1974; De Loor G.P., 1983; Wobschall D., 1977; Mattei E. et al., 2008; Ren W., Tateiba M., 1998) have demonstrated that a refractive relation, dependent only on the volumetric fraction of dry matter and free water, is a good approach for different kind of soil.

The dielectric constant variation for a mix of soil and water,  $R$ , may be calculated as first approximation considering three contributions. The first related to the water presence,  $R\varepsilon$ , the second related to the soil itself,  $[1-(R+\phi)]\varepsilon$ , and the last related to the air presence,  $\phi\varepsilon$ . Where  $R$ ,  $\phi$ , and  $[1-(R+\phi)]$  are respectively the volume fraction for the water, for the air-filled pores and for the soil.

Topp et al. (1980) developed a polynomial equation of the third order (like  $R = -a + b\varepsilon - c\varepsilon^2 + d\varepsilon^3$ ) to retrieve the volumetric moisture  $m_v$  through the real part of the complex dielectric constant  $\varepsilon'$  (the imaginary part of the complex dielectric constant can be neglected):

$$m_v = -5.3 \cdot 10^{-2} + 2.92 \cdot 10^{-2} \varepsilon' - 5.5 \cdot 10^{-4} \varepsilon'^2 + 4.3 \cdot 10^{-6} \varepsilon'^3 \quad (2.10)$$

that can be inverted in order to retrieve the real part of the complex dielectric constant:

$$\varepsilon' = 3.03 + 9.3m_v + 146m_v^2 - 76.7m_v^3 \quad (2.11)$$

Several studies have confirmed that this equation does not depend on soil properties, such as the texture, the bulk density, the temperature, the type or the salinity (Topp G.C., 1985; Dalton F.N. and Van Genuchten M.Th., 1986; Whalley W.R., 1993).

### ***2.3 Soil moisture retrieval techniques***

Several models for the direct or indirect measurement of water content have been developed: the models that include the process of evaporation, extraction or chemical removal to measure the soil

water, are called direct, instead the models that relate the water content of the soil with the chemical and physical properties of the soil matrix, are called indirect.

In this section we will look at the soil moisture retrieval models that use SAR data as input.

The promising approaches for water content estimation by using microwave radiation include: data fusion, microwave scattering models, change detection and semi-empirical approaches.

Semi-empirical models usually employ SAR imagery of single wavelength, incident angle and polarization.

Among these models the first that have used polarimetric radar data was that proposed by Oh Y. et al. (1992, 2000); this method uses the cross-polarized ( $\sigma_{hv}^0 / \sigma_{vv}^0$ ) and the co-polarized ( $\sigma_{hh}^0 / \sigma_{vv}^0$ ) ratios of the backscattering coefficients in terms of the surface parameters. The model was tested on radiometric data; as a consequence it may be not too accurate using SAR data.

Dubois P.C. et al. (1995) developed subsequently another empirical model that uses the backscatter co-polarized ratios only; although it was developed using radiometric data, its performances were also validated on the SAR data.

Two physical/theoretical models were presented by Fung A.K. et al. (1992) and Shi J. et al. (1997). The model proposed by Fung et al, the Integral Equation Method (IEM), uses radar scattering model to predict backscatter signal from different inputs (i.e. radar frequency, surface roughness, dielectric constant, incidence angle). The Shi model (Shi J. et al., 1997) is based mainly on the IEM and is modified and extended to accommodate parameter retrieval. This model was tested only on SAR data; the algorithm and its inverse require the knowledge of the surface roughness to estimate the water content, hence its implementation is complex and difficult.

In recent years another theoretical model was developed: the Polarimetric Two-Scale Model (PTSM, Iodice A. et al., 2010). This model describes the scattering from a bare soil surface, and shows an inversion method to estimate the surface roughness and the dielectric constant from the co-polarized and cross-polarized ratios.

All these models provide good results in areas with short vegetation or bare soil, but can provide erroneous results in areas where the vegetation is higher.

### ***2.3.1 The Dubois Model***

In the last years several models have been developed for soil moisture retrieval considering vegetated areas. Among these approaches, the empirical model of Dubois P.C. et al. (1995) tends to be a better

choice (it employs only co-polarized backscattering coefficients that are less sensitive to system noise and cross-talk), because it provides good results for both SAR and radiometer data (that are very sensitive to the water soil content). This model, where the co-polarised backscattering coefficients are expressed as a function of system parameters, such as frequency and incidence angle, as well as a function of soil properties as dielectric constant and surface roughness, is applicable to different data measured by different sensors and tends to be quite accurate in most cases. For surface height between 0.3cm and 3cm, wavelength  $\lambda$  between 1.5GHz and 11GHz, incidence angle  $\theta$  between  $30^\circ$  and  $65^\circ$ , the backscatter coefficients for this model, are expressed as follows:

$$\sigma_{hh}^{\circ} = 10^{-2.75} \frac{\cos^{1.5} \theta}{\sin^5 \theta} 10^{0.028\epsilon' \tan \theta} (kh \sin \theta)^{1.4} \lambda^{0.7} \quad (2.12)$$

$$\sigma_{vv}^{\circ} = 10^{-2.35} \frac{\cos^3 \theta}{\sin^3 \theta} 10^{0.046\epsilon' \tan \theta} (kh \sin^3 \theta)^{1.1} \lambda^{0.7} \quad (2.13)$$

where  $h$  is the rms surface height,  $k$  is the wavelength number, and  $\epsilon'$  is the real part of the complex dielectric constant. These equations represent a system of two non-linear equations with  $ks$  and  $\epsilon'$  unknown. The backscattering coefficients  $\sigma_{hh}^{\circ}$  and  $\sigma_{vv}^{\circ}$  decrease with increasing local incidence angle, and increase when the surface roughness values decrease. Moreover increasing local incidence angle, the sensitivity to moisture content decreases.

In order to determine the soil moisture parameter, we can compute the  $\epsilon'$  from the eq. (2.12) and (2.13) system, obtaining:

$$\epsilon' = \frac{\log 10 \left[ \left( \frac{(\sigma_{hh}^{\circ})^{0.7857}}{\sigma_{vv}^{\circ}} \right) \cdot 10^{-0.21} \cdot \cos^{1.82} \theta \sin^{0.93} \theta \cdot \lambda^{0.15} \right]}{-0.024 \tan \theta} \quad (2.14)$$

Once estimating the real part of complex dielectric constant, it is possible to substitute this value in eq. (2.10) in order to retrieve the soil moisture parameter,  $m_v$ .

We can summarise the performances of the empirical Dubois model as follows (Dubois P.C. et al., 1995):

- the validity ranges for the surface parameters have been estimated of about  $m_v \leq 35\%$  and  $kh \leq 2.5$ ; for the soil moisture retrieval applications the accuracy should be about  $4.2\text{vol.}\%$  and for surface roughness should be about  $kh$  of 0.4 for a bare surface;

- in order to achieve an accuracy better than 4vol.% for the inversion algorithm, the radar data should be calibrated within accuracy between the two co-polarised channel of 2dB absolute and 0.5 dB relative;
- to exclude vegetated areas contribution it is necessary to include also the cross-polarised data.

### 2.3.2 The Water-cloud Model

The Dubois model has been developed for bare soils with short vegetation; in order to circumvent this limitation and to include the canopy contribution, a method developed by Attema E. and Ulaby F. (1978) is used.

This model, based on the co-polarized backscattering coefficients, is called Water-Cloud Model, WCM, and presents a simplified approach to measure the backscattering coefficient including the soil and the vegetation contribution (Ulaby F.T. et al., 1986). For a given incidence angle this model gives:

$$\sigma_{pp}^0 = \sigma_{veg}^0 + \sigma_{veg+soil}^0 + \tau^2 \sigma_{soil}^0 \quad (2.15)$$

Here the total power scattered by the co-polarized backscattering coefficient in the  $pp$  channel,  $\sigma_{hh}^0$  for example, is represented by the incoherent sum of the underlying soil contribution  $\sigma_{soil}^0$  (attenuated by the vegetation layer) and the vegetation contribution  $\sigma_{veg}^0$ . In the eq. (2.15)  $\tau^2$  represent the two-way vegetation transmittivity, expressed as:

$$\tau^2 = e^{(-2bW_c \sec \Phi)} \quad (2.16)$$

where  $W_c$  is the vegetation water content ( $\text{kg/m}^2$ ),  $b$  is the attenuation parameter and  $\Phi$  is the nadir angle.

The expression for  $\sigma_{veg}^0$  is:

$$\sigma_{veg}^0 = Am_v \cos \theta (1 - \tau^2) \quad (2.17)$$

where  $m_v$  is the soil moisture content,  $\theta$  is the incidence angle, and  $A$  is the vegetation scattering. The  $A$  and  $b$  parameters depend on the type of vegetation. The type and geometrical structure of the canopy, as well as the polarization and wavelength of the sensor, are accounted for through these parameters, which are determined by fitting model against experimental data (Jackson T.J., Schmugge T.J., 1991; Bindlish R., Barros A.P., 2001).

The second term on the right side of the eq. (2.15),  $\sigma_{veg+soil}^0$ , characterizes the interaction between the vegetation and the underlying soil; this term is not dominant in the co-polarized backscattered signal and can be neglected (Dobson M.C., Ulaby F.T., 1986), hence it can be possible rewrite the eq. (2.15) in the following form:

$$\sigma_{pp}^0 = \sigma_{veg}^0 + \tau^2 \sigma_{soil}^0 \quad (2.18)$$

So this model takes into account and limits the influence of the vegetation canopy layer, isolating the co-polarized backscattering coefficient from the single contributions of absorption and scattering of vegetation.

## **CHAPTER 3**

### ***Study area and experimental results***

Several studies have demonstrated that soil moisture decreases the soil strength and increases the soil stress; hence this parameter has a critical part in many landslide events (Abramson L.W. et al., 1996).

Unfortunately often it is not easy to retrieve the soil moisture with in-situ measurements (Jacome A. et al., 2013). In these cases, the satellite measurement can help both the researchers and the rescue units. A SAR system can provide images independently on weather condition, and because it is an active sensor, can take images also in poor light conditions or in total darkness. These interesting features of microwave sensors have on the other side a penetration depth of some centimetres, from 1 to 5 cm, on bare areas.

#### ***3.1 Data set: Description***

This research has been funded by the Italian Space Agency (ASI) with the aim to identify a new possible application field for the second generation of Italian satellite COSMO-SkyMed.

With this purpose ASI has provided some Ping-Pong images (HH and VV polarization channel) from its archive acquired in the Campania region, during a period ranging from 2008 and 2011. This area encompasses a large portion of the territory comprising the entire Gulf of Naples (as reported in Google Earth images shown in Fig. 3. 1).

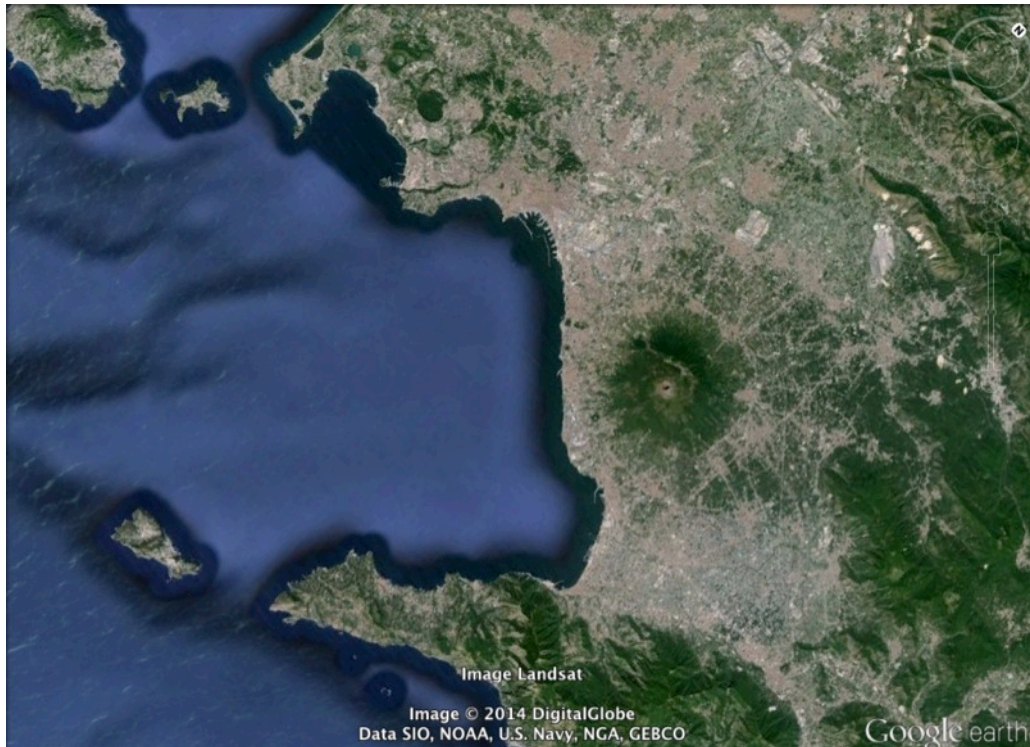


Fig. 3. 1: Google Earth image of Gulf of Naples.

The main acquisition parameters of these images are reported in the Tab. 3. 1, and the geographic coordinates for this site are:

- Top Left:                40°43'58'' N            13°51'30'' E
- Top Right:             41°7'20'' N             14°30'28'' E
- Bottom Left:         40°45'4'' N             14°21'55'' E
- Bottom Right:        40°46'2'' N             14°52'2'' E

#	Record Number	Date	Pol	Centre Scene Angle	Look Side	Pass direction
1	100682542	22/06/2011	CO	37.780°	Right	Ascending
2	100592540	16/09/2009	CO	30.950°	Right	Ascending
3	100591265	08/09/2009	CO	30.950°	Right	Ascending
4	100566362	11/05/2009	CO	30.950°	Right	Ascending
5	100541863	02/12/2008	CO	30.950°	Right	Ascending

Tab. 3. 1: Acquisition parameters of COSMO-SkyMed archive images.

The Gulf of Naples is spread over an area of about 870 km<sup>2</sup> and has an average depth of 170 m.

The coastline of the Gulf measures about 195 km and starts from Mount of Procida in the northeast to Punta Campanella at southeast.

The bay of Naples is dominated by Mount Vesuvius (an active volcano) at east, by the chain of Lattari Mountains in the south and Mount Epomeo (is a volcano-tectonic horst inserted into the centre of a complex system of active faults) on the Ischia Island. The northern part of the Gulf, to the west of Naples, is occupied by a system of volcanoes called Campi Flegrei.

The high presence of volcanic systems in the area involves a seismic activity, more or less evident depending on the different periods of activity

During the research study three more images were acquired by the COSMO-SkyMed constellation, and provided by ASI courtesy.

These Ping Pong images (HH and VV polarization channel) were acquired in December 2013 in Indonesian region of Pangkalanbuun, Central Kalimantan (Fig. 3. 2).

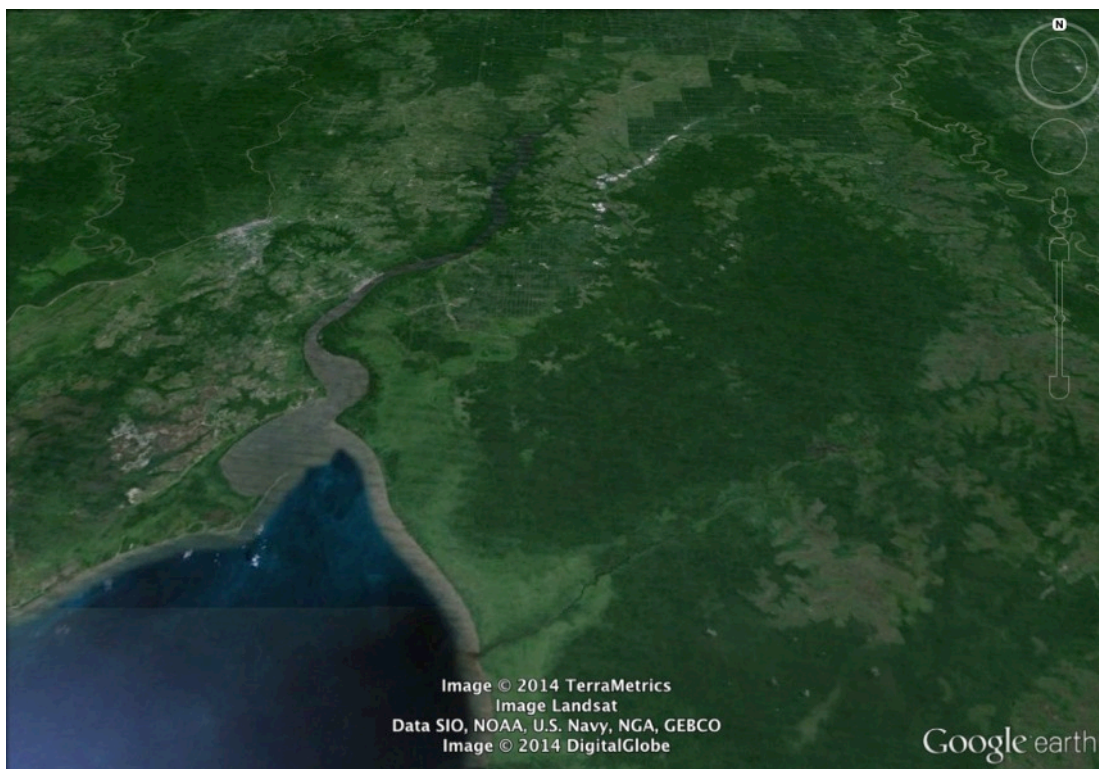


Fig. 3. 2: Google Earth images of Central Kalimantan region, Indonesia.

The main acquisition parameters of these images are reported in Tab. 3. 2, and the geographic coordinates for this site are:

# 1

- Top Left: 2°27'24.95'' S 112°3'32.80'' E
- Top Right: 2°23'44.52'' S 111°46'5.75'' E
- Bottom Left: 2°46'0.66'' S 111°59'43.48'' E
- Bottom Right: 2°42'19.84'' S 111°42'15.98'' E

# 2

- Top Left: 2°35'9.52'' S 112°1'57.36'' E
- Top Right: 2°31'28.93'' S 111°44'30.12'' E
- Bottom Left: 2°53'45.21'' S 111°58'7.89'' E
- Bottom Right: 2°50'4.23'' S 111°40'40.20'' E

# 3

- Top Left: 2°42'52.97'' S 112°0'22.08'' E
- Top Right: 2°39'12.21'' S 111°42'54.66'' E
- Bottom Left: 3°1'26.21'' S 111°56'32.97'' E
- Bottom Right: 2°57'45.06'' S 111°39'5.08'' E

#	Date	Pol	Centre Scene Angle	Look Side	Pass direction
1	01/12/2013	CO	29.497°	Right	Ascending
2	01/12/2013	CO	29.493°	Right	Ascending
3	01/12/2013	CO	29.490°	Right	Ascending

Tab. 3. 2: Acquisition parameters of COSMO-SkyMed images acquired in December 2013.

Located along the equator, Indonesia archipelago has a tropical climate with two distinct monsoon seasons, one wet and one dry. Average annual rainfall in the lowlands varies from 1780 to 3175 mm in the mountainous regions and can reach up to 6100 mm. The wettest areas are those mountainous of Sumatra, West Java, Kalimantan, Sulawesi and New Guinea. The humidity is generally high, averaging about 80%, and the temperatures vary little throughout the year (the average daily temperature in Jakarta is between 26°C and 30°C).

Indonesia is located on the edge of major tectonic faults, such as the Pacific Plate, Eurasian and Australian, which makes the region highly prone to phenomena such as volcanism and earthquakes

(and also tsunami as a consequence of strong earthquakes). In fact in this region is possible to count has at least 150 active volcanoes.

All of these phenomena can change significantly the morphology of an area.

For this Indonesian area, another image was taken into account for this study. The TerraSAR-X satellite, a German SAR system for Earth observation, acquired this image on March 13, 2008, and Astrium-GEO provided it freely for educational software for polarimetric data analysis.

This SAR satellite, under a polarimetric point of view, has the same characteristics that will have the COSMO-SkyMed Seconda Generazione (CSG) satellite. In this study a Dual-pol Stripmap image (HH and VV polarization channel) of Central Kalimantan region of Indonesia has been used as testing image for the future images of CSG system.

The geographic coordinates of the area acquired by TerraSAR-X system are:

- Top Left:                    2°28'45.09'' S                    111°57'4.69'' E
- Top Right:                    2°26'57.68'' S                    111°48'9.70'' E
- Bottom Left:                    2°59'2.47'' S                    111°51'9.26'' E
- Bottom Right:                    2°57'14.84'' S                    111°42'14.23'' E

and the main acquisition parameters are reported in Tab. 3. 3.

#	Date	Pol	Centre Scene Angle	Look Side	Pass direction
1	13/03/2008	CO	33.709°	Right	Ascending

Tab. 3. 3: Acquisition parameters of TerraSAR-X data of Central Kalimantan region, Indonesia.

In Fig. 3. 3 is reported a Google Earth image that show the three acquisition areas for COSMO-SkyMed satellite, and the one of TerraSAR-X system.

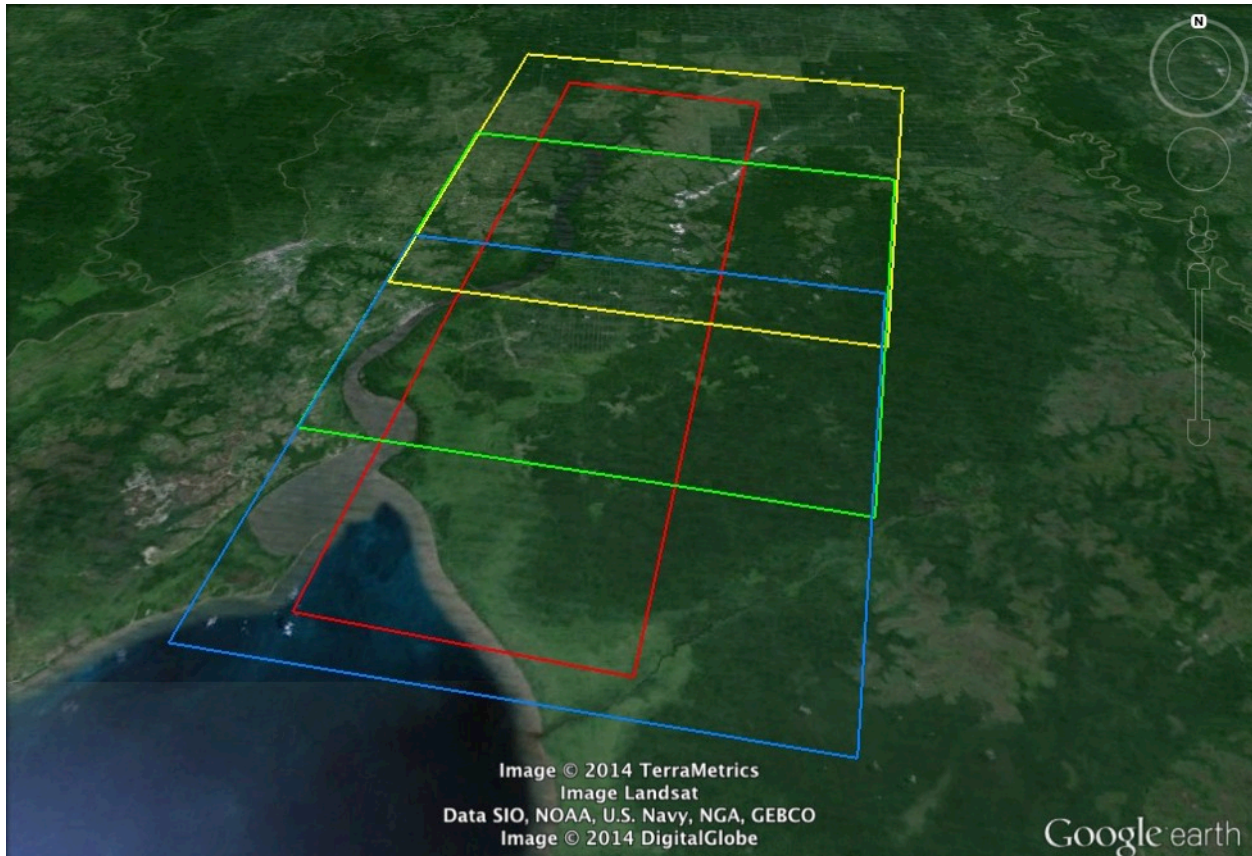


Fig. 3. 3 Google Earth image of Indonesian acquisition area. In red line the area acquired by TerraSAR-X satellite; in yellow, green and blue lines the areas acquired by COSMO-SkyMed satellite (respectively #1 yellow, #2 green, #3 blue).

### ***3.2 Data set: Processing and Analysis***

In this chapter the processing and analysis procedure will be described in more detail.

#### ***3.2.1 Data set processing***

The images provided by the ASI and Astrium-GEO, have passed a first stage of processing aimed to prepare them for subsequent analysis.

This processing has followed some well-defined steps: first of all it is necessary to convert the complex data in phase/module signal data. This conversion step allows, separating the two polarization channels (HH and VV channel in this case study), to operate with the amplitude signal data.

Subsequently the data were subjected to a multilook processing. This tool is used to reduce noises or little errors or some differences (constructive-destructive interference, for example) present in adjacent pixels. This step allows a resizing of image but it should well calibrate the multilook level in order to not affect too much the resolution.

The last step of processing concern the speckle problem; this degradation effect is due to non-ideal nature of real imaging system. It is shown within the image as a granulation effect caused by a multiplicative noise within adjacent pixels. It is possible to reduce this speckle effect by smoothing radar images by applying one of the most speckle reduction models (called speckle filters) developed in the last years (for an extensive comparison between different models, see Zhenghao S., 1994).

For this research field it has been chosen to use the adaptive model developed by Frost V.S. (1982).

This model, to well adapt the filter to backscatter signal of the image data, estimates the scene reflectivity by involving the observed image (in terms of local mean and standard deviation) with the impulse response of the SAR system.

The impulse response of the SAR system is calculated by minimizing the mean square error between the scene reflectivity model (assumed as an autoregressive process) and the observed image.

So the model produces minimum mean square errors estimates within homogeneous areas while preserving edge structures.

The filter equation can be synthesized as:

$$m(t) = e^{-KC_l^2(t_0)|t|} \quad (3.1)$$

where  $K$  is a constant that controls the damping rate of the impulse response function;  $t_0$  is the pixel to be filtered;  $C_l(t_0)$  is the variation coefficient. When the variation coefficient is small, the filter smooths out the speckles (i.e. the granulation effect visible within radar images), and when  $C_l(t_0)$  is large it provides to preserve the original observed image.

In the following picture are reported the data resulting by these processing phases on the archive images of Gulf of Naples.

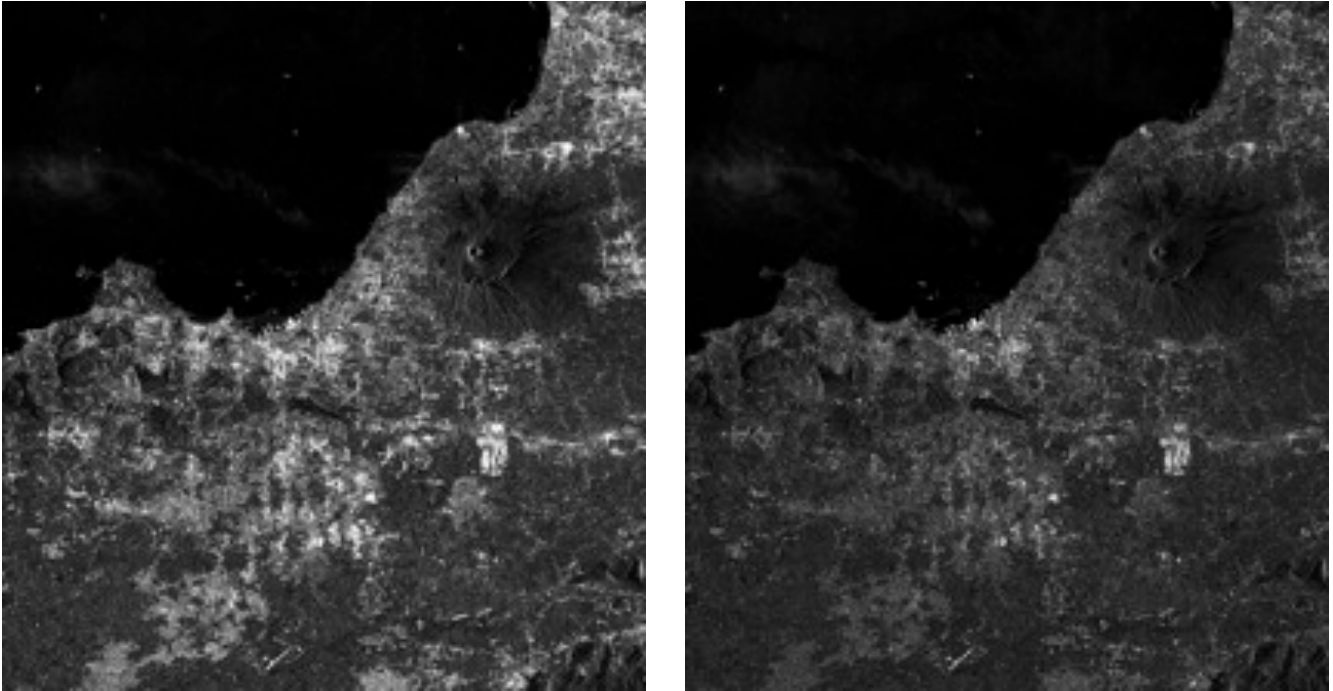


Fig. 3. 4: COSMO-SkyMed archive image acquired on December 2, 2008. At left is reported the HH polarization channel, while the VV polarization channel at right.

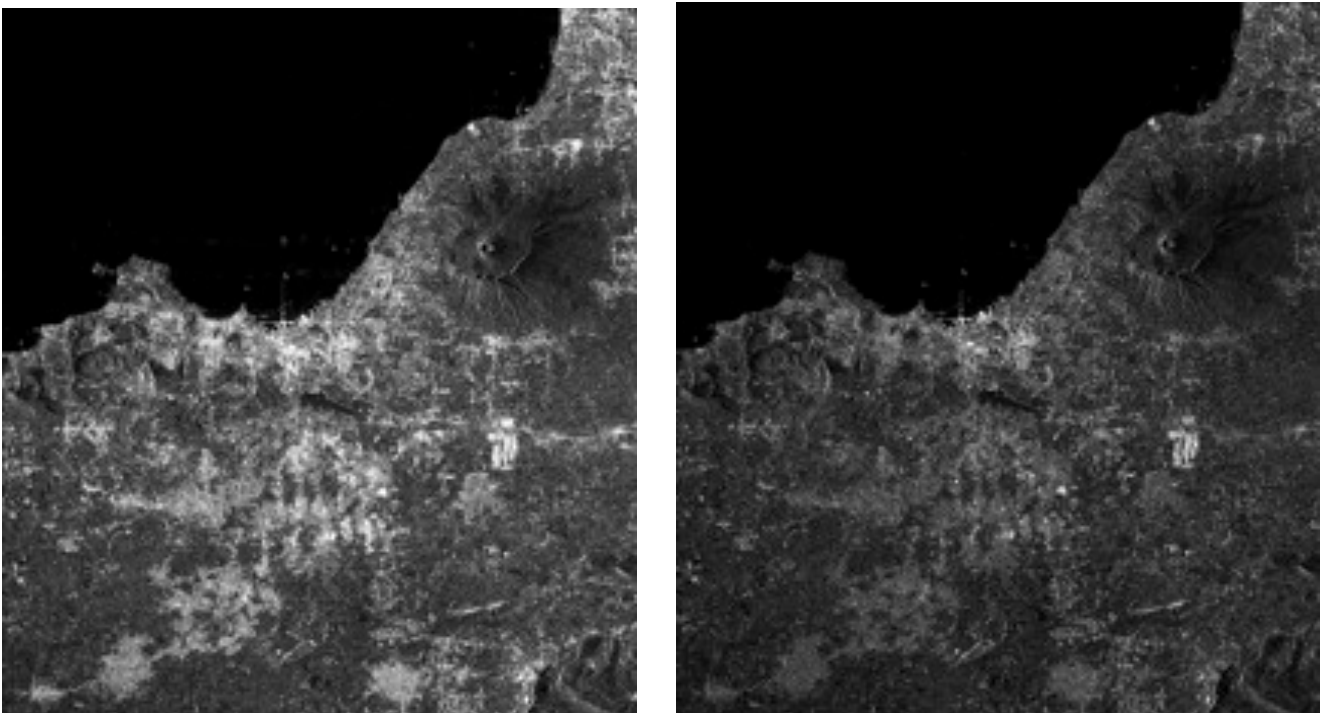


Fig. 3. 5: COSMO-SkyMed archive image acquired on May 11, 2009. At left is reported the HH polarization channel, while the VV polarization channel at right.

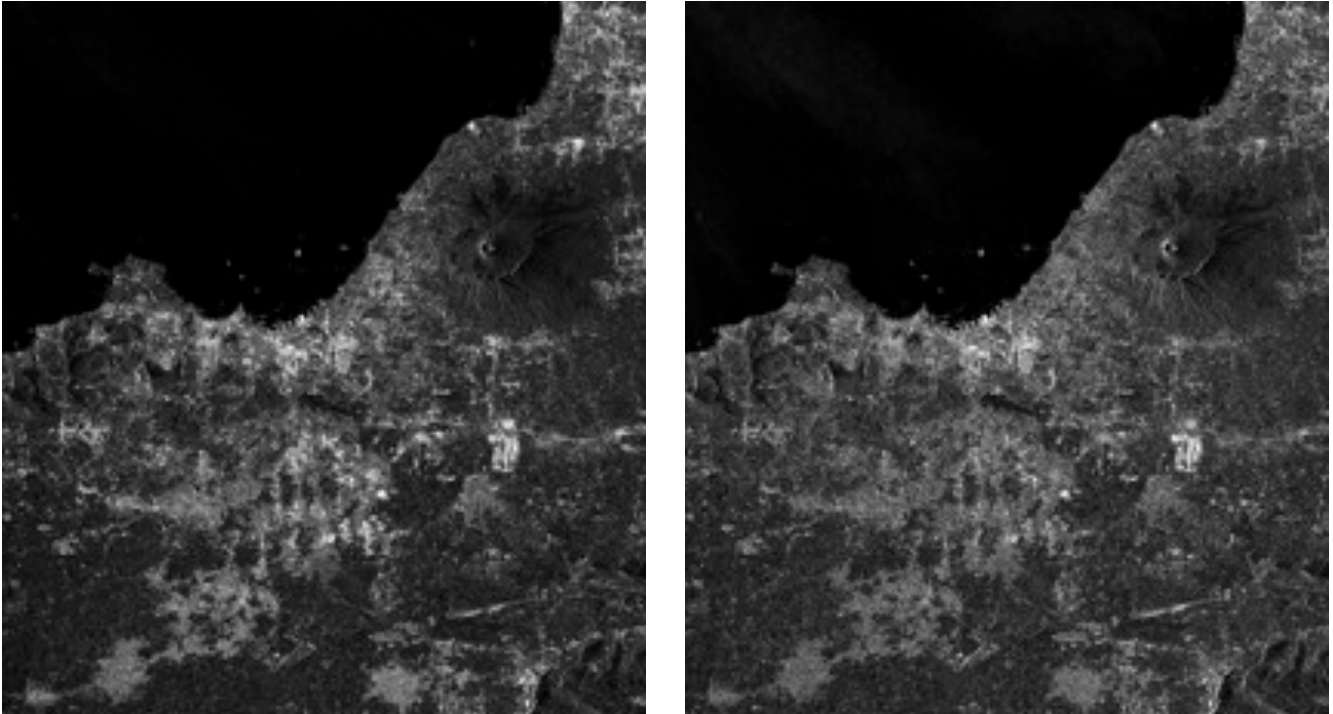


Fig. 3. 6: COSMO-SkyMed archive image acquired on September 8, 2009. At left is reported the HH polarization channel, while the VV polarization channel at right.

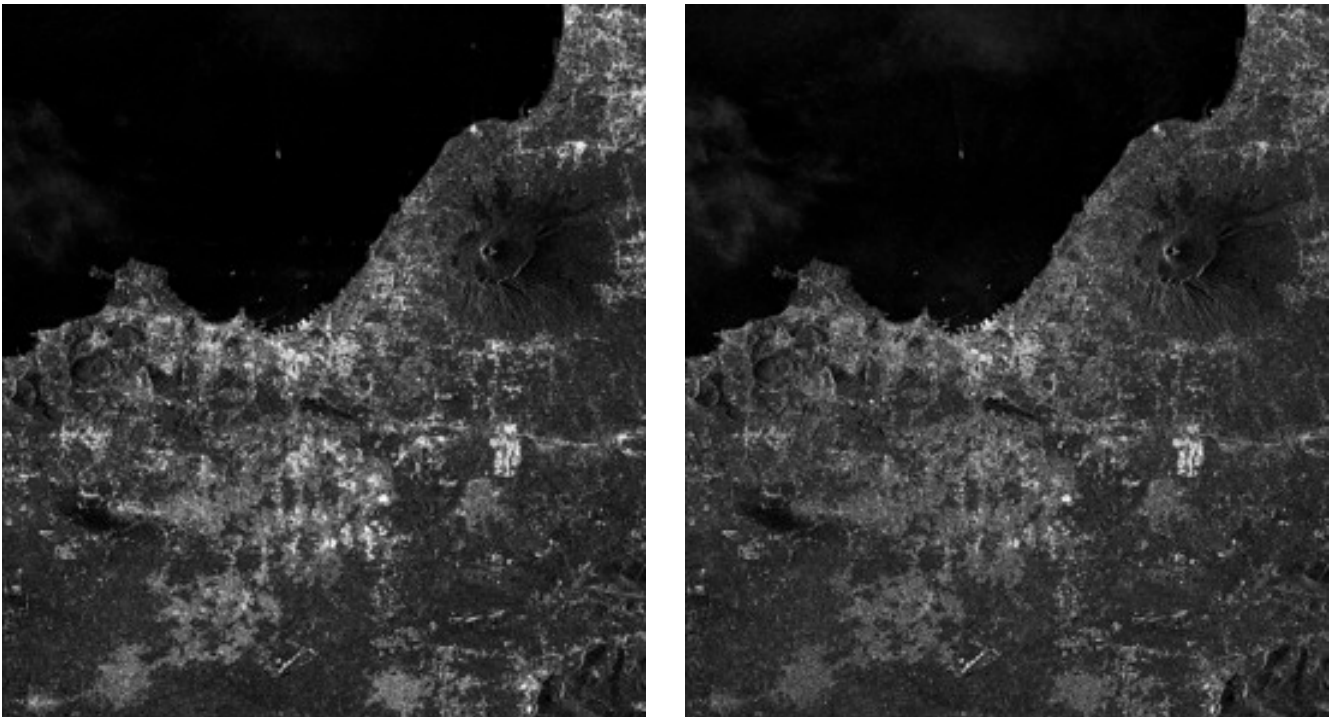


Fig. 3. 7: COSMO-SkyMed archive image acquired on September 16, 2009. At left is reported the HH polarization channel, while the VV polarization channel at right.

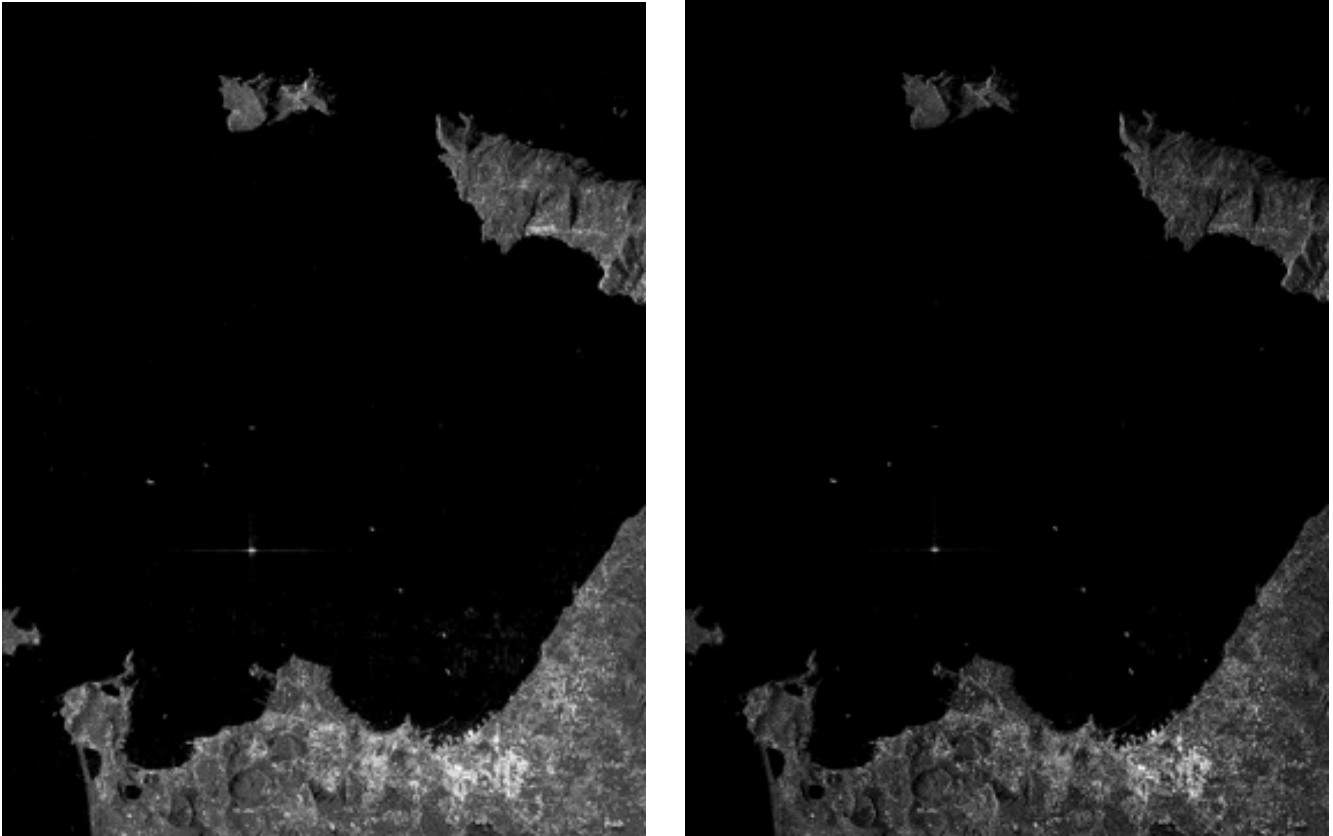


Fig. 3. 8: COSMO-SkyMed archive image acquired on June 22, 2011. At left is reported the HH polarization channel, while the VV polarization channel at right.

In these images we can see the capability of SAR sensor in the observation of a region for different purposes. For example for the maritime and coastal traffic monitoring, in fact in all of these images can be easily identified ships that stand out against the dark background of the sea.

Looking at the internal areas, stand-up urbanized sites (cities, airports, department stores, etc.) or those with a greater presence of man-made structures. Information like these are very useful for applications which involve land studies for civilian or military purposes. As the last, but not in order of importance, the SAR data are critical in environmental applications (for example dedicated to the study of the morphology surface, or targeted to monitoring and forecasting natural disasters, etc.), showing with extreme accuracy the variations of slopes and the different materials composing the land surface. Moreover the polarimetric data, containing more information than the single polarization data, can help to completely characterize (in terms of dielectric and soil properties) the observed area.

The figures from 3.9 to 3.11 show the COSMO-SkyMed images acquired in December 1, 2013, in the Indonesian State, after the processing phases above illustrated.

These images are related to areas with a low level of human settlement (thus with a low presence of man-made structures), but in which cultivated fields are visible. This result shows us (in addition to previous mentioned) the capability of SAR observation in the agricultural field too, thanks to the great signal response to the microwave radiation, backscattered from the cultivated areas. For this reason, the microwave systems are also subject to several studies with the aim to identify the different planted seed species.

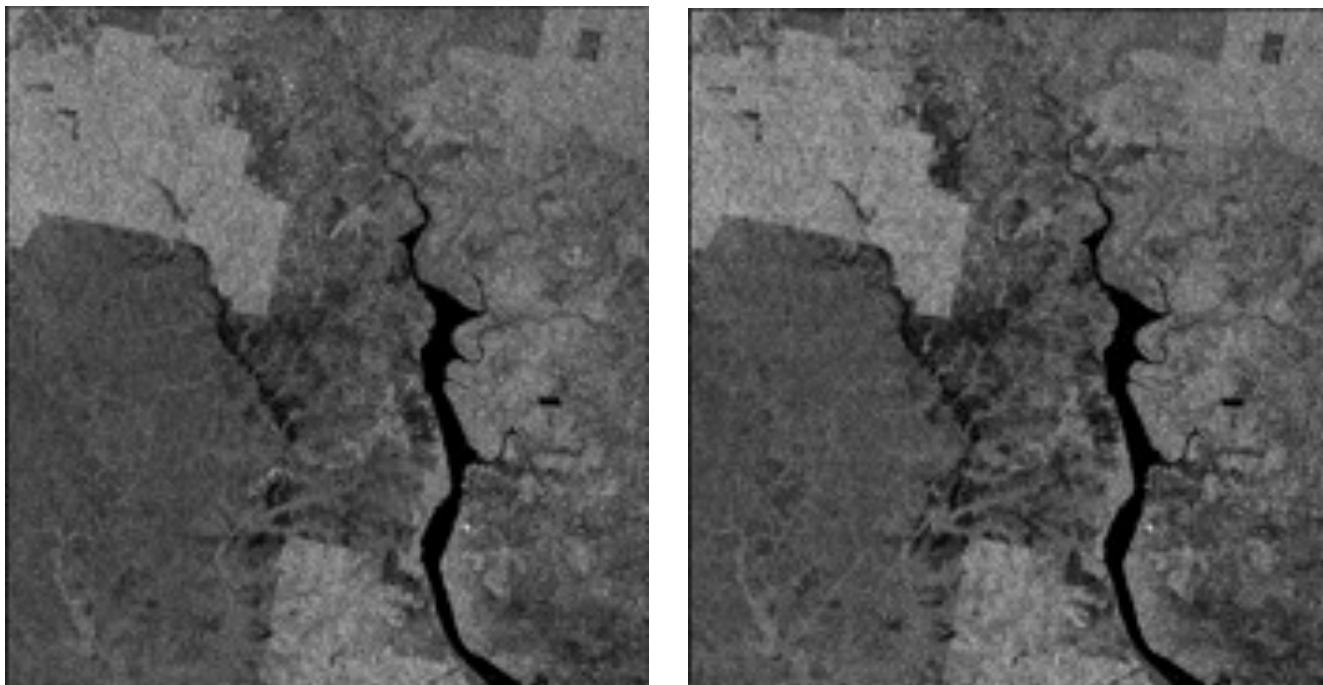


Fig. 3. 9: COSMO-SkyMed data acquired on December 1, 2013. At left is reported the HH polarization channel, while the VV polarization channel at right.

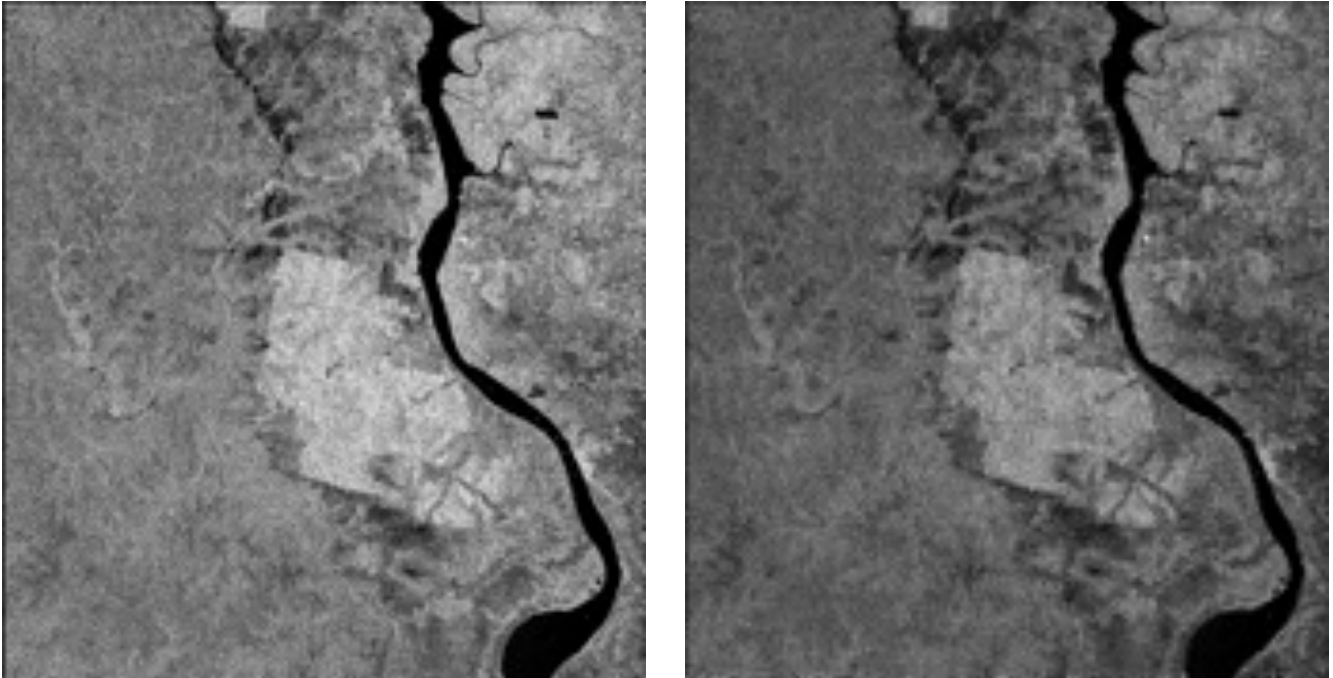


Fig. 3. 10: COSMO-SkyMed data acquired on December 1, 2013. At left is reported the HH polarization channel, while the VV polarization channel at right.

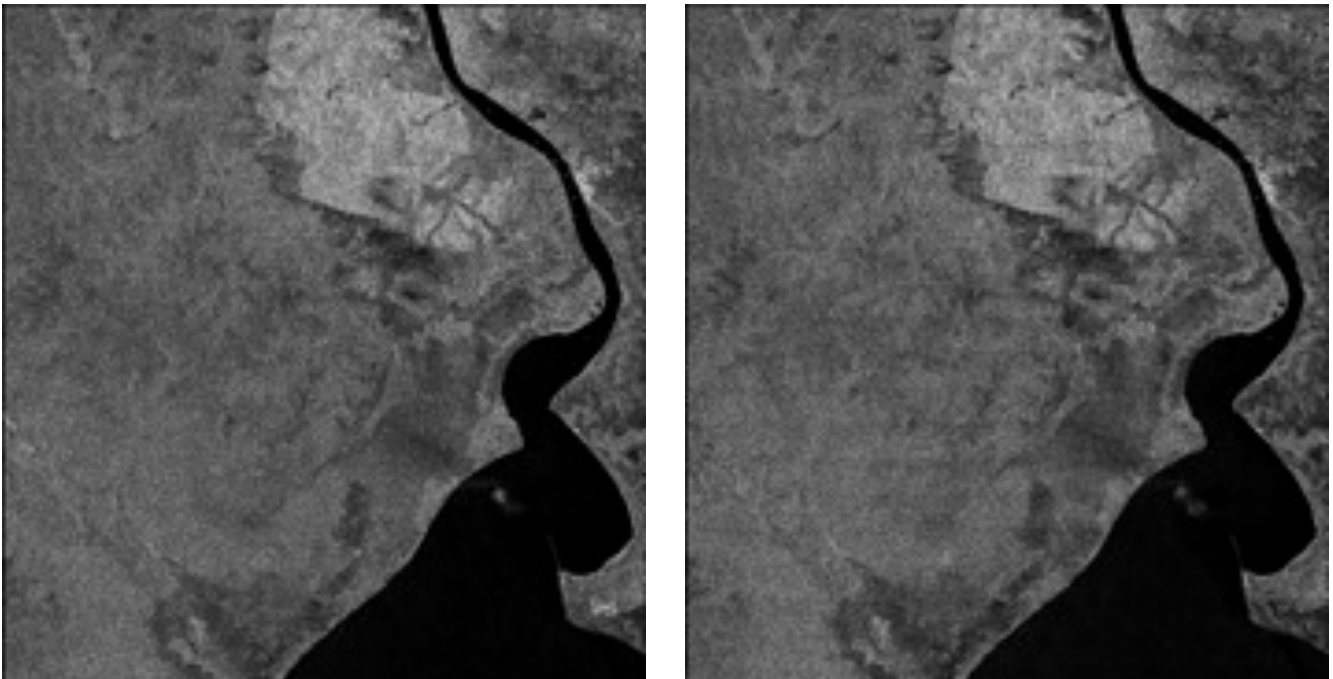


Fig. 3. 11: COSMO-SkyMed data acquired on December 1, 2013. At left is reported the HH polarization channel, while the VV polarization channel at right.

The last couple of figures report the data of the TerraSAR-X system over the same Indonesian area, acquired on March 13, 2008, and provided by Astrium-GEO for free as test images of an educational software for polarimetric analysis.

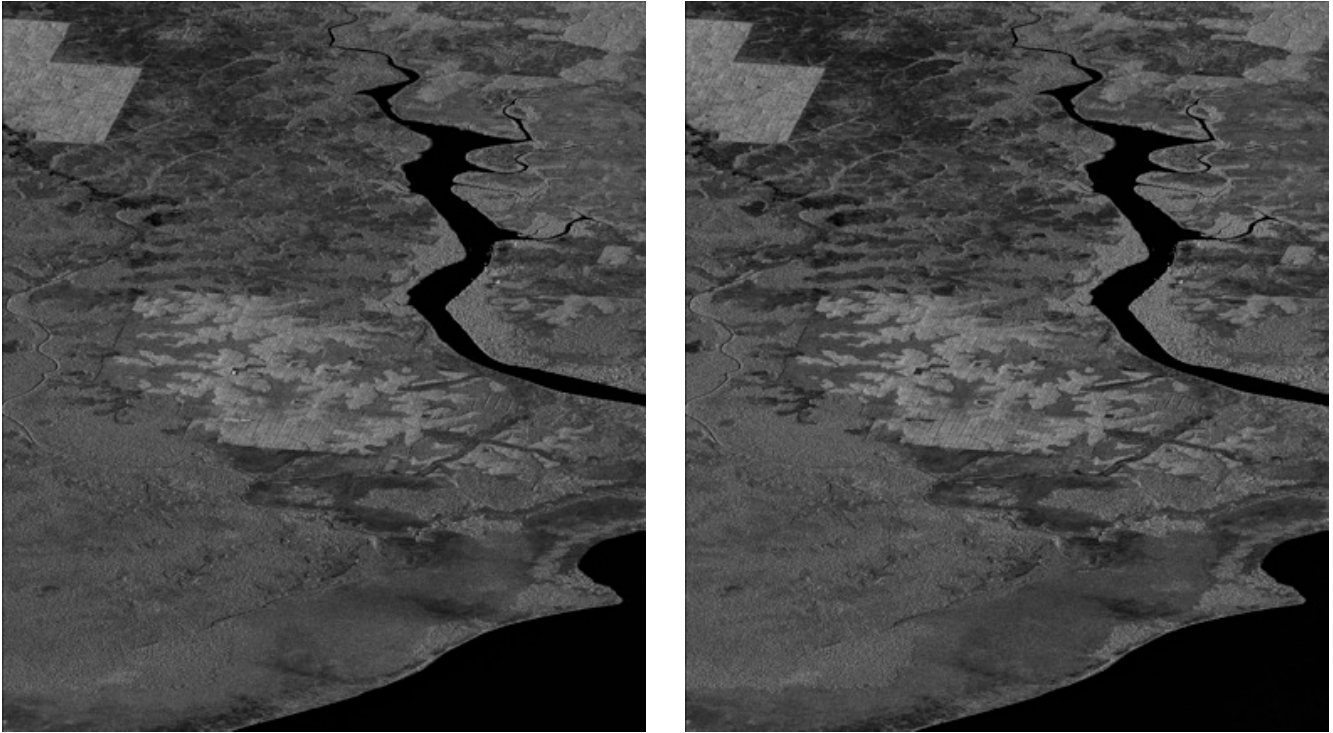


Fig. 3. 12: TerraSAR-X data acquired on March 13, 2008. At left is reported the HH polarization channel, while the VV polarization channel at right.

After these initial stages of processing the images are ready to be submitted to the analysis that is the subject of this research.

### ***3.2.2 Data set Analysis***

In order to demonstrate SAR system capability of soil moisture study, the first test conducted was to relate the backscattering data of archive images to the soil moisture information at the acquisition time. Unfortunately for the Gulf of Naples site, in the time interval of the acquisition, i.e. from 2008 to 2011, there are no catalogues of soil moisture ground measurement (or dielectric constant, or soil properties) for the interesting area.

To overcome this limitation, when choosing images to be required, it has been paid attention to the weather conditions at the acquisition time; moreover those images were chosen so that the weather conditions were kept constant in the days preceding the acquisition.

As depicted in Chapter 1, the microwave radiation can penetrate only few centimetres into the surface (from 1 to 5 cm); as a consequence we can estimate the value of dielectric constant (the interesting parameter for this application) of this thick soil layer. It can be easy to understand that, in general, in a thin layer of soil there are significant variations in the level of moisture due to several factors, either

directly (variation in weather conditions, presence of wind, humidity more or less strong, sunny day) and indirect (changes due to human activities, geological activity or natural events).

As the acquisition is instantaneous, it can be surely affirmed that choosing images of areas where the weather has remained unchanged for at least 3 days before the acquisition, the moisture values are those actually present in the area and therefore detected.

The weather conditions, for the area of Gulf of Naples, are investigated and were arbitrarily assigned values from 1 to 4 on the weather in the days of acquisition, where 1 stands for a moist condition and 4 stands for a dry condition:

- December 2, 2008; storm, value 1
- May 11, 2009; cloudy, value 3
- September 8, 2009; clear, value 4
- September 16, 2009; rain, value 2
- June 22, 2011; clear, value 4

The performance of this data is shown in the following chart (Fig. 3. 13).

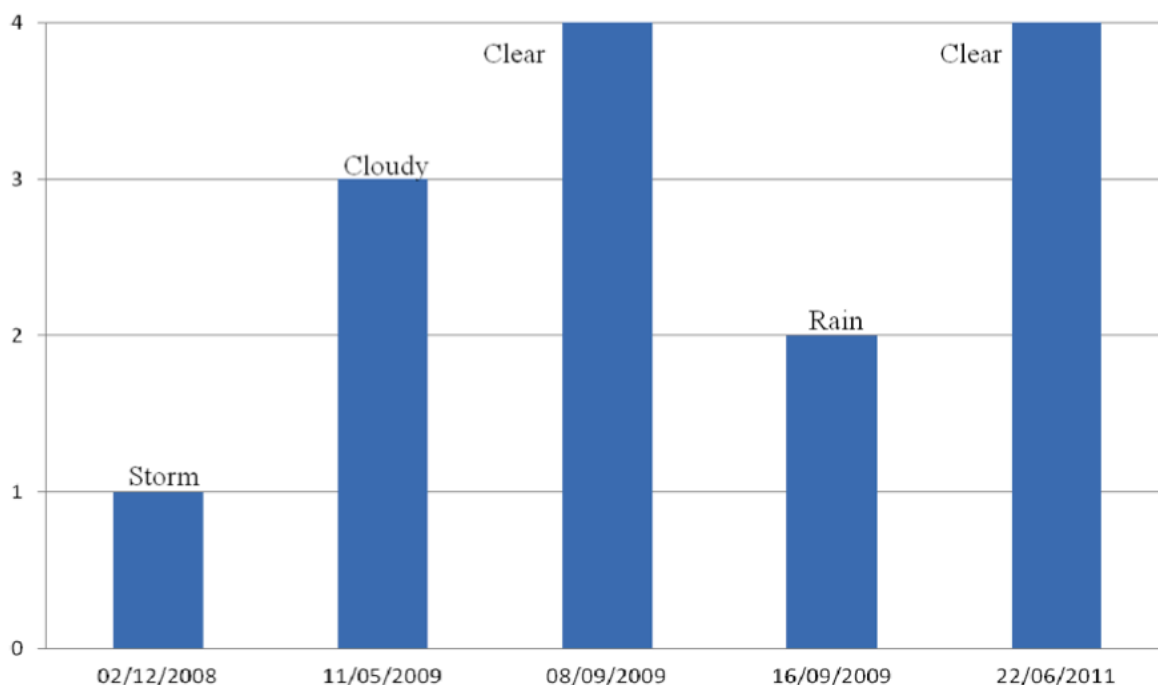


Fig. 3. 13: Weather trend for the archive data of COSMO-SkyMed satellite system.

Once obtained the estimated weather (and as a consequence the moisture) trend, it has been put in relation to the SAR data. Because all the known soil moisture retrieval models use a co- or cross-polarization backscattering coefficients ratio, the following step was the calculus of these ratios and the measurement of mean and standard deviation values. The results of this measurement are reported in Tab. 3. 4, and plotted in Fig. 3. 14.

Acquisition Date	Mean	Standard Deviation
02/12/2008	2.33	4.02
11/05/2009	2.81	5.53
08/09/2009	2.91	5.75
16/09/2009	2.52	4.77
22/06/2011	2.93	6.12

Tab. 3. 4: Mean and standard deviation values for the co-polarized backscattering coefficients.

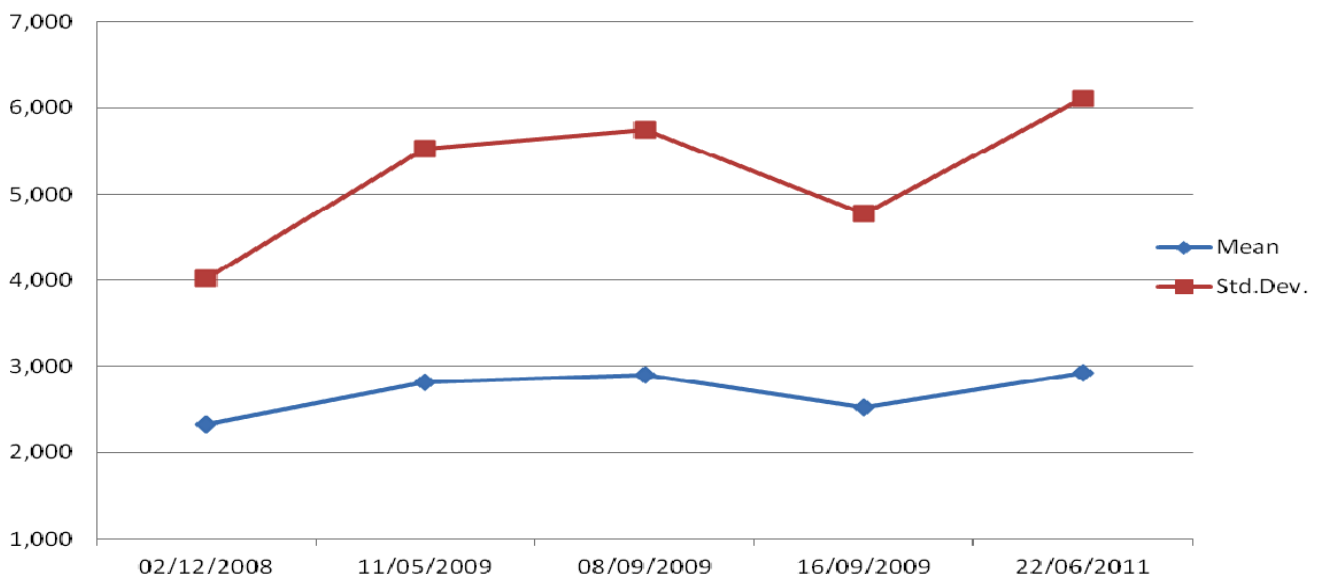


Fig. 3. 14: Mean and standard deviation trend of co-polarized backscattering coefficients ratio.

Looking at Fig. 3. 13 and Fig. 3. 14 we can note some analogies in the trend of these two plots: where the assigned values of moisture are low, also the mean and standard deviation values are low. On the other hand where the moisture has high values, also the mean and standard deviation have high values; these trend variations follow the variations of the weather trend.

This result permits us to say with reasonable certainty that there is a close link between the data acquired through microwave SAR sensors and soil characteristic parameters, as the moisture parameter is.

### 3.2.3 Data set Coherence Analysis

All of the images presented in section 3.1, are subsequently analysed measuring the polarimetric complex coherence.

As illustrated in Chapter 1, this parameter is an index of correlation between the two polarization channels of the image.

The adopted formula is that reported in Section 1.5 (in eq. 1.35, and synthesized in the following relation), where in place of  $j_1$  and  $j_2$  were replaced the HH and VV channels data:

$$\gamma = \frac{\langle j_1 j_2^* \rangle}{\sqrt{\langle j_1 j_1^* \rangle \langle j_2 j_2^* \rangle}} \quad (3.2)$$

As reported in Caltagirone F. et al. (2012), the COSMO-SkyMed system at present can acquire multi-polarimetric images only in a “PINGPONG Mode” (“alternating” or “burst” polarimetric mode) with no coherent phase information between the polarimetric channels.

This behaviour is confirmed by the measurements performed on the COSMO-SkyMed Ping-Pong data set as it is shown in the following charts.

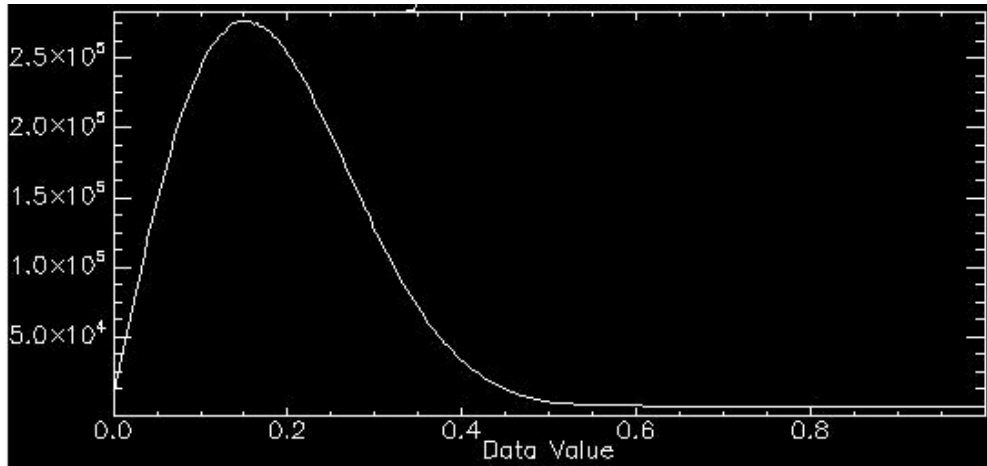


Fig. 3. 15: Coherence histogram for the data acquired on December 2, 2008.

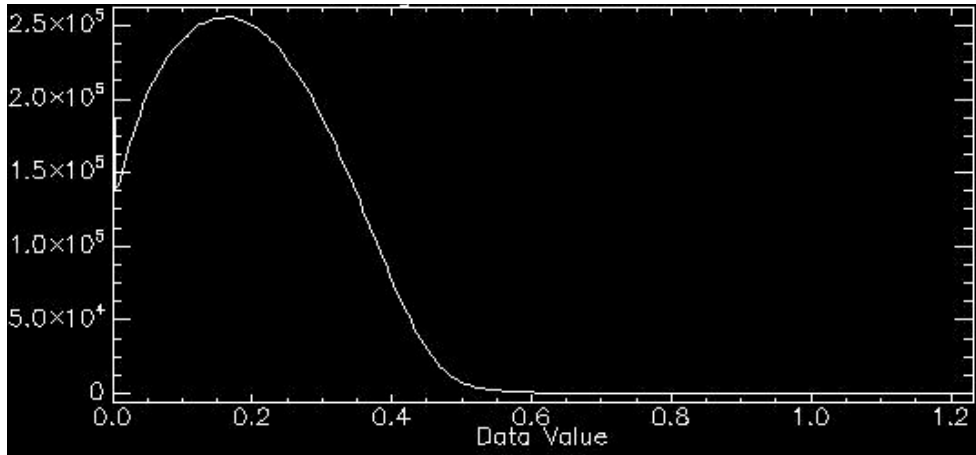


Fig. 3. 16: Coherence histogram for the data acquired on May 11, 2009.

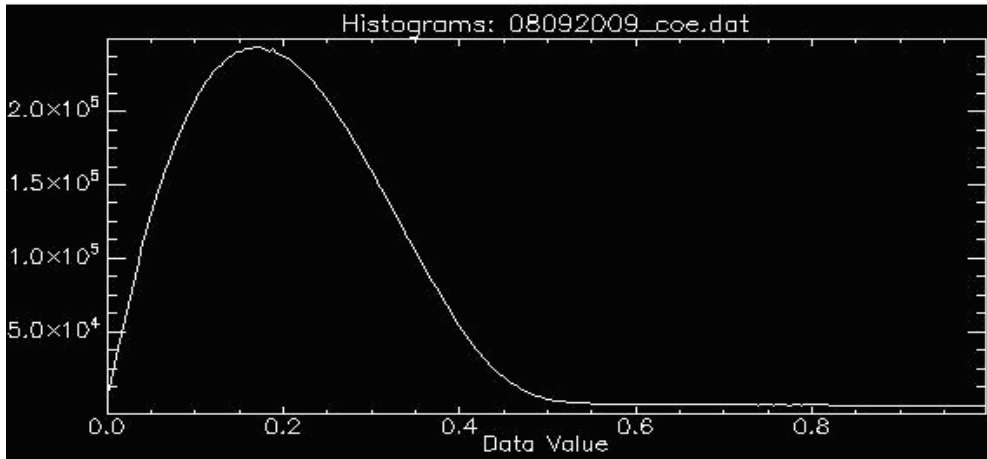


Fig. 3. 17: Coherence histogram for the data acquired on September 8, 2009.

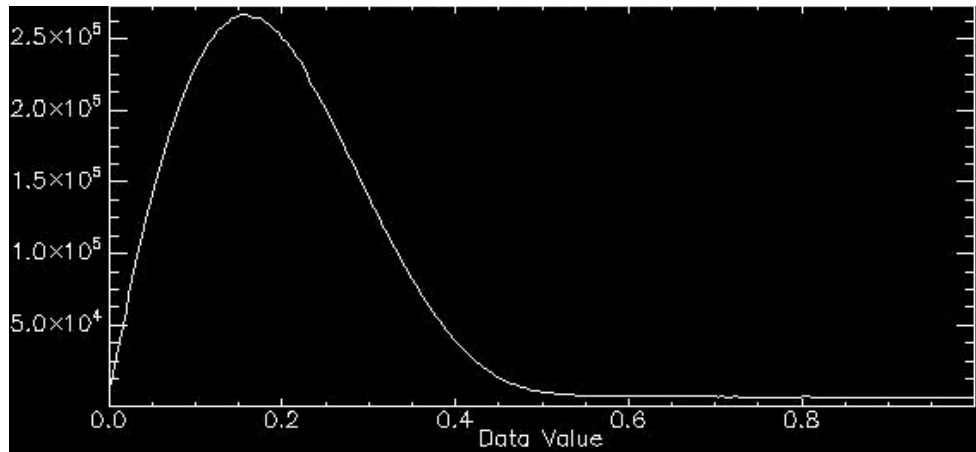


Fig. 3. 18: Coherence histogram for the data acquired on September 16, 2009.

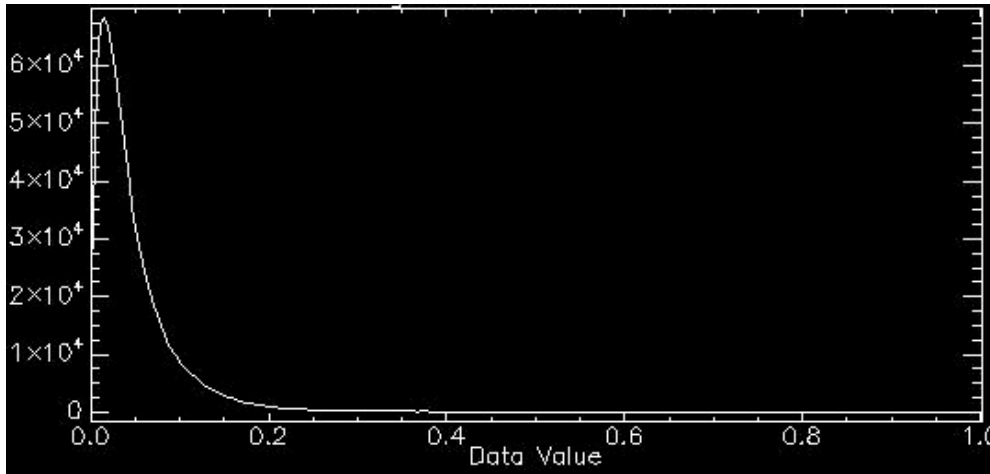


Fig. 3. 19: Coherence histogram for the data acquired on June 22, 2011.

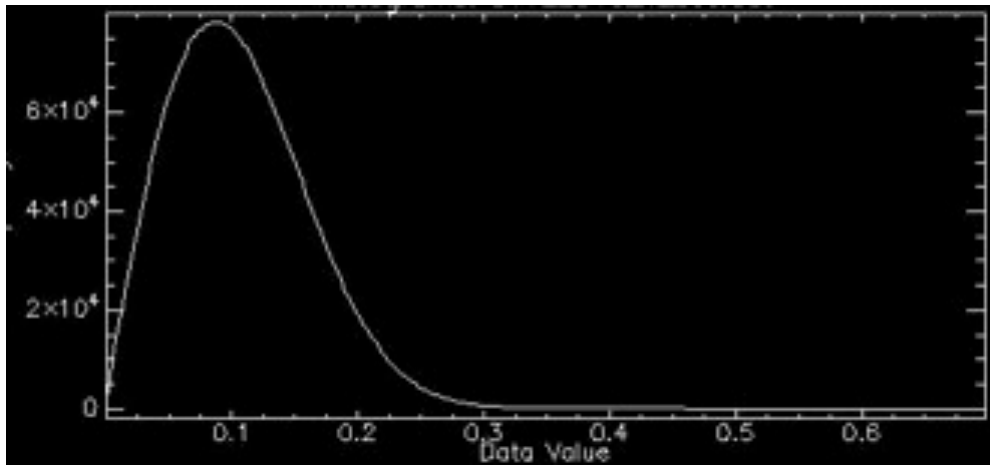


Fig. 3. 20: Coherence histogram for the data acquired on December 1, 2013 (a).

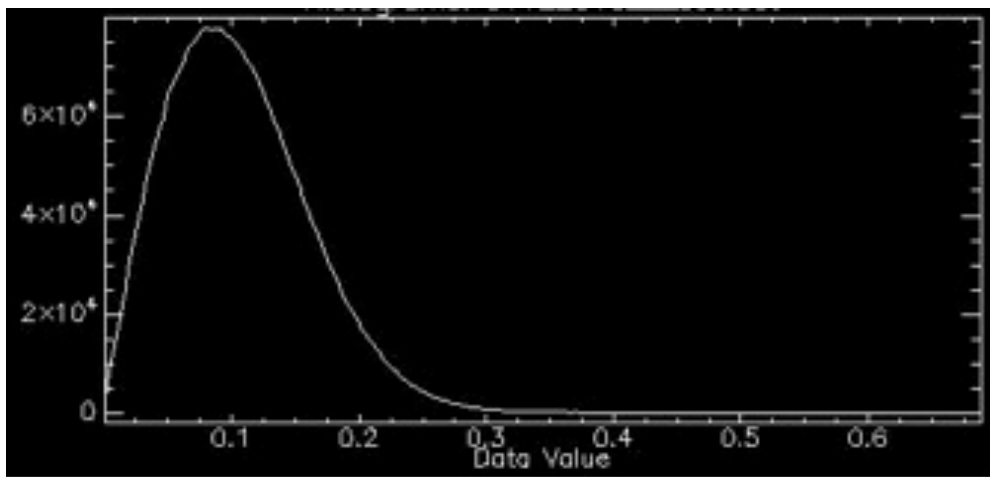


Fig. 3. 21: Coherence histogram for the data acquired on December 1, 2013 (b).

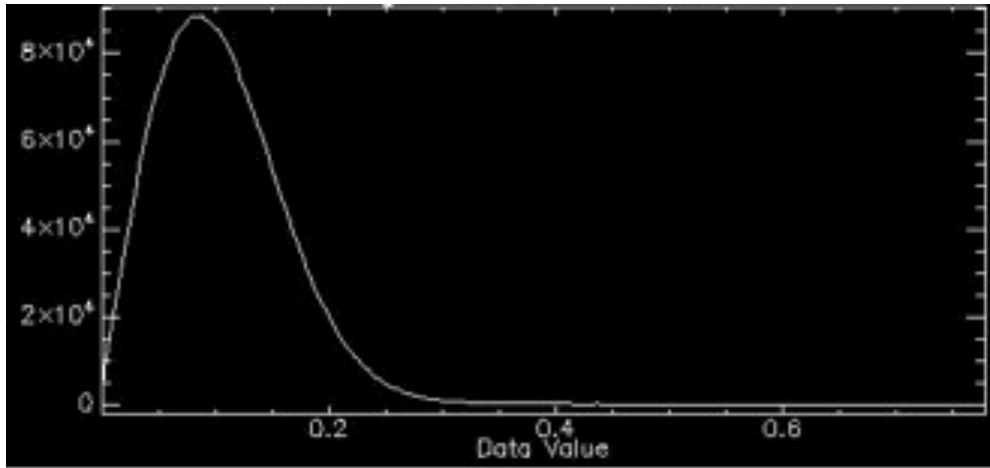


Fig. 3. 22: Coherence histogram for the data acquired on December 1, 2013 (c).

As we can see, the mean values of coherence stood under 0.3, and this leads to the foreseen poor correlation between the two polarization channels.

As an additional exercise, the same measurements have been performed on polarimetric data, acquired by TerraSAR-X system, through coherent Stripmap mode (both the H and V channels are simultaneously acquired at receiver). These data were analysed about their coherence parameter, and this test has led to the histogram of coherence, which is reported in Fig. 3. 23.

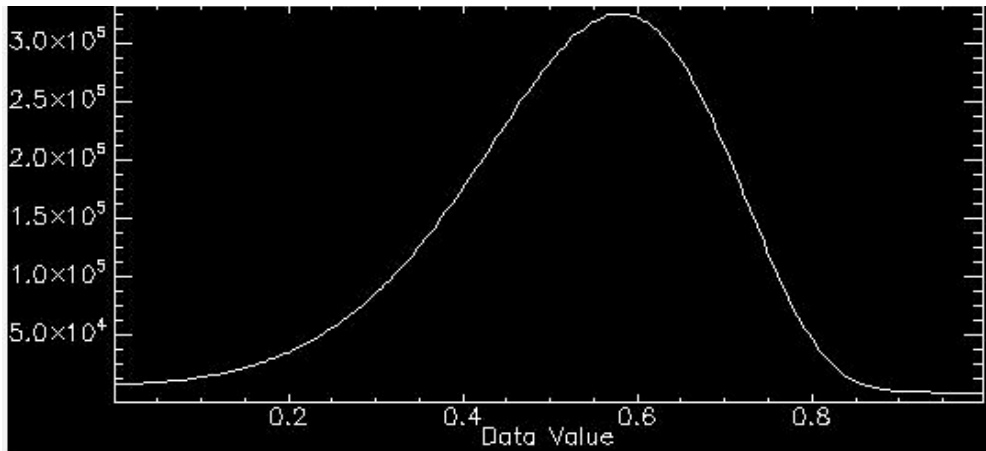


Fig. 3. 23: Coherence histogram for the data acquired on March 13, 2008 by TerraSAR-X system.

This plot shows a mean coherence value around 0.6, that is index of correlation between the two polarization channels of the data (HH and VV channel). For this data was also possible to calculate a coherence map, that is shown in the following figures.

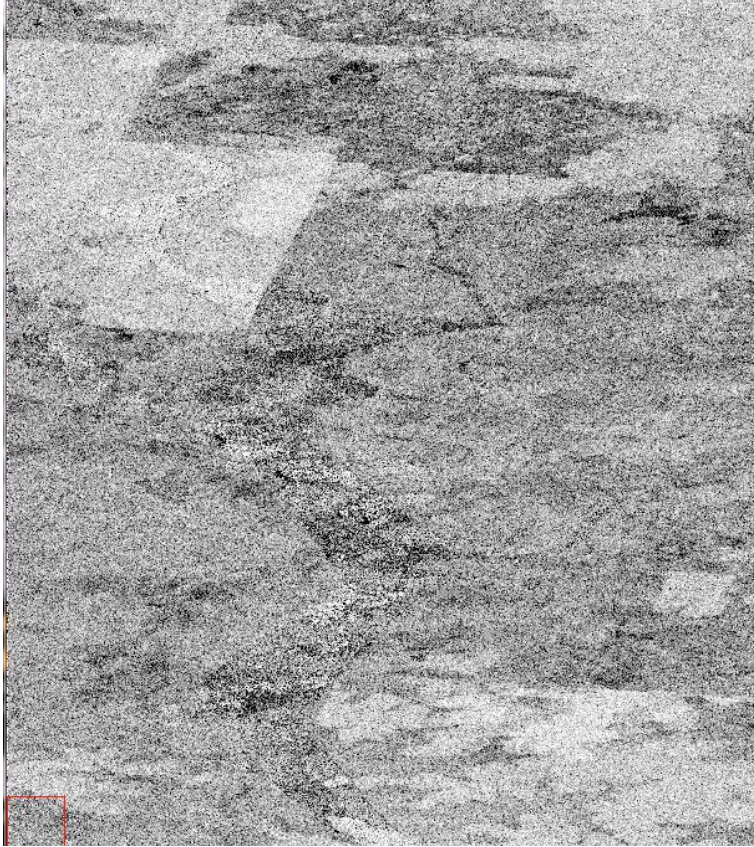


Fig. 3. 24: Coherence map for the image acquired by TerraSAR-X system, on March 13, 2008

As expected for a coherent data, it is possible to identify areas in the coherence map where the values are higher (lighter pixels), specifically the areas where the vegetation is lower (cultivated field, for example).

### ***3.3 Soil moisture maps***

The following phase of this research was the evaluation of a soil moisture map.

A new algorithm, starting by the Dubois model (Dubois P.C. et al., 1995), was implemented and tested on the available data, taking into account the equations for the polarimetric backscattering coefficients provided by Dubois (eq. 2.12 and 2.13), and the inversed equation from the dielectric constant to soil moisture parameter provided by Topp (Topp et al., 1980: eq. 2.10).

During the implementation stages the tiny variation of incidence angle during the acquisition has been taken into account. The SAR geometry acquisition involves an angle variation ranging from a near value of an angle to a far value.

These ranges vary for each SAR system: for COSMO-SkyMed SAR system this variation in the incidence angle is about  $2.18^\circ$  from near to the far angle, while for the TerraSAR-X SAR system is about  $1.5^\circ$ .

Once ended the implementation phase, the resulting program was tested on the available data and have been produced the soil moisture maps shown in the following figures.



Fig. 3. 25: Soil moisture map for the COSMO-SkyMed image acquired on December 2, 2008.

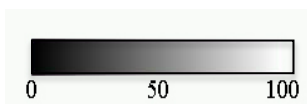


Fig. 3. 26: Soil moisture map for the COSMO-SkyMed image acquired on May 11, 2009.



Fig. 3. 27: Soil moisture map for the COSMO-SkyMed image acquired on September 8, 2009.

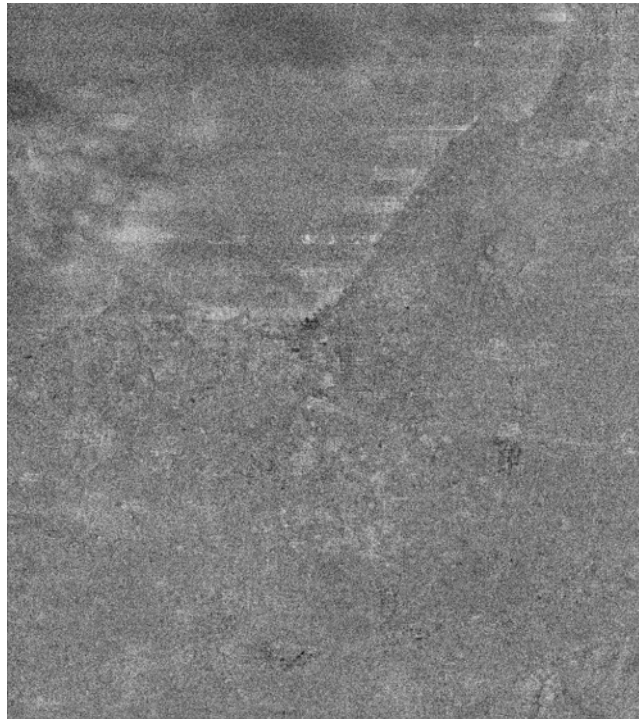


Fig. 3. 28: Soil moisture map for the COSMO-SkyMed image acquired on September 16, 2009.

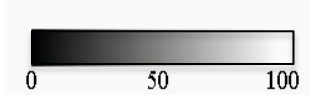


Fig. 3. 29: Soil moisture map for the COSMO-SkyMed image acquired on June 22, 2011.

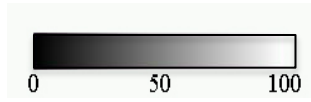
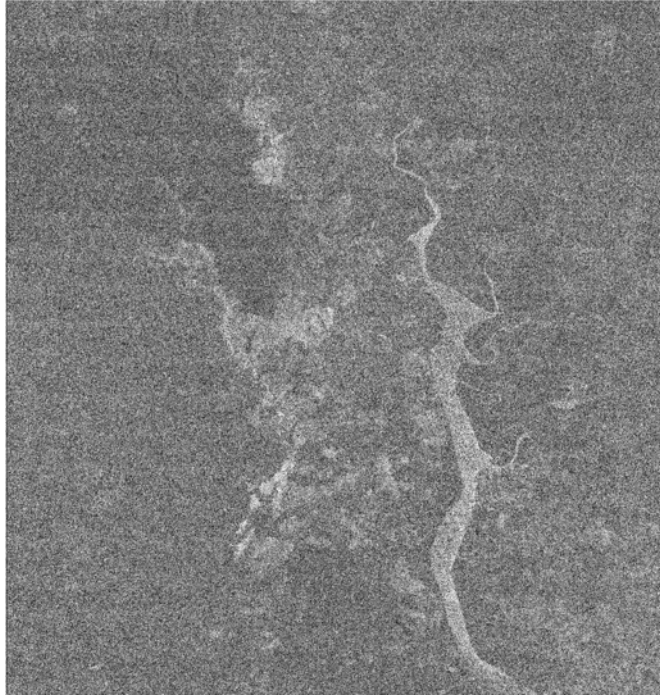


Fig. 3. 30: Soil moisture map for the COSMO-SkyMed image acquired on December 1, 2013 (a).

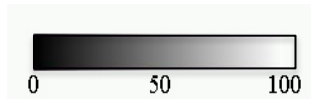


Fig. 3. 31: Soil moisture map for the COSMO-SkyMed image acquired on December 1, 2013 (b).

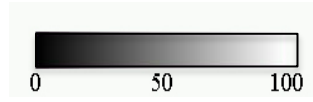
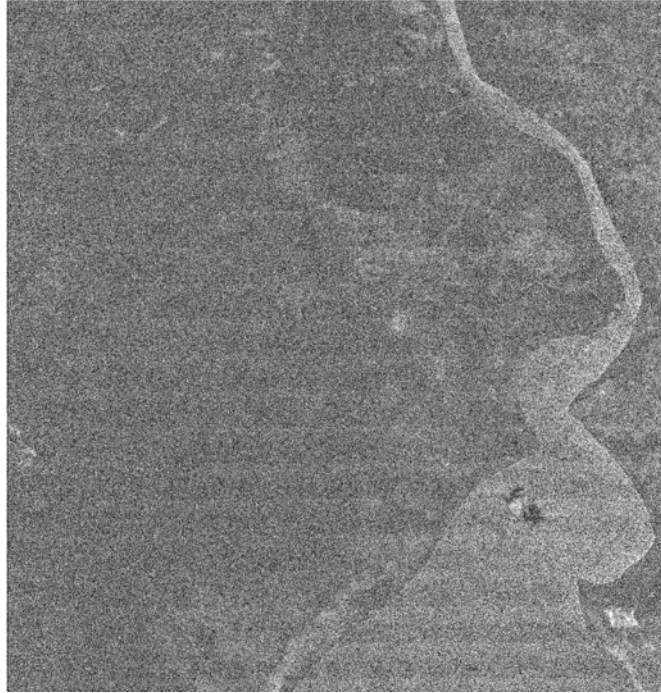


Fig. 3. 32: Soil moisture map for the COSMO-SkyMed image acquired on December 1, 2013 (c).

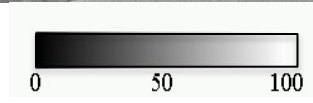


Fig. 3. 33: Soil moisture map for the TerraSAR-X data acquired on March 13, 2008.

The maps obtained for the COSMO-SkyMed archive data show the presence of an almost homogeneity in the pixel values. This result is probably due to a combination of factors: the limitation of the soil moisture retrieval model on the rms height of surface, which were not respected in the area of Gulf of Naples; the presence of a great amount of water nearby the interested area; a lack of coherence due to geometry acquisition, and a few brilliant scatterers on the area; a large amount of vegetation that afflicts the backscattered signal, etc.

### ***3.4 Study on radar sensitivity***

During this work it has also been analysed the sensitivity required by the Dubois Model. Collaboration with Thales Alenia Space (Rome group), has allowed us to estimate the backscattering coefficient values given by the Dubois model, with its varying different parameters (rms surface height, dielectric constant and incidence angle, in the range of COSMO-SkyMed system operation). These results were then related to the sensitivity of the radar sensor of COSMO-SkyMed system, in order to identify the best configuration for a soil moisture study through COSMO-SkyMed data.

The sensitivity of this SAR system is about -20dB (nominal sensitivity); the incidence angle of observation ranges from 20° to 65°; the radiometric accuracy is about 1dB per channel (2dB for the two co-polarimetric channels).

Referring to the Section 2.3.1, the limits on the surface characteristics imposed by the Dubois model are: 2dB for the radiometric accuracy; a rms surface height ranging from 0.3cm and 3cm; an incidence angle ranging between 30° and 65°.

The dielectric constant parameter can range from 1 to 80 (for a liquid water). Realistic values for surface soil moisture (i.e. soil and water are mixed) range from 2 to 25, from dry to wet soil.

For this analysis the values of rms surface height have been varied, together with the incidence angle and the dielectric constant, in order to evaluate the backscattering coefficients values (in dB); the ranges that have been used are:

- rms surface height ranging between 0.2cm and 5cm (step 0.2cm);
- dielectric constant ranging between 2 and 25 (step 6);
- incidence angle ranging between 30° to 65° (step 1°).

The obtained plots of backscattering coefficients values are reported in the following charts.

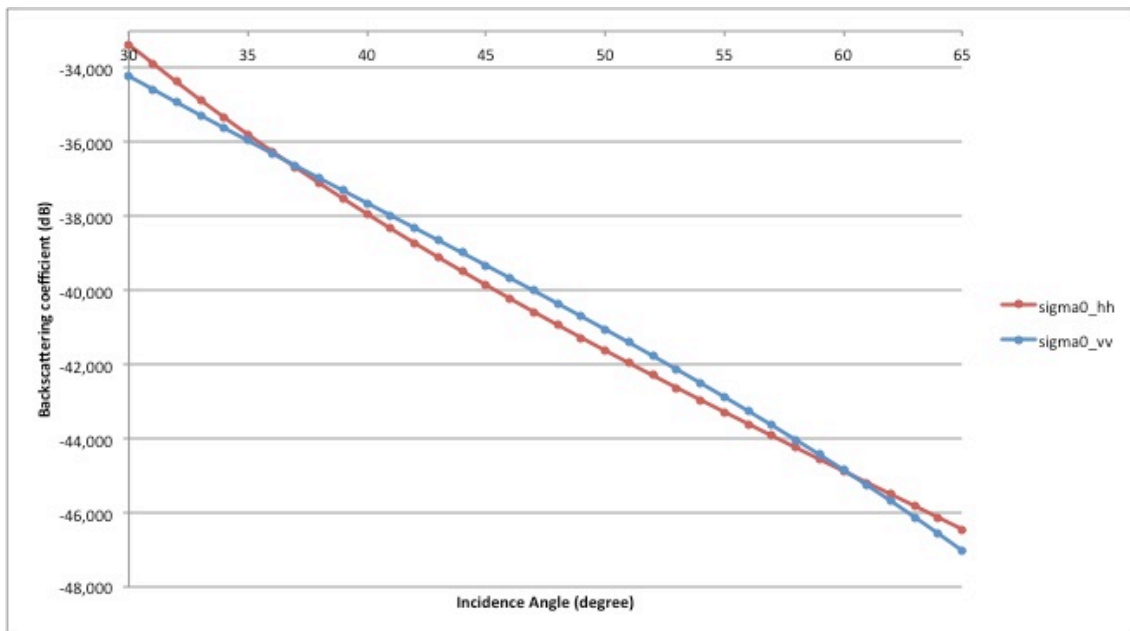


Fig. 3. 34: Sensitivity evaluation for  $h=0.002$  and  $\epsilon=2$ .

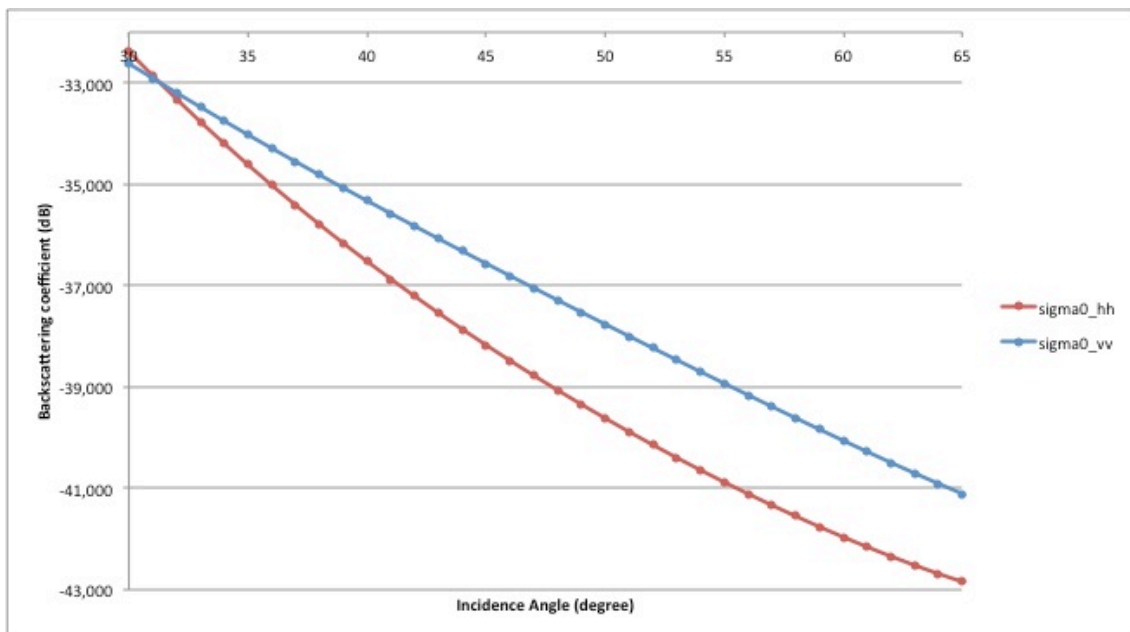


Fig. 3. 35: Sensitivity evaluation for  $h=0.002$  and  $\epsilon=8$ .

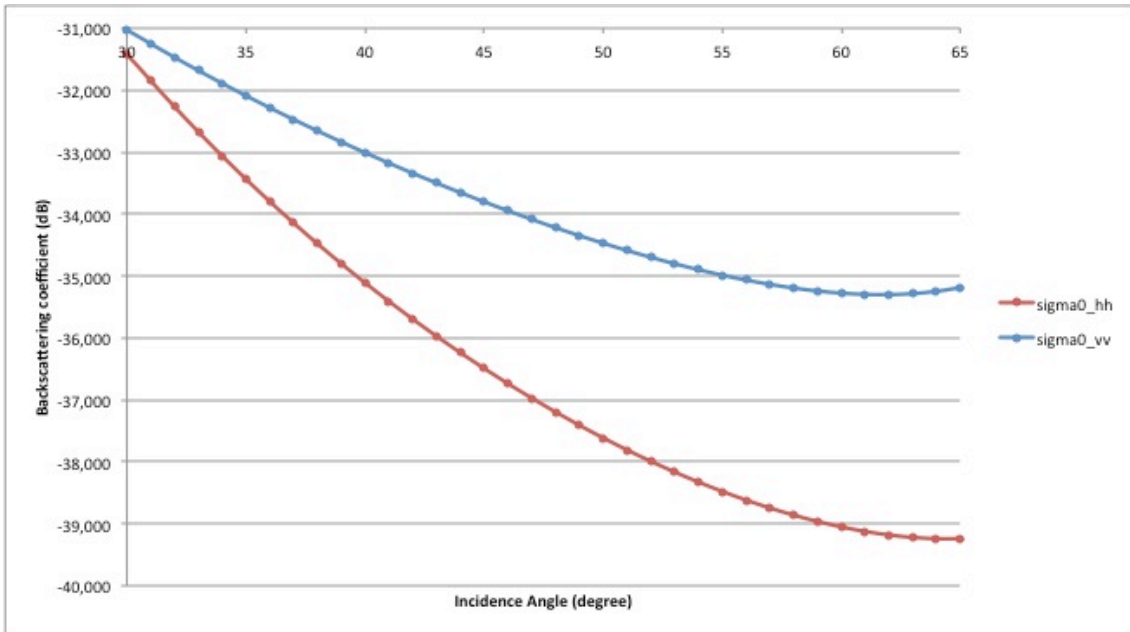


Fig. 3.36: Sensitivity evaluation for  $h=0.002$  and  $\epsilon=14$ .

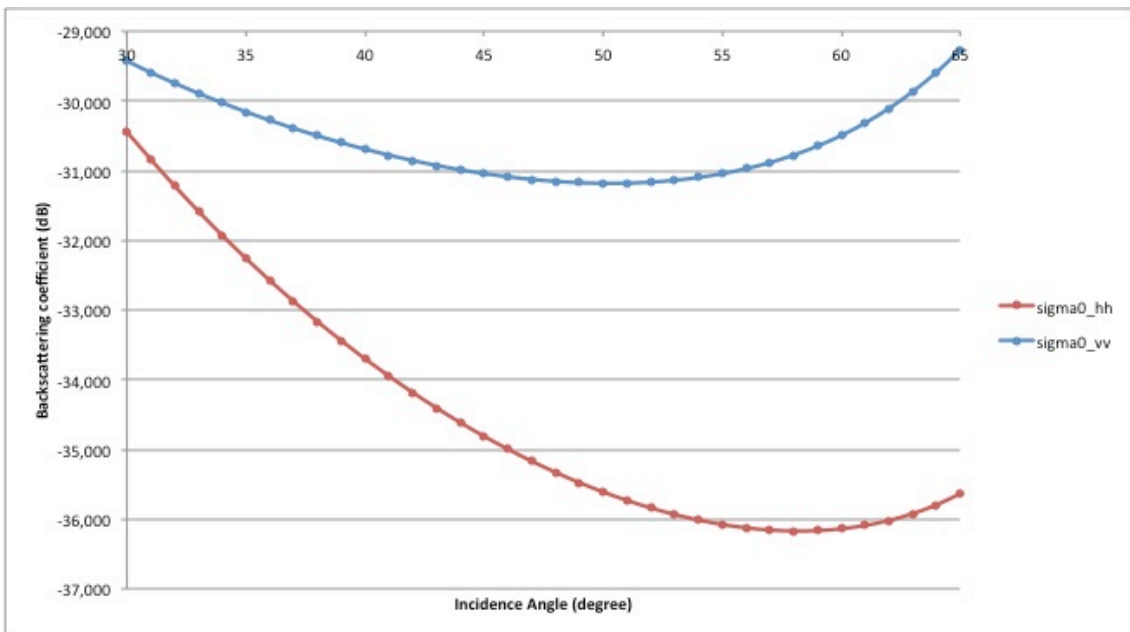


Fig. 3.37: Sensitivity evaluation for  $h=0.002$  and  $\epsilon=20$ .

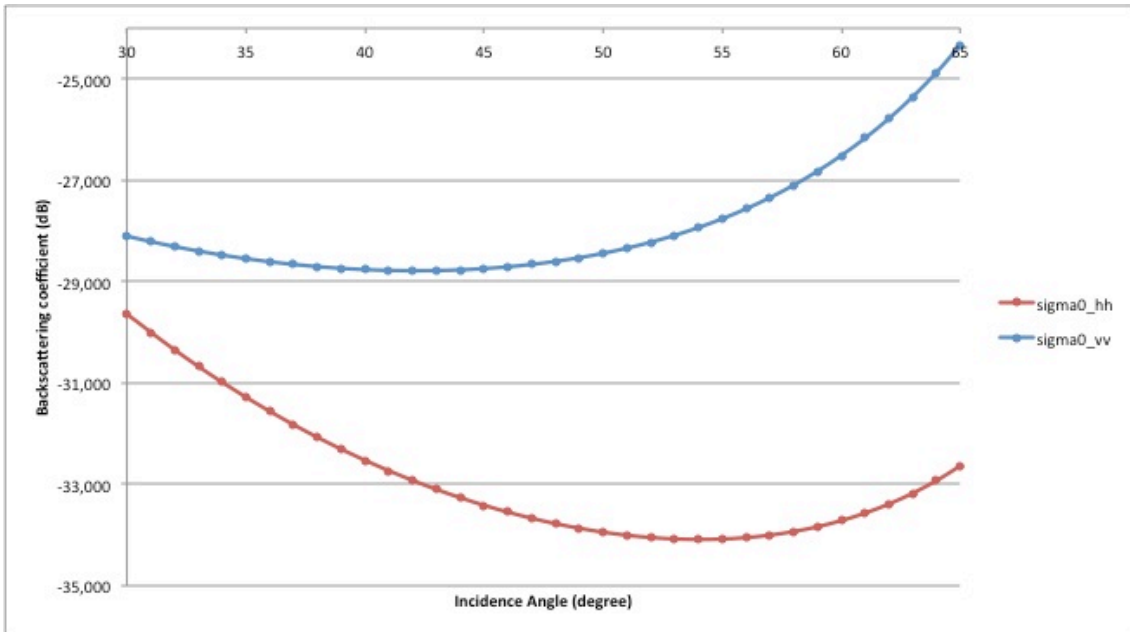


Fig. 3. 38: Sensitivity evaluation for  $h=0.002$  and  $\epsilon=25$ .

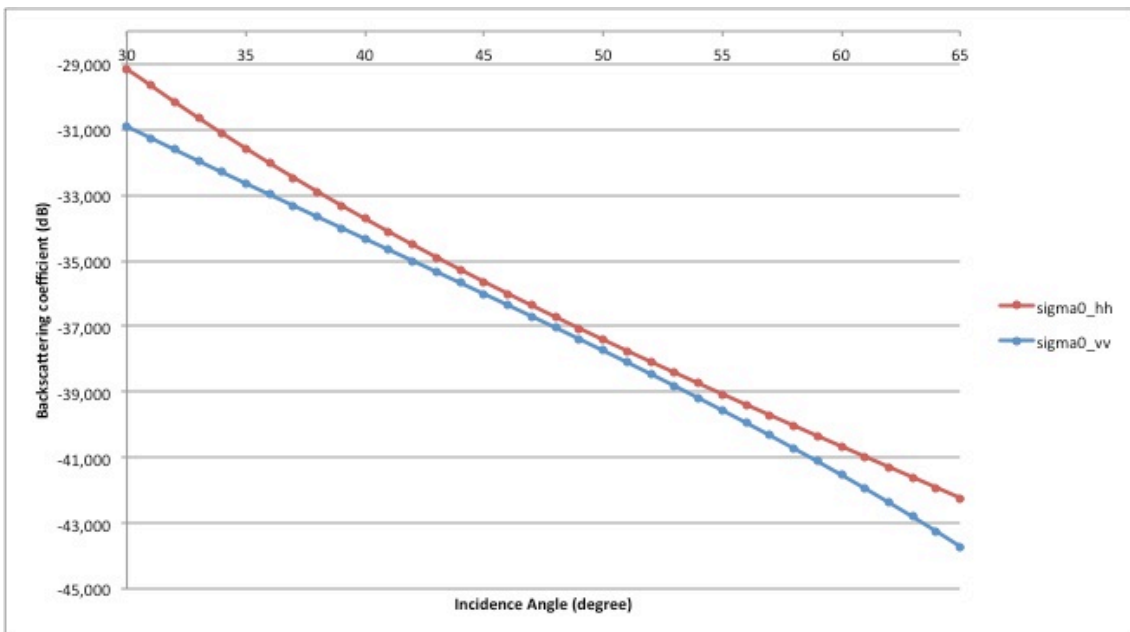


Fig. 3. 39: Sensitivity evaluation for  $h=0.004$  and  $\epsilon=2$ .

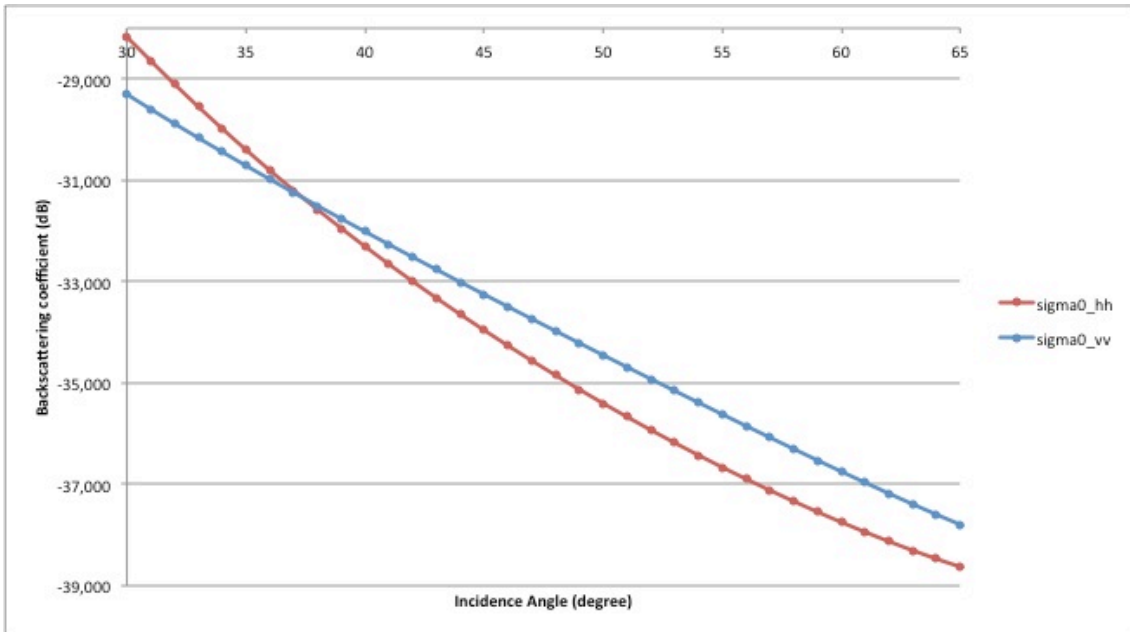


Fig. 3. 40: Sensitivity evaluation for  $h=0.004$  and  $\epsilon=8$ .

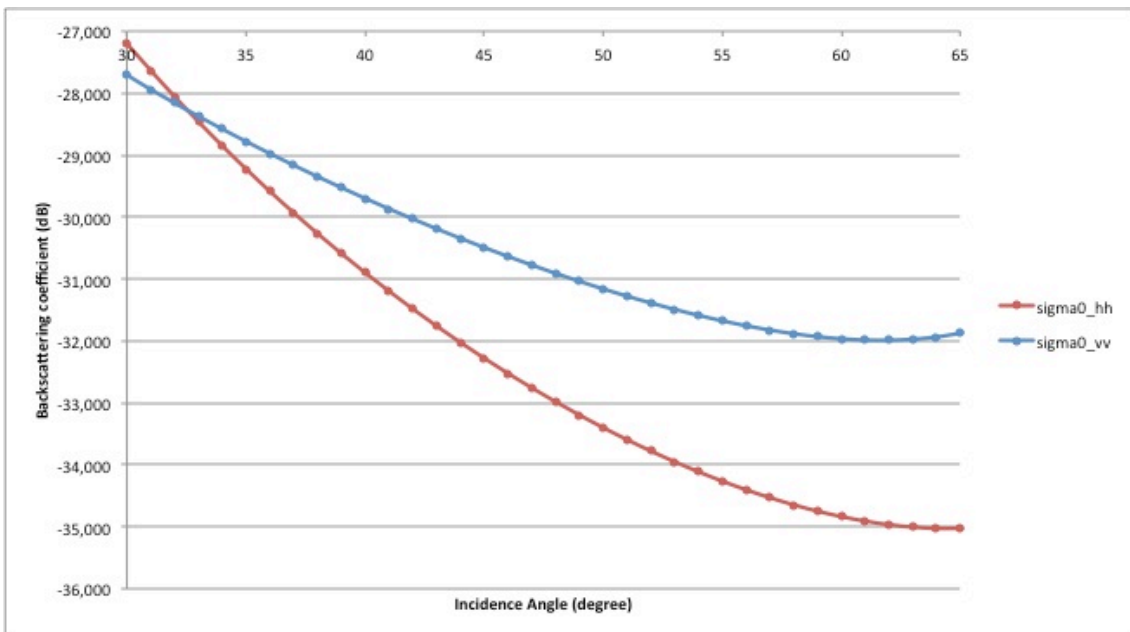


Fig. 3. 41: Sensitivity evaluation for  $h=0.004$  and  $\epsilon=14$ .

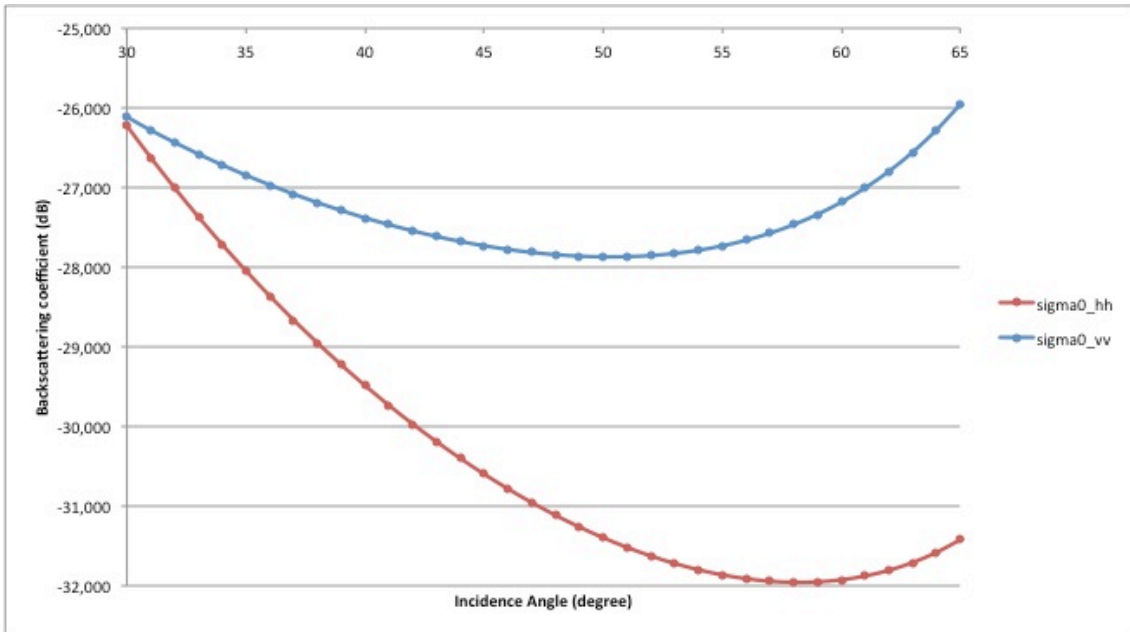


Fig. 3.42: Sensitivity evaluation for  $h=0.004$  and  $\epsilon=20$ .

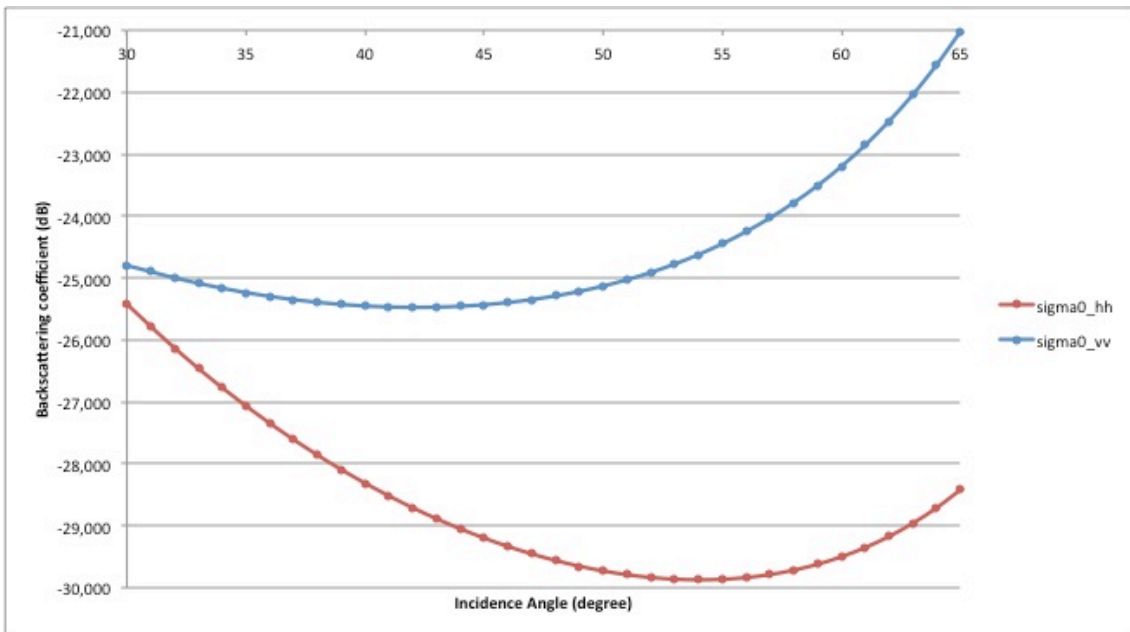


Fig. 3.43: Sensitivity evaluation for  $h=0.004$  and  $\epsilon=25$ .

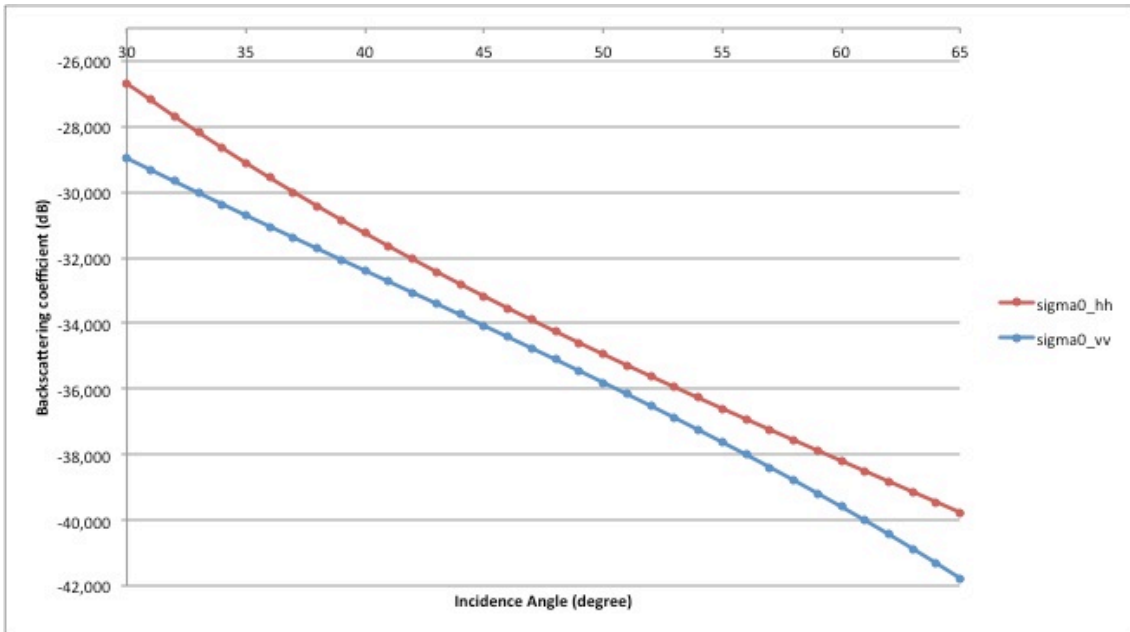


Fig. 3.44: Sensitivity evaluation for  $h=0.006$  and  $\epsilon=2$ .

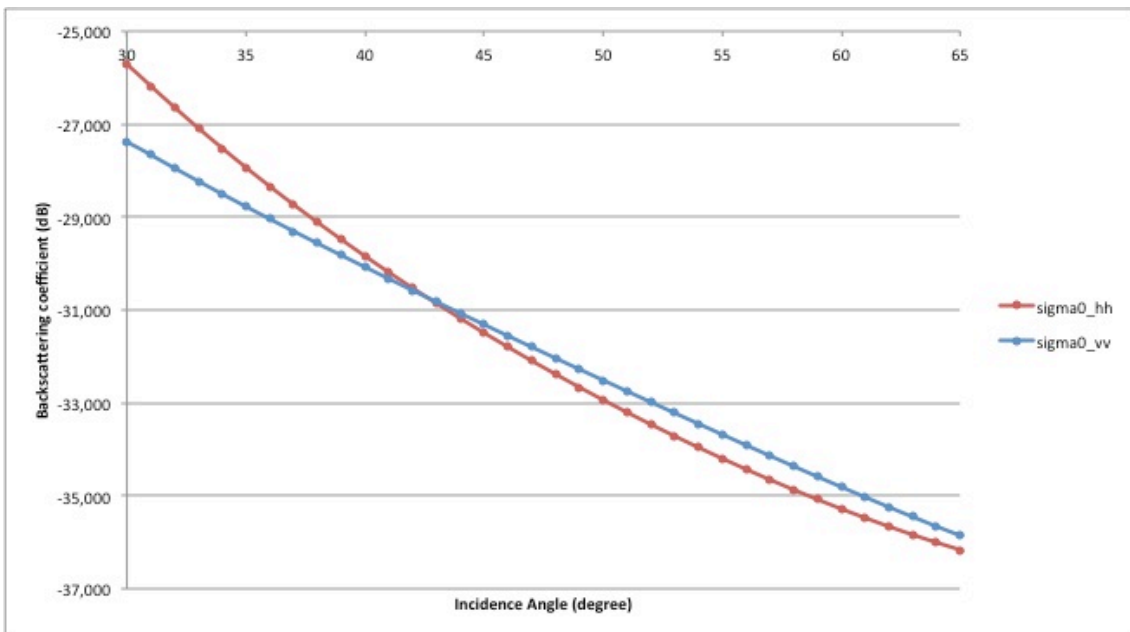


Fig. 3.45: Sensitivity evaluation for  $h=0.006$  and  $\epsilon=8$ .

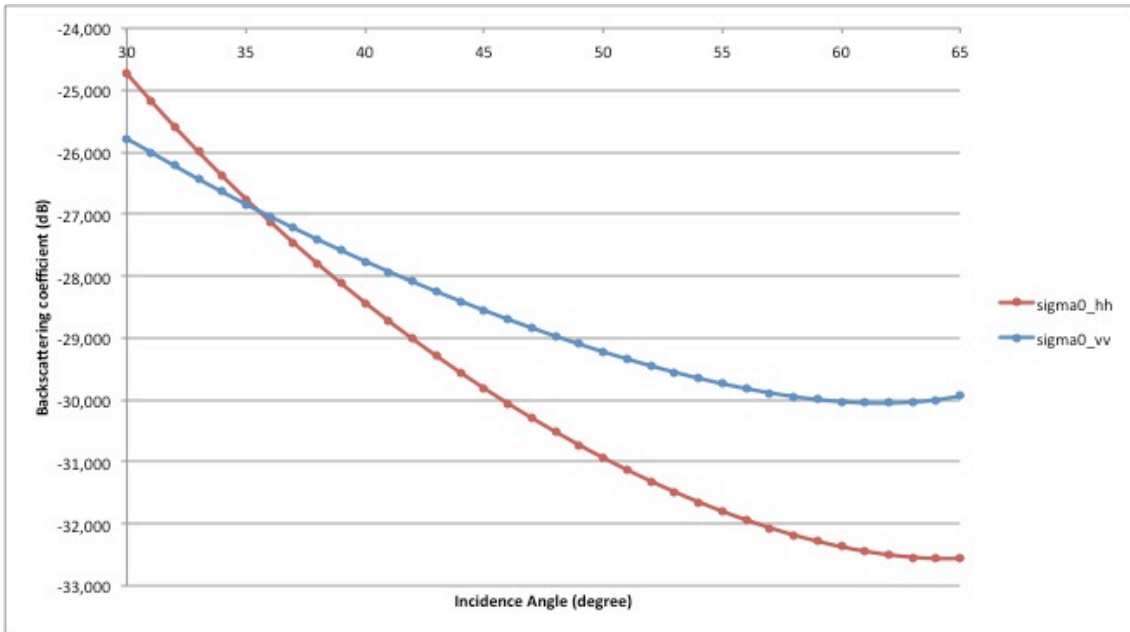


Fig. 3.46: Sensitivity evaluation for  $h=0.006$  and  $\epsilon=14$ .

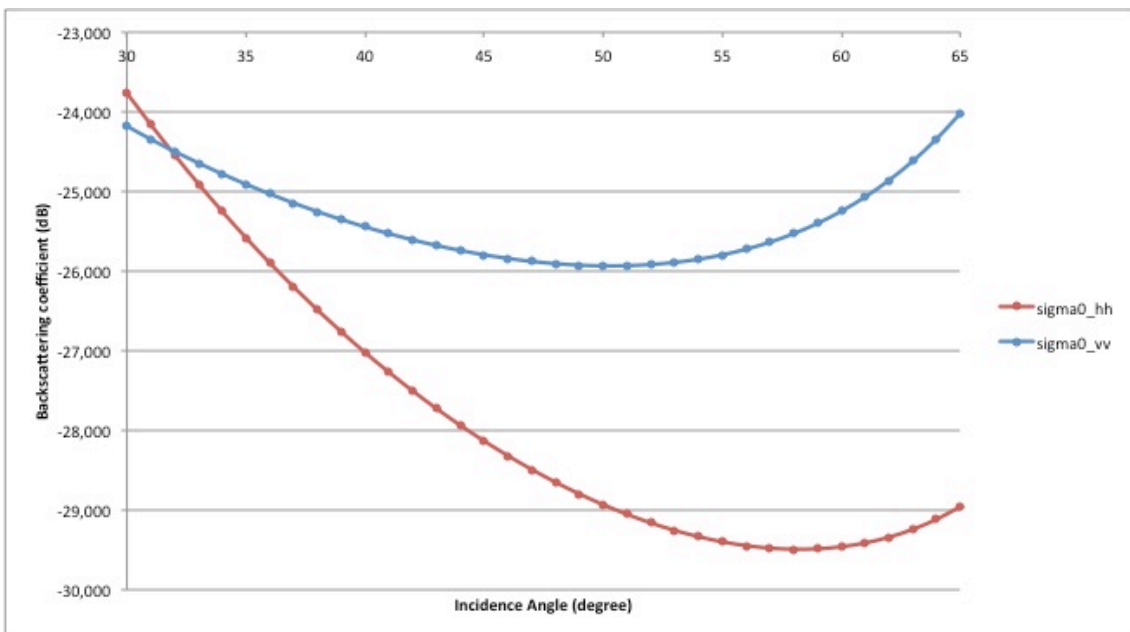


Fig. 3.47: Sensitivity evaluation for  $h=0.006$  and  $\epsilon=20$ .

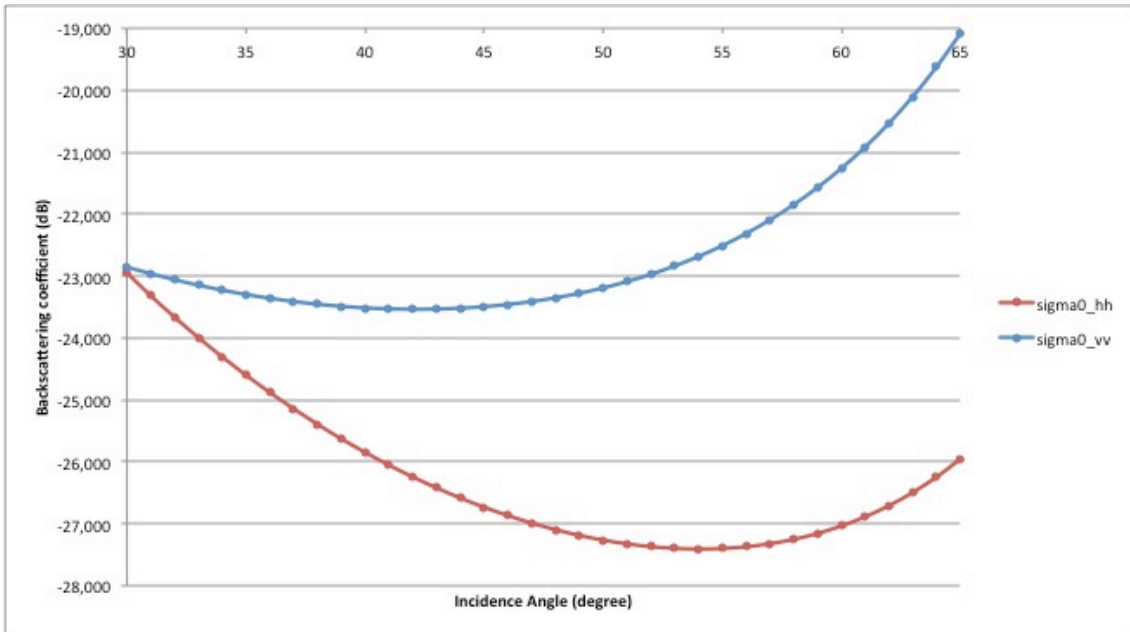


Fig. 3. 48: Sensitivity evaluation for  $h=0.006$  and  $\epsilon=25$ .

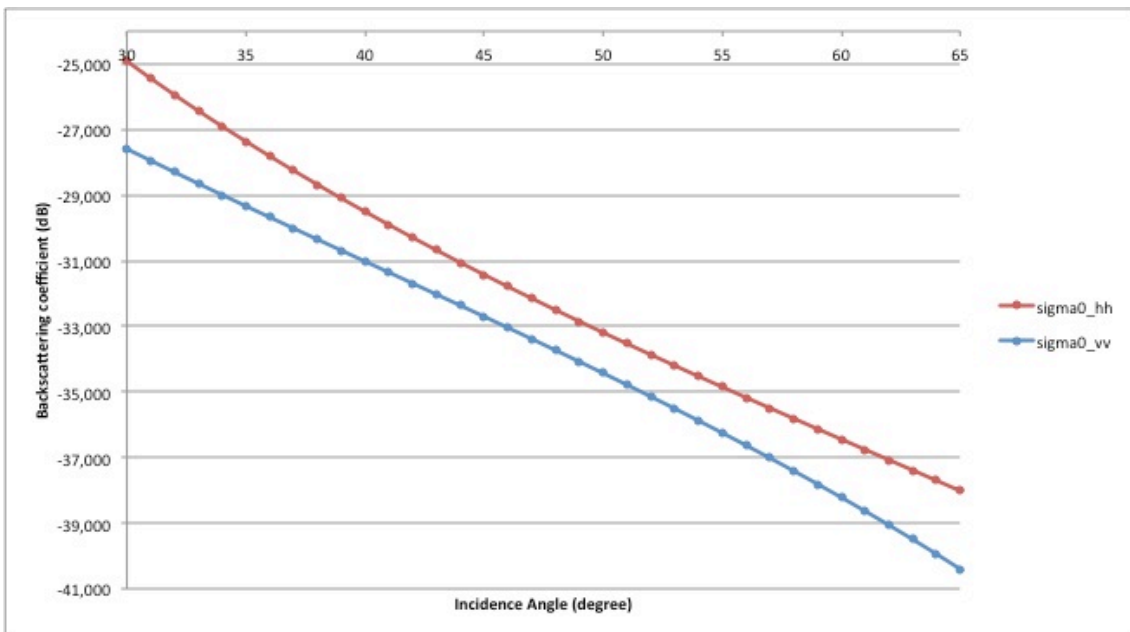


Fig. 3. 49: Sensitivity evaluation for  $h=0.008$  and  $\epsilon=2$ .

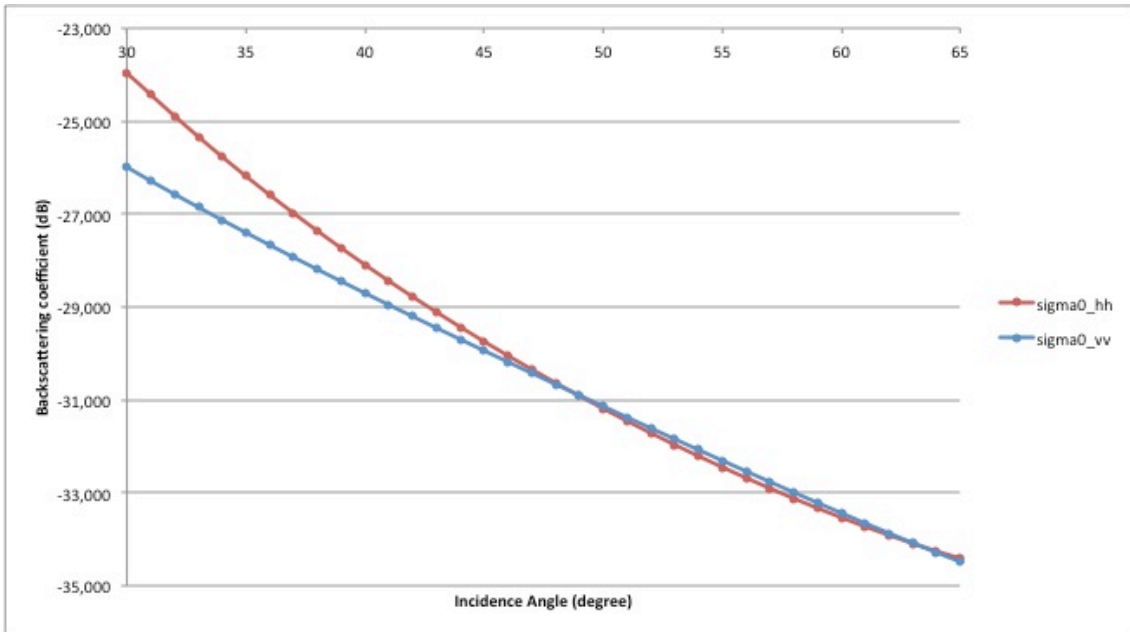


Fig. 3. 50: Sensitivity evaluation for  $h=0.008$  and  $\epsilon=8$ .

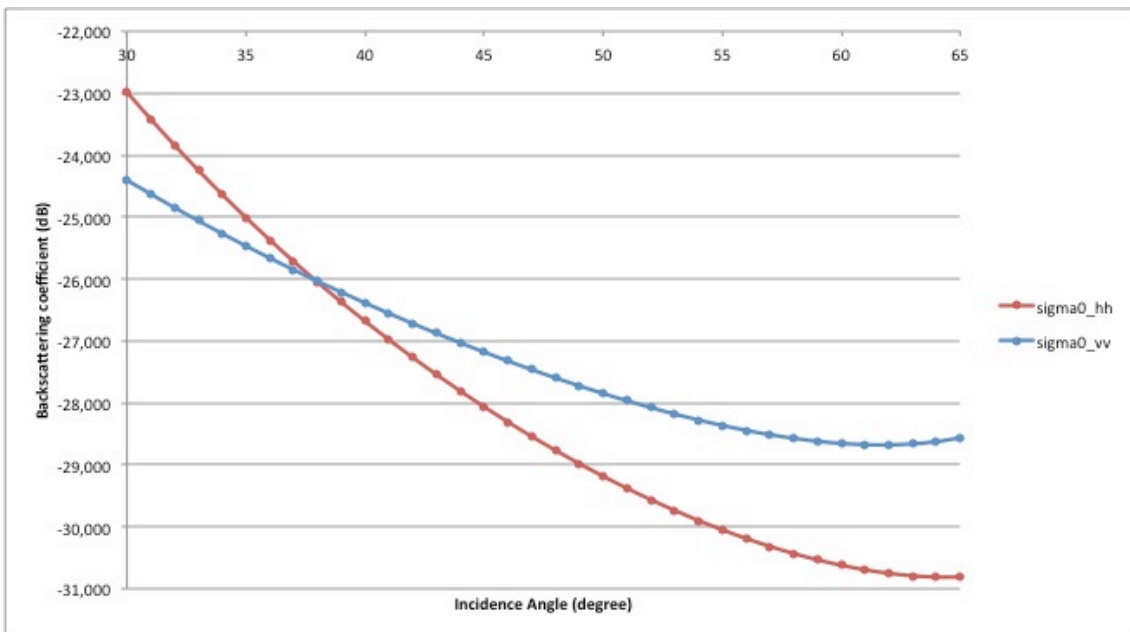


Fig. 3. 51: Sensitivity evaluation for  $h=0.008$  and  $\epsilon=14$ .

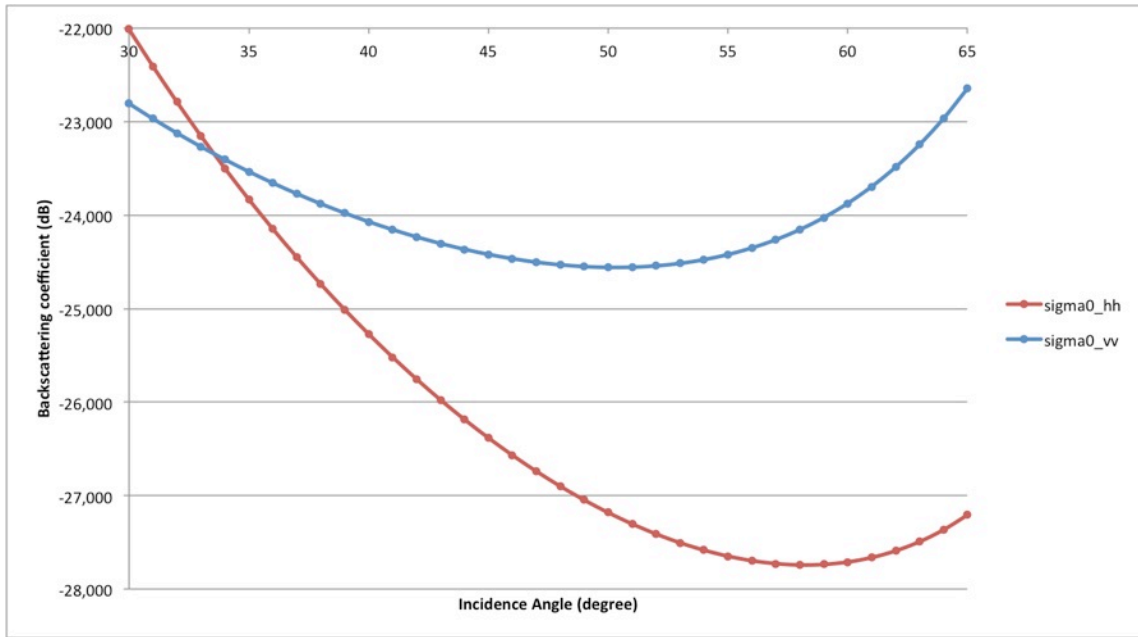


Fig. 3.52: Sensitivity evaluation for  $h=0.008$  and  $\epsilon=20$ .

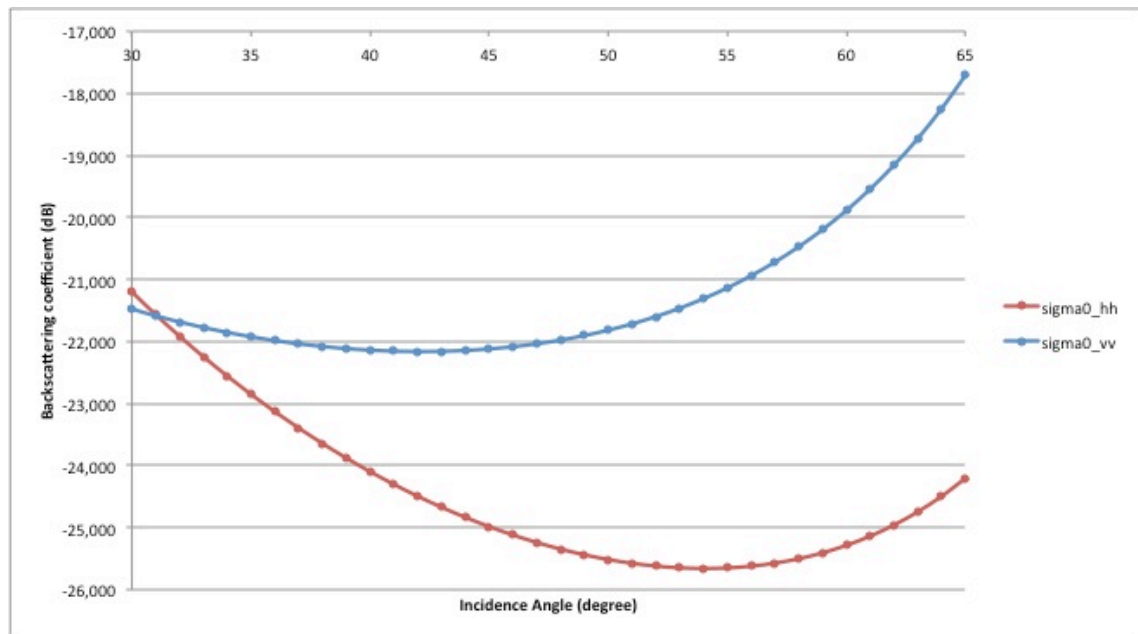


Fig. 3.53: Sensitivity evaluation for  $h=0.008$  and  $\epsilon=25$ .

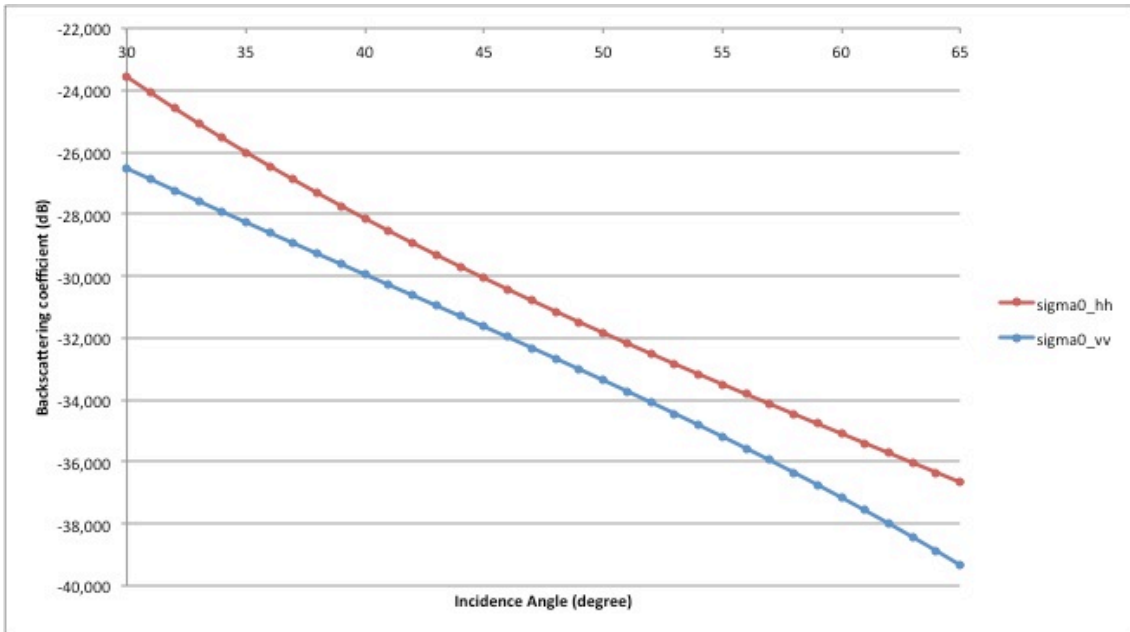


Fig. 3.54: Sensitivity evaluation for  $h=0.01$  and  $\epsilon=2$ .

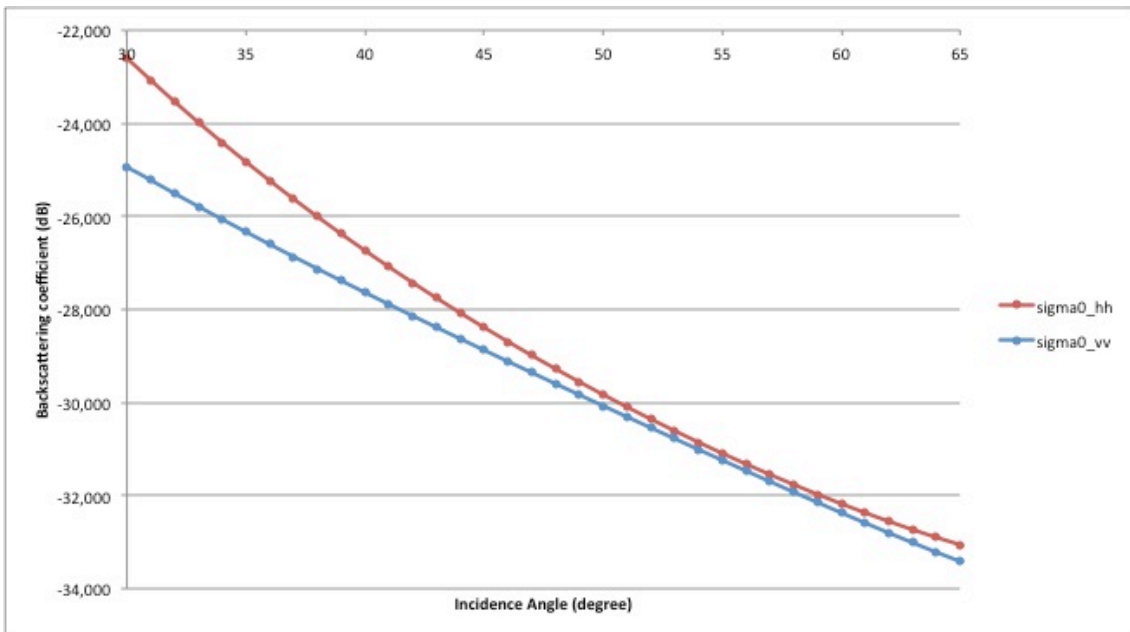


Fig. 3.55: Sensitivity evaluation for  $h=0.01$  and  $\epsilon=8$ .

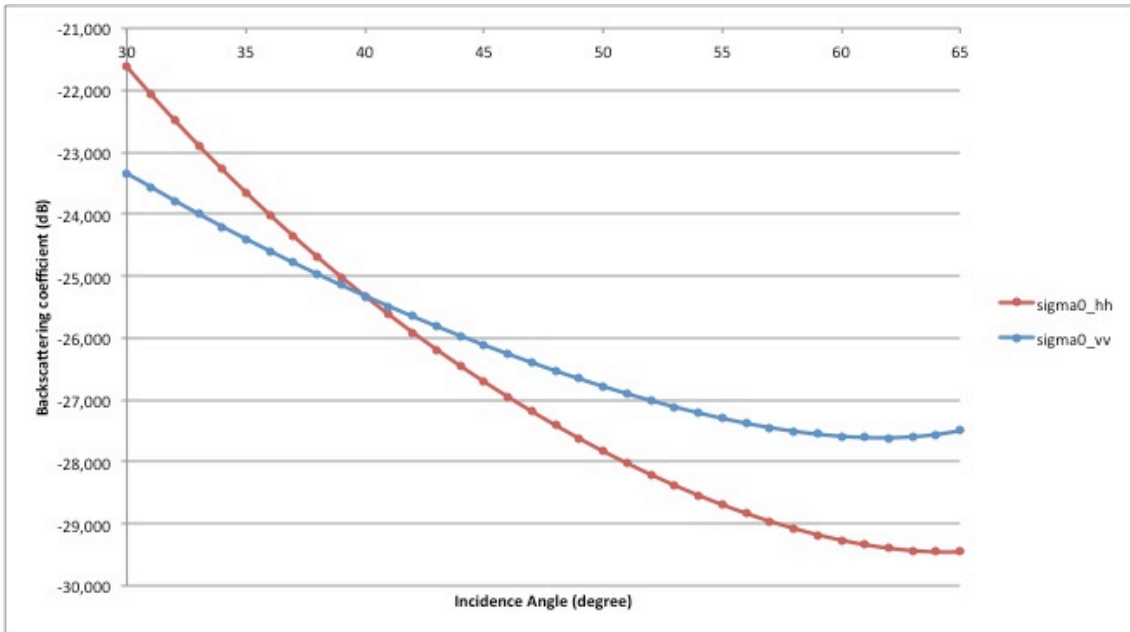


Fig. 3.56: Sensitivity evaluation for  $h=0.01$  and  $\epsilon=14$ .

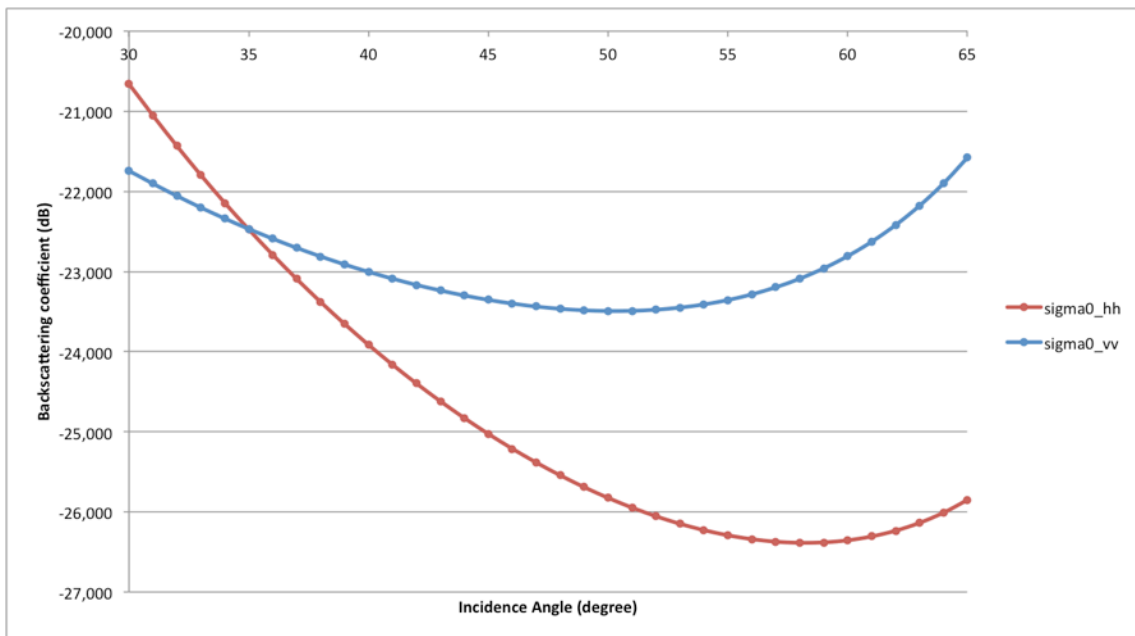


Fig. 3.57: Sensitivity evaluation for  $h=0.01$  and  $\epsilon=20$ .

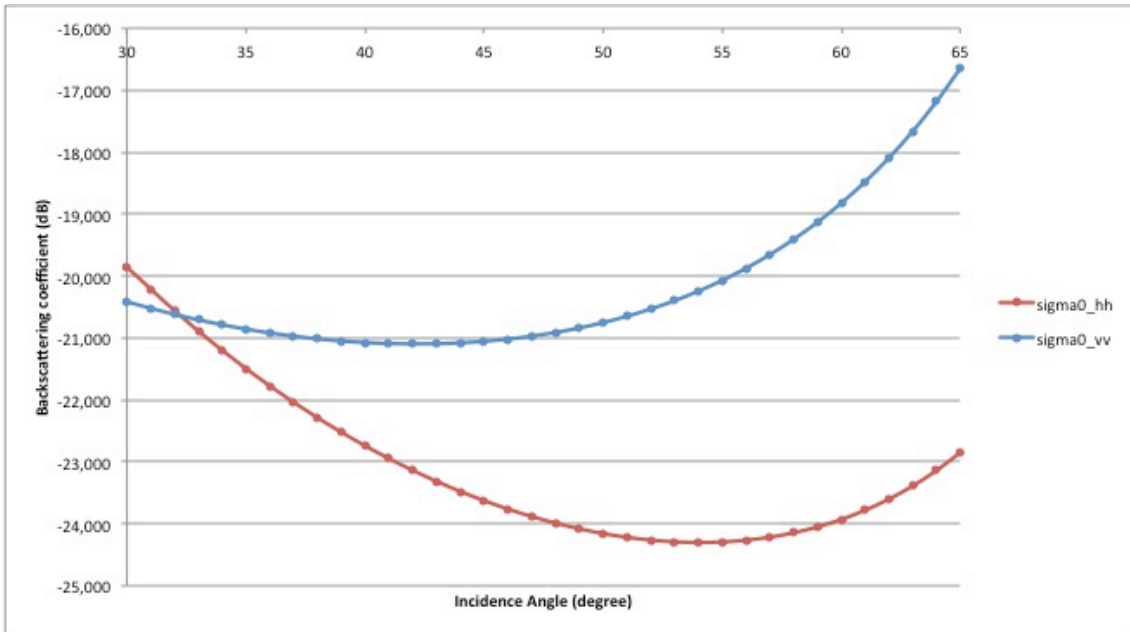


Fig. 3. 58: Sensitivity evaluation for  $h=0.01$  and  $\epsilon=25$ .

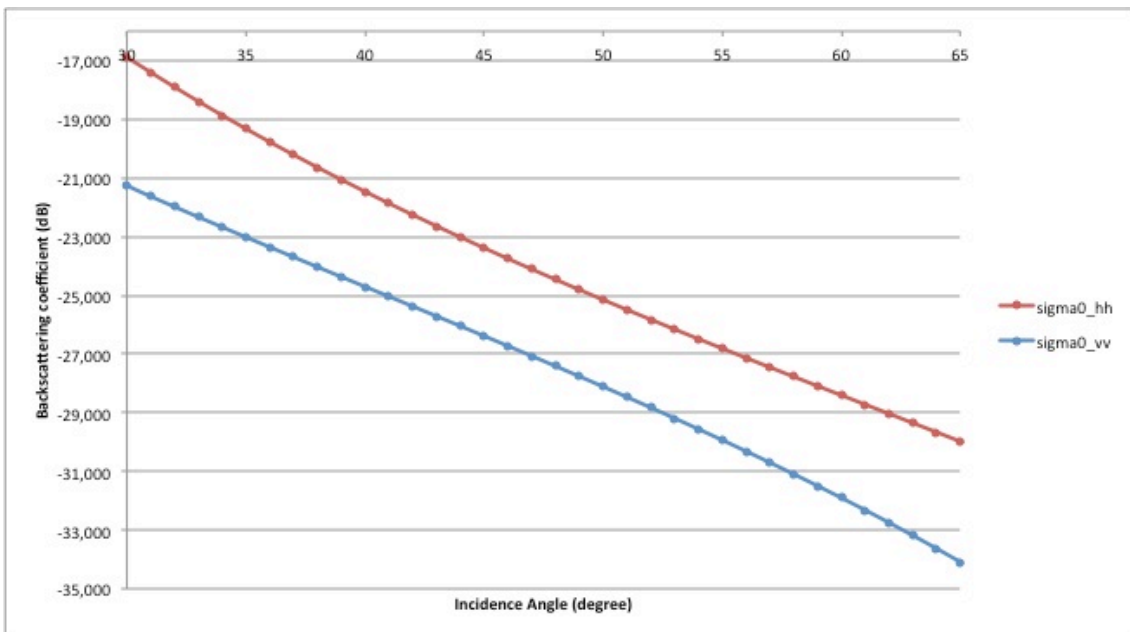


Fig. 3. 59: Sensitivity evaluation for  $h=0.03$  and  $\epsilon=2$ .

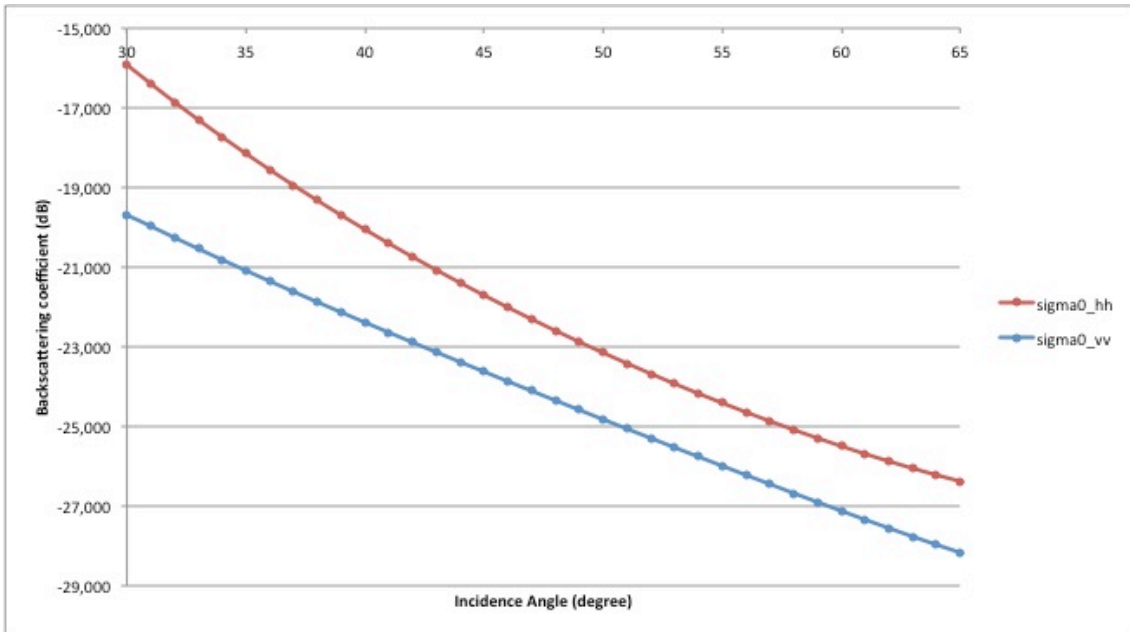


Fig. 3. 60: Sensitivity evaluation for  $h=0.03$  and  $\epsilon=8$ .

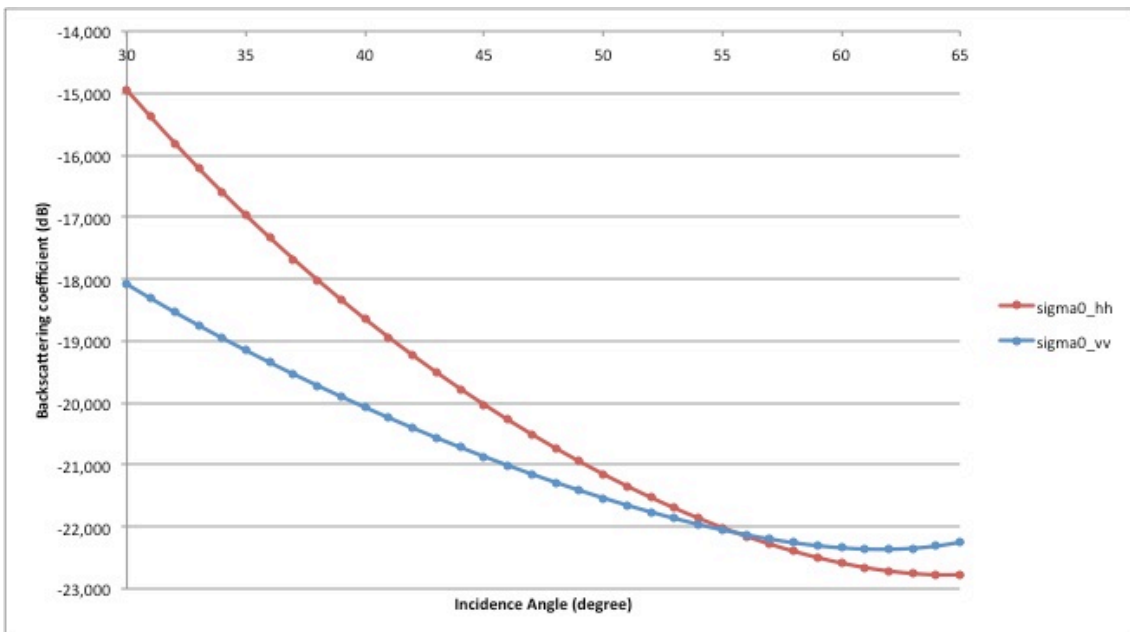


Fig. 3. 61: Sensitivity evaluation for  $h=0.03$  and  $\epsilon=14$ .

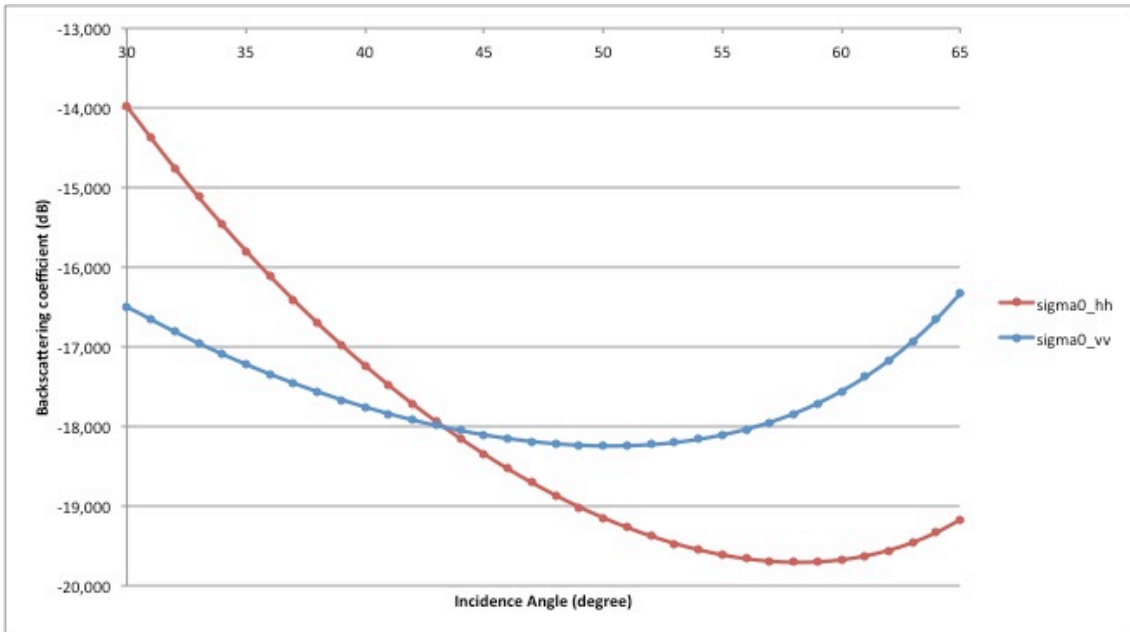


Fig. 3. 62: Sensitivity evaluation for  $h=0.03$  and  $\epsilon=20$ .

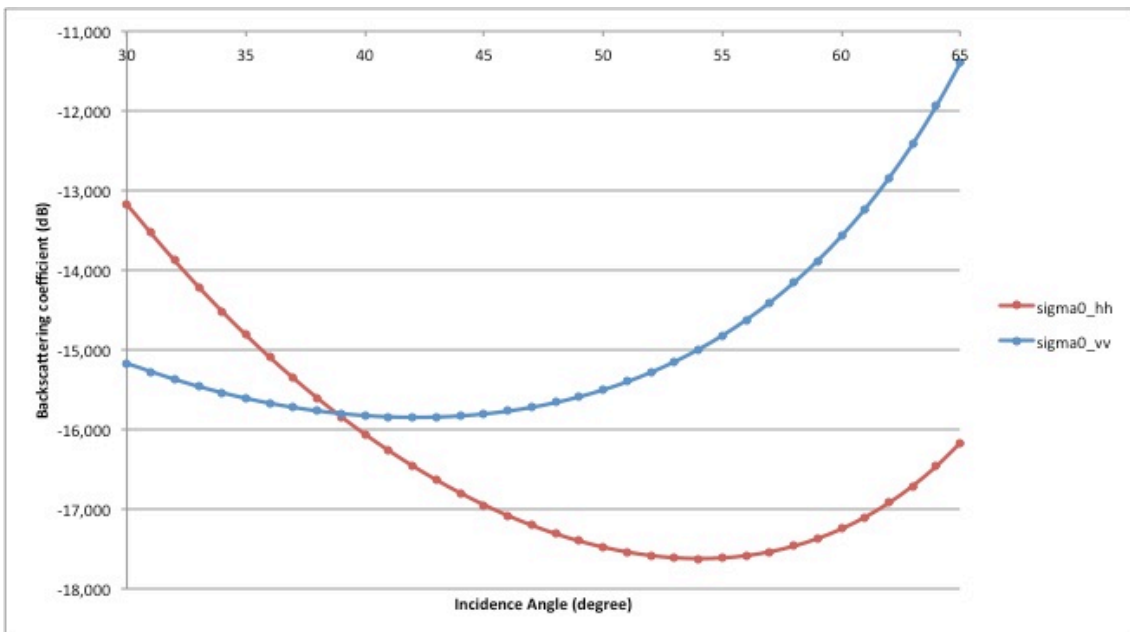


Fig. 3. 63: Sensitivity evaluation for  $h=0.03$  and  $\epsilon=25$ .

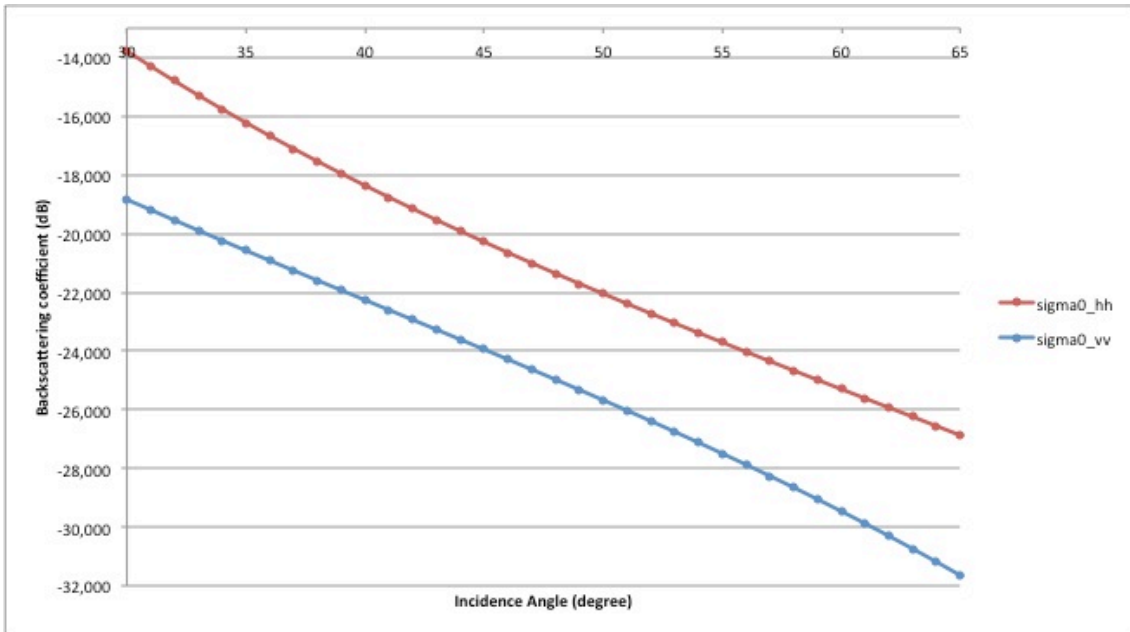


Fig. 3.64: Sensitivity evaluation for  $h=0.05$  and  $\epsilon=2$ .

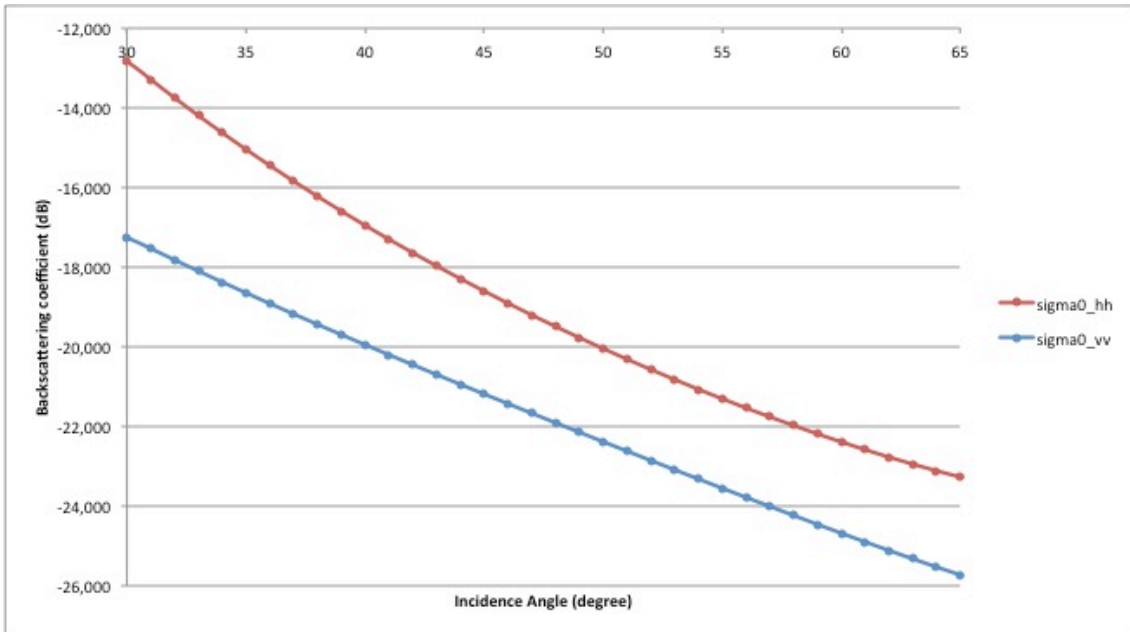


Fig. 3.65: Sensitivity evaluation for  $h=0.05$  and  $\epsilon=8$ .

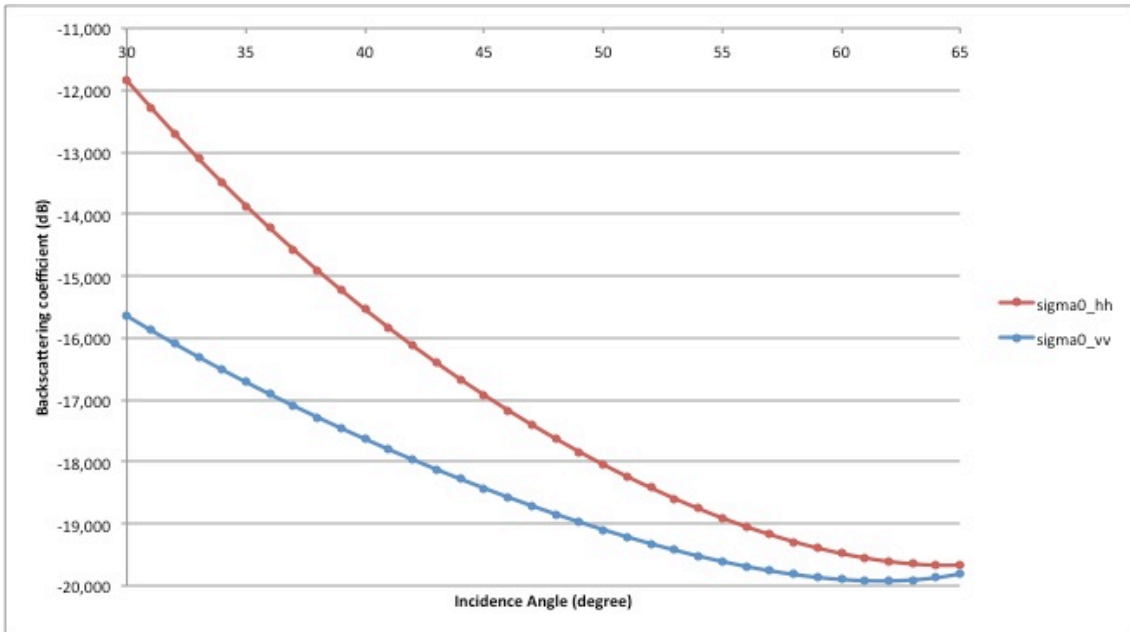


Fig. 3.66: Sensitivity evaluation for  $h=0.05$  and  $\epsilon=14$ .

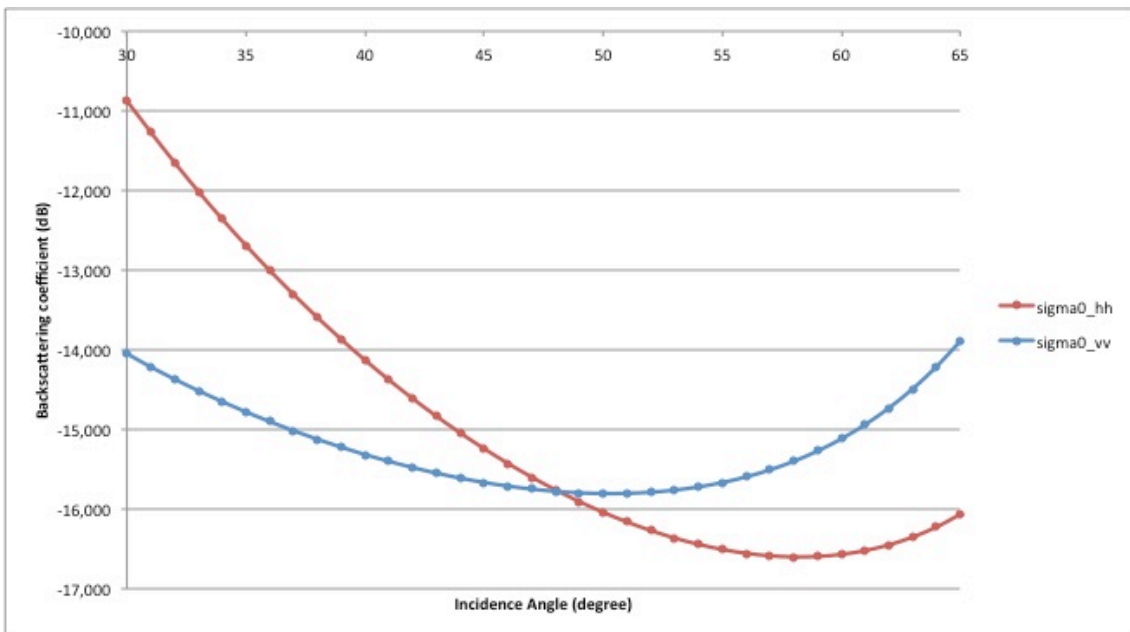


Fig. 3.67: Sensitivity evaluation for  $h=0.05$  and  $\epsilon=20$ .

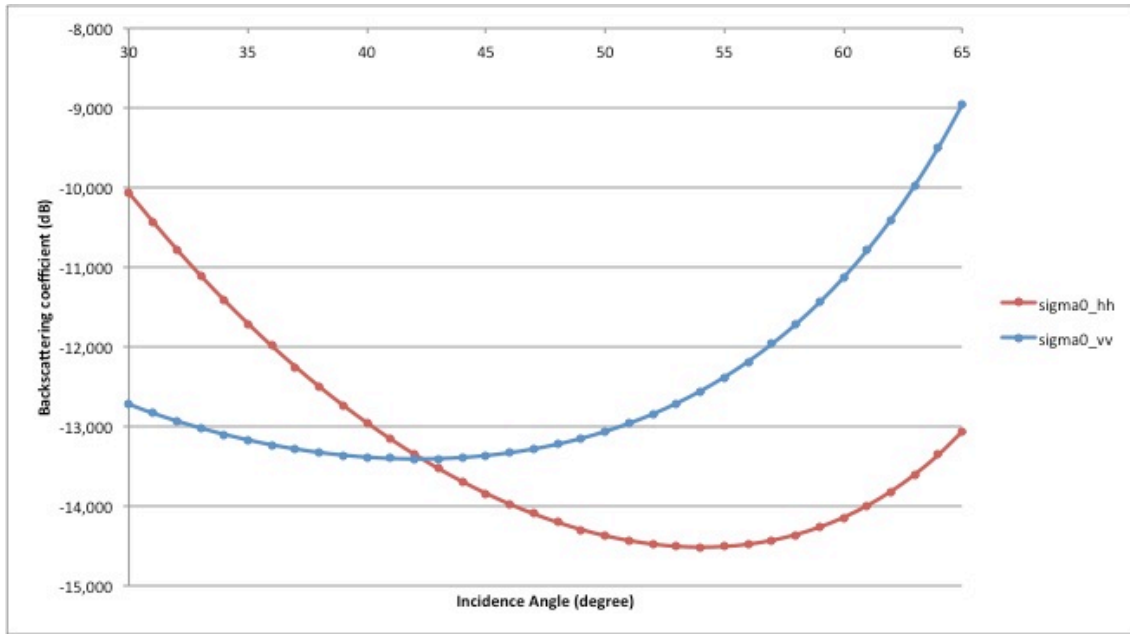


Fig. 3. 68: Sensitivity evaluation for  $h=0.05$  and  $\epsilon=25$ .

From these plots it is possible to identify some operative ranges of model functionality with the sensitivity of COSMO-SkyMed data. These ranges are shown in the following Tab. 3. 5.

<b>Rms Surface Height h [m]</b>	<b>Dielectric constant <math>\epsilon</math></b>	<b>Backsc. Coefficients <math>\sigma^0</math> [dB]</b>	<b>Incidence Angle <math>\theta</math> [degrees]</b>
0.03	8	Within -20dB	30 ÷ 33
0.03	14	Within -20dB	30 ÷ 40
0.03	20	Within -20dB	30 ÷ 65
0.03	25	Within -18dB	30 ÷ 65
0.05	2	Within -20dB	30 ÷ 33
0.05	8	Within -20dB	30 ÷ 41
0.05	14	Within -20dB	30 ÷ 65
		Within -15dB	30 ÷ 33
0.05	20	Within -20dB	30 ÷ 65
		Within -15dB	30 ÷ 38
0.05	25	Within -15dB	30 ÷ 65

Tab. 3. 5: Limit ranges of validity for the Dubois model by using COSMO-SkyMed data.

From these results it is possible to deduce that the Dubois model is applicable only for highest values of rms surface height and for high dielectric constant (hence for wet soil).

## **CHAPTER 4**

### ***Further Developments***

This research is aimed to the identification of new applications for the new generation of the Italian SAR system COSMO-SkyMed Seconda Generazione.

The launch of this system is planned for the 2015, when two satellites will reach the four one already present in orbit, and will join the first two satellites (SAR1 and SAR2) that, after 7 years of work have reached the end of their operability phase, assuring the service continuity.

In the following sections the COSMO-SkyMed Seconda Generazione system is shown in their polarimetric characteristics (which are interesting for this kind of application), and a possible further development in the frame of landslides monitoring and forecasting is going to be proposed.

#### ***4.1 Slope stability model***

Landslide events often occur in mountainous region, causing a large amount of losses in term of human lives and physical properties.

In the last years several researches have been conducted on the area of landslides hazard and assessment risk in different part of the world. Some of these studies consider the remotely sensed data as common approach for the evaluation of a safety factor for landslide hazard (Anbalagan R. and Singh B., 1996), for GIS based model (Thapa P.B. and Dhital M.R., 2000; Saha A.K. et al., 2002; Sarkar S. and Kanungo D.P., 2004), for statistical based model (Skirikar S.M. et al., 1998; Dhakal A.S. et al., 1999), and for deterministic based techniques (Joshi J. et al., 2000).

All quite the slope failure types require the soil moisture parameter knowledge. This parameter is pivotal because a great presence of water in soil increases the soil stress and reduces the soil strength (Ray R.L., 2004). The assessment of a regional or global soil moisture profiles is a difficult task to achieve. To overcome this problem the measurement of soil moisture by means of Synthetic Aperture Radar data was very useful, even if the microwave radiation can penetrate only a thin upper layer (Njoku E.G. et al., 2003) of the soil surface (typical value are between 1 and 5 centimetre, for landslide studies is critical to obtain soil moisture profile of the whole soil layer). We refer to the study of Jackson T.J. (1980), Arya L.M. et al. (1983) and Liang X. et al. (1994) to a detailed discussion on the link between the surface and sub-surface soil moisture.

A study on stability of slope is usually conducted for assessing the slope stability with controlled or uncontrolled ground water or pore water pressure. In this condition the slopes saturated by water,

should be subjected to seepage-induced by body forces, and thus to potentially de-establishing effects (Windisch E.J., 1991).

In the land application planning it is pivotal to take into account the risks derived by the instability of slopes, that could transform into landslides.

A slope stability model that takes into account the soil moisture parameter derived from remotely sensing data was deduced by Ray R.L. and Jacobs J. (2008). They evaluated a safety factor  $F$  for landslides hazards as follows:

$$F = \frac{C_s + C_r}{\gamma_e D \sin \theta} + \left(1 - m_v \frac{\gamma_w}{\gamma_e}\right) \frac{\tan \phi}{\tan \theta} \quad (4.1)$$

In this equation  $C_s$  and  $C_r$  are the effective soil and root cohesion [ $\text{kN}/\text{m}^2$ ],  $D$  is the depth of the soil above the failure plan [m],  $\theta$  is the slope angle [ $^\circ$ ],  $\phi$  is the internal friction angle,  $\gamma_w$  is the unit weight of water [ $\text{kN}/\text{m}^3$ ],  $\gamma_e$  is the effective weight of the soil, and  $m_v$  is the soil moisture content.

The  $\gamma_e$  weight can be defined as:

$$\gamma_e = q \frac{\cos \theta}{D} + (1 - m_v) \gamma_d + m_v \gamma_s \quad (4.2)$$

where  $\gamma_d$  is the unit weight of the dry soil [ $\text{kN}/\text{m}^3$ ] and  $\gamma_s$  is the unit weight of the saturated soil [ $\text{kN}/\text{m}^3$ ], and  $q$  is any additional load on the soil surface [ $\text{kN}/\text{m}^2$ ].

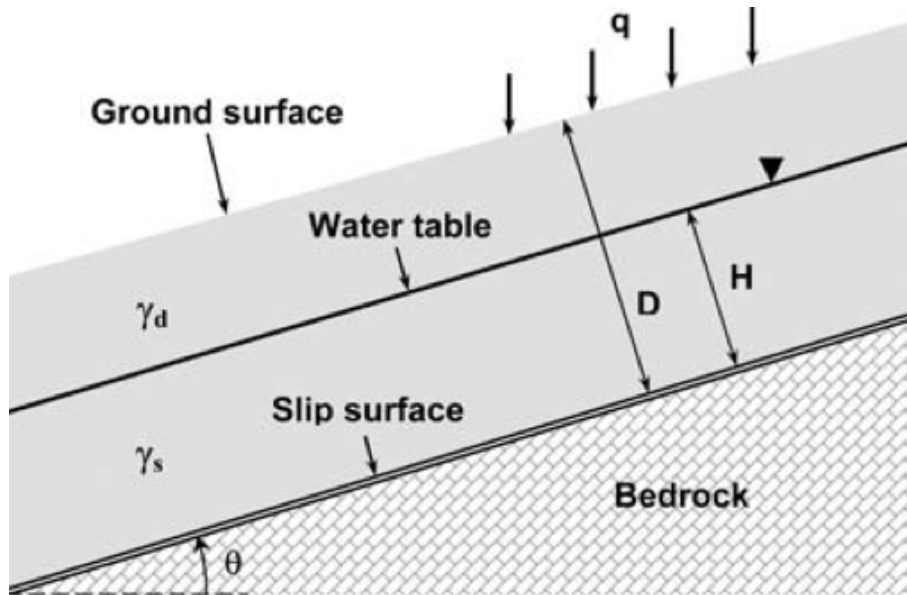


Fig. 4. 1: Representation of the different slope parameters and variables.  $H$  is the saturated thickness of the soil above the failure plain (m).

Ray R.L. and Jacobs J. (2008) investigate the generation of a slope stability safety factor methodology based on a physical slope stability modelling, taking into account the influence of rainstorm events and some variable parameters as soil type and topography, with the aims to produce a landslide susceptibility maps over a determined area.

They have applied this slope stability model to an area located in the Highway 50 corridor at Cleveland Corral, El Dorado County, CA, US; these regions are highly susceptible to landslides events subsequently to heavy rainfall.

For their work they have been used the Advanced Microwave Scanning Radiometer (AMSR-E) soil moisture data (obtained from NASA Earth Observing System Data Gateway), and the Tropical Rainfall Measuring Mission (TRMM) rainfall 3B42 3-hr product from Goddard Distributed Active Archive Center (DAAC). Other climatic data (for example rainfall data, temperature, wind speed, etc.) were obtained by National Climatic Data Center (NCDC) or through in situ measurements.

The soil and vegetation characteristics were obtained from the States Soil Geographic (STATSGO), Land Data Assimilation System (LDAS), and from literature (Ray R.L., 2004; Sidle R.C. and Ochiai H., 2006; Deoja B.B. et al., 1991).

The triggering mechanism for slope instability is usually a rise in the water content on ground, which increases soil saturation and ultimately the pore water pressure. As a consequence of this mechanism the normal effective stresses and shear strength are reduced for potential failure surfaces. To be able to understand properly the soil saturation index estimation and the models developed for this purpose, we suggest seeing Montgomery D.R. and Dietrich W.E. (1994), Borga M. et al. (1998), and Pack R.T. et al. (1998).

Slope stability maps can be derived from the topography, land-use, soil types, and rainfall characteristics.

The results of this study have permitted to estimate a safety factor,  $F$ , in four categories that establish the occurring of a landslide:

- Highly susceptible,  $F < 1$ ;
- Moderately susceptible,  $1 < F < 1.25$ ;
- Slightly susceptible,  $1.25 < F < 1.5$ ;
- Not susceptible,  $F > 1.5$ .

Whether a slope is unstable or stable depends on the value of factor  $F$  being larger or smaller than one (landslides occur when the safety factor is less than one). The stability is predominantly depending upon the value of the soil cohesion and friction angle. The most favourable condition towards stability scenario involves a completely dry soil ( $m=0$ ), and the worst condition is represented by a completely saturated soil ( $m=1$ ).

In the regions under study, the landslides happen in the periods when the occurring of rainfall is greater, and the soil moisture value is usually higher.

These results indicate an evident relationship between landslide events, surface soil moisture and rainfalls.

As an example of this result, we report the chart of Ray R.L. and Jacobs J. (2008) for the El Dorado County site (Fig. 4. 2) that indicates the safety factor values obtained by the application of the slope stability model.

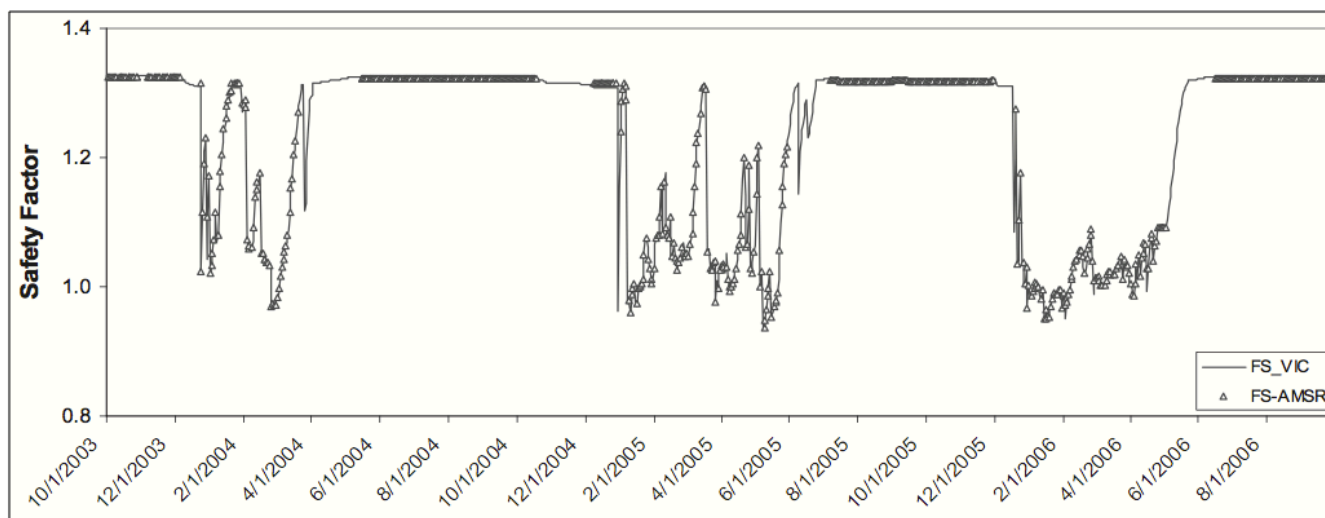


Fig. 4. 2: Dynamic safety factor values evaluated by Ray R.L. and Jacobs J. (2008) with the AMSR-E soil moisture data (2003-2006) for the California site.

These results on the Highway 50 corridor have shown a strong relationship between AMSR-E soil moisture data, modelled soil moisture and in situ pore water measurement, and were confirmed by the comparison with the real landslides inventory data.

Subsequently, a study of Ray R.L. and De Smedt F. (2009) on the Dhading district, Nepal has confirmed the results previously obtained on the slope stability factor model.

The results of these works suggest that rainstorms could generate gravitational slope when pore water pressures build up at the contact between the soil mantle and the underlying bedrock.

Soils that are unstable under fully saturated conditions are situated on steep slope angles with mostly agricultural land cover, or are excavated slopes along the highway. This indicates that these soils, due to their low cohesion and human disturbance become sensitive to failure with gradual increase of saturation.

In general these results show that agricultural lands is particularly susceptible to slope failure. This is because cultivation usually starts after strong deforestation without constructing appropriate terraces even on steep slopes.

#### ***4.2 COSMO-SkyMed Seconda Generazione***

The Italian Space Agency (ASI) and the Italian Ministry of Defence (ItMoD) have funded this Earth Observation program, formed by two satellites with a Synthetic Aperture Radar payload.

This program has been conceived as an evolution of the COSMO-SkyMed first generation system (CSK), and will assure the service continuity with respect to the actual four-satellites system.

These new satellites will implement a Dual-pol mode for the main acquisition modalities, transmitting vertical, V (or horizontal, H), and receiving simultaneously both the H and V components of a backscattered signal.

In addition to the capabilities of the first generation of COSMO-SkyMed, the Seconda Generazione (CSG) will have a full Quad-pol mode when the transmission rate is doubled: the H and V polarizations are alternatively used to transmit a signal, and the two polarization channels are simultaneously received. In this way the complete scattering matrix (HH, HV, VV and VH) can be acquired in the same area keeping the phase coherence information. It is possible to acquire a multi polarization image also with the PING-PONG mode (i.e. “alternating” or “burst polarimetric mode”), but losing the phase coherence among the polarization channels.

Caltagirone F. et al. (2012) has been presented, in his work, the detailed CSG polarimetric features.

This SAR system has been designed to operate in all the four polarization combinations (see Fig. 4. 3):

- ✓ Single polarization: HH or VV;
- ✓ Alternating polarization: HH and VV, or VV and VH, or HH and HV;
- ✓ Dual-pol: HH and HV, or VV and VH;
- ✓ Quad-pol: HH, VV, HV and VH.

The new entry mode is Quad-pol mode based on the standard STRIPMAP acquisition technique, and allowed two receiving channels at the same time.

In the STRIPMAP acquisition mode the rate, at which pulses are transmitted, is determined by the maximum Doppler bandwidth expected. This value is linked both to the azimuth beamwidth (i.e.  $\theta_{az} = 0.866\lambda / L$ , where  $L$  is the antenna length in the azimuth direction, and  $\lambda$  is the wavelength) and the SAR velocity (i.e.  $V \cong 7500m/s$ ), and in case of small azimuth beamwidths is expressed in the following form:

$$B_{dopp} = 4 \frac{V}{\lambda} \sin\left(\frac{\theta_{az}}{2}\right) \cong 2 \frac{V}{L} \quad (4.1)$$

In order to permit the acquisition of the full polarimetric scattering matrix (Quad-pol mode), the two polarizations are pulsed alternatively and the transmission rate is doubled, and hence the four polarimetric channels are acquired into the same area keeping the coherence in phase.

The polarimetric information can be achieved also with the PING-PONG acquisition mode, but in this case no phase coherence among the channels is available.

The Pulse Repetition Frequency (PRF) for the STRIPMAP mode is set to typical value of 3÷3.5 kHz, while for the QUAD-POL mode is set to 6÷7 kHz.

Caltagirone F. et al. (2012) have listed an evaluation of the performances for this acquisition mode, which is reported in the following table.

<b>Requirement</b>	<b>Unit</b>	<b>Value</b>
Access region	deg	20 ... 45
Swath		
Range	km	15 ... 20
Azimuth	km	40
Resolution		
Range	m	3
Azimuth	m	3

Tab. 4. 1: QUADPOL expected image quality performances (Caltagirone F., et al. 2012).

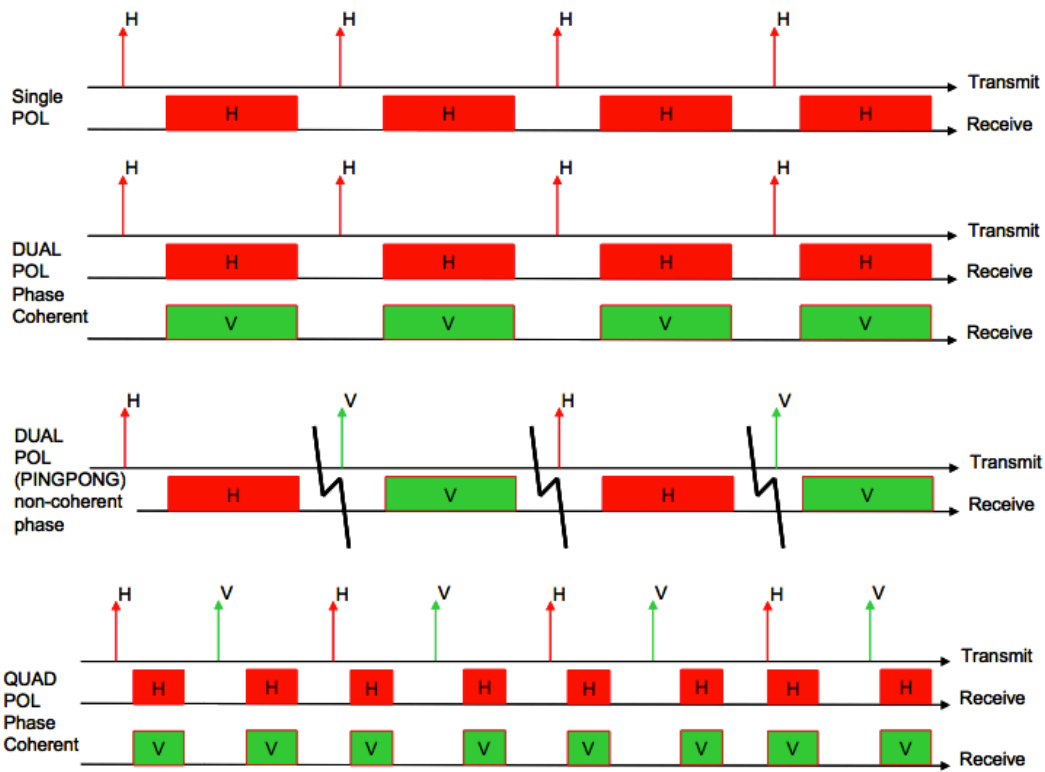


Fig. 4. 3: nominal STRIPMAP, DUAL-POL, PING-PONG, QUAD-POL modes (Caltagirone F., et al. 2012).

## ***CONCLUSIONS***

Several studies have demonstrated that landslide events occupy a large portion about the natural disaster field. For this kind of applications the most important parameter is the soil moisture content because a great presence of water into the soil increases the soil stress and reduces the soil strength.

These considerations, together with a deep study on the actually SAR system and on the state-of-the-art of the current SAR application, have led to focus this PhD research on the soil moisture measurement by using polarimetric SAR data.

This research was funded by the Italian Space Agency in order to suggest a new possible application for the COSMO-SkyMed Seconda Generazione satellites system.

Whit this purpose some polarimetric data (co-polarised, i.e. acquired on HH and VV polarization channels), of the first COSMO-SkyMed SAR system generation, have been made available by the Italian Space Agency freely.

These data, together with a TerraSAR-X polarimetric image (also co-polarised and provided by courtesy of Astrium-GEO), are used for soil moisture map retrieval.

During this research this data have been processed and analysed following a procedure described in Chapter 3.

A preliminary analysis on these data has shown the relationship existing between the radar backscattering and dielectric and geometric properties of the soil surface. This relationship was verified through two charts depicting the mean and standard deviation trend and the weather trend. These plots show a similar trend, which allows us to say, with reasonably certainty that this link actually exists. So, it is confirmed that SAR system is a valuable tool for a wide range of Earth Observation related to land and environmental applications.

Moreover, in order to well characterise the available SAR data and the SAR systems, an analysis on the complex polarimetric coherence were performed. The results of this study (reported in section 3.2.3) confirmed the poor value of coherence for the COSMO-SkyMed data that are acquired on a burst mode (with mean values around 0.2), while for the TerraSAR-X, that is fully polarimetric, show higher values which fall in the expected ranges (mean values around 0.6).

Subsequently an extensive study on the most known soil moisture retrieval models was conducted. This analysis has led to the choice of the Dubois model for the soil moisture retrieval on the co-polarised data.

The model was implemented considering the critical issues concerning the incidence angle variations during the acquisition, and the limitations introduced for the model itself. The resulting algorithm was then applied on the available data, obtaining soil moisture maps reported in section 3.3.

As we can see, the best results have been obtained on the more recent images of COMSO-SkyMed system, and on the TerraSAR-X image, together acquired on the Indonesian region of Pangkalanbuun, Central Kalimantan. The results obtained show a high percentage of soil moisture content above the soil, but unfortunately there are not soil moisture ground data for this area to confirm these results. So, the weather conditions involving the area at acquisition time are controlled, and are compared to the soil moisture map results.

The area was acquired on March 13, 2008 by the TerraSAR-X system, and then on December 1, 2013 by the COSMO-SkyMed system.

The oldest image was acquired during a period of heavy storms, when precipitations of about 24mm involving the area for consecutive days; while the youngest image was acquired during a clear weather period, but with an high percentage of atmospheric humidity, with values around the 80%.

Recalling that the microwave radiation can penetrate only few centimetres inside the first layer of soil is clear that the high values of soil moisture visible in the maps (lighter areas) are well related to the moisture condition involving the area during the acquisition.

As shown in section 2.3.1, the Dubois model imposes some limits to its applicability that involves the radiometric accuracy and the sensitivity of the SAR system. The radiometric accuracy required by the model is equal to 2dB, and is the same specified for the COSMO-SkyMed SAR system.

Collaboration with Thales Alenia Space Rome (TAS Rome) has been established in order to analyse the model sensitivity with the COSMO-SkyMed polarimetric data.

This sensitivity analysis has shown that the model's equations for the backscattering coefficients measurement provide values near the sensitivity inferior limit of the SAR system (between -19dB and -15dB). Moreover it has been identified the limit ranges of validity for the use of the Dubois model with the COSMO-SkyMed data, that are reported in Tab. 3. 5.

These results led us to affirm that a phase correlation preservation of the COSMO-SkyMed SAR satellites data could bring out the new generation of the ASI system as leader among the Earth Observation missions, and in particular in the landslides monitoring and forecasting field.

In fact, as we have shown in the Chapter 4, COSMO-SkyMed Seconda Generazione involves some upgrades about the polarimetric characteristics of the system, keeping the service continuity.

These upgrades concern the capability to simultaneously acquire coherent data in all the four polarization channels (i.e. QUAD-POL mode: HH, HV, VV, and VH polarization).

Certainly an improvement over the sensitivity of the sensor would be useful for the application of this model on the COSMO-SkyMed data, which actually is close to the inferior limit; some progresses can be achieved by improving the response of the electronic component of the system (for example, reducing noise, improving the gain, increasing the efficiency, using noble metals to stabilize the signal, etc.).

Recalling the aim of this research, that is the suggestion of new applications for the COSMO-SkyMed Seconda Generazione system, we have presented a possible further development in the section 4.1.

Once obtained these improvements on the data, it is possible to think of a landslide monitoring and forecasting project based on the Ray R.L. and Jacobs J. (2008) work.

A slope stability model has been proposed which allows to classify an area into four classes of risk (safety factors  $F$ ) concerning the occurrence of a landslide.

These safety factors are evaluated by means of the soil moisture parameter, which plays a critical role in triggering landslides.

The value of soil moisture parameter can be achieved at global scale by using remotely sensed data; in particular the data acquisition by means SAR satellite systems (that use microwave radiation for the transmits signal) are useful in this frame thanks to their capability to acquire independently on weather conditions and on daylight conditions. Moreover they can reach each point on the ground surface, also that they are inaccessible to ground measurements.

The slope instability is a major concern in almost all parts of the Earth, and the possibility to evaluate a slope stability map may be of great help to regions too often involved in natural landslide disasters in specific areas.

The ability to capture the evolution of soil moisture, and the capability to create a detailed stability map over wide areas, may be will allow us to anticipate critical hazard periods on a specific area, real time basis, and giving the opportunity to prevent the loss of human lives and material issues.

## REFERENCES

1. **Abramson L.W.**, Lee T.S., Shama S., Boyce G.M., “Slope stability and stabilization methods”, *A Wiley-Interscience Publication, John Wiley & Sons, Inc.*, New York, **1996**.
2. **Allain S.**, Ferro-Famil L., Pottier E., “Surface parameters retrieval from polarimetric and multi-frequency SAR data”, *Proceedings of IGARSS '03: Learning from Earth's Shapes and Sizes*, pp.1417-1419, **2003**.
3. **Alvarez-Mozos J.**, Gonzalez-Audicana M., Casali J., Larranaga A., “Effective versus measured correlation length for radar-based surface soil moisture retrieval”, *International Journal of Remote Sensing*, vol.29, no.17-18, pp.5397-5408, **2008**.
4. **Anbalagan R., Singh B.**, “Landslide hazard and risk assessment mapping of mountainous terrains: a case study from Kumaun Himalaya, India”, *Eng. Geol.*, 43(4):237-246, **1996**.
5. **Arya L.M.**, Richter J.C., Paris J.F., “Estimating profile water storage from surface zone soil moisture measurements under bare field conditions”, *Water resources Research*, vol.19, no.2, pp.403-412, **1983**.
6. **Attema E., Ulaby F.**, “Vegetation modelled as a water cloud”, *Radio Science*, vol.13, pp.357-364, **1978**.
7. **Baghdadi N.**, Aubert M., Cerdan O., Franchisteguy L., Viel C., Martin E. Zribi M., Desprats J.F., “Operational mapping of soil moisture using synthetic aperture radar data: Application to the touch basin (France)”, *Sensors*, vol.7, no.10, pp.2458-2483, **2007**.
8. **Bindlish R., Barros A.P.**, “Parameterization of vegetation backscatter in radar-based soil moisture estimation”, *Remote Sensing of Environment*, vol.76, pp.130-137, **2001**.
9. **Bond J.J., Willis W.O.**, “Soil-water evaporation – long-term drying as influenced by surface residue and evaporation potential”, *Soil Science Society of America Proceedings*, vol.35, no.6, p.984, **1971**.
10. **Borga M.**, Dalla Fontana G. Da Ros D., Marchi L., “Shallow landslide hazard assessment using physically based model and digital elevation data”, *Environ. Geol.*, 35(2-3):81-88, **1998**.
11. **Borgeaud, M.**, Noll, J. Bellini A., “Multi-temporal comparisons of ERS-1 and JERS-1 SAR data for land applications”, *Geoscience and Remote Sensing Symposium, IGARSS '94. Surface and Atmospheric Remote Sensing: Technologies, Data Analysis and Interpretation*, vol.3, pp.1603-1605, 8-12 Aug **1994**.

12. **Born M., Wolf E.**, “Principle of Optics: electromagnetic theory of propagation interference and diffraction of light”, 5<sup>th</sup> ed. Elmsford, NY: Pergamon, **1985**.
13. **Brown W.M.**, “Synthetic aperture radar”, *IEEE Transactions on Aerospace and Electronic Systems*, vol.AES-3, no.2, pp.217-229, **1967**.
14. **Bryant R.**, Moran M.S., Thoma D.P., Collins C.D.H., Skirvin S., Rahman M., Slocum K., Starks P., Bosch D., Dugo M.P.G., “ Measuring surface roughness height to parameterize radar backscatter models for retrieval of surface soil moisture”, *IEEE Geoscience and Remote Sensing Letters*, vol.4, no.1, pp.137-141, **2007**.
15. **Bulfin M., Gleeson T.**, “A study of surface soil conditions under a non-cultivation management system. I. Physical and chemical properties”, *Irish Journal of Agricultural Research*, vol.6, no.2, pp.177, **1967**.
16. **Caltagirone F.**, De Luca G.F., Covello F., Fiorentino C., Serva S., Di Domizio D., Cecchini A., Torre A., “The new Quad-pol characteristics of COSMO-SkyMed Seconda Generazione”, *Joint KA-ICSSC Conference*, Ottawa, Canada, September 24-27, **2012**.
17. **Chen K., Fung A.K.**, “A comparison of Backscattering Models for Rough Surfaces”, *IEEE Transactions on Geoscience and Remote Sensing*, vol.33, no.1, pp.195-200, **1995**.
18. **Cloude S.R.**, “Eigenvalue parameters for surface roughness studies”, *Polarization: measurement, analysis and remote sensing II*, D.H. Goldstein and D.B. Chenault, Eds., pp.2-13, **1999**.
19. **Curlander J.C., McDonough R.N.**, “Synthetic aperture radar: systems and signal processing”, J.A. Kong, Ed., John Wiley & Sons, New York, p.648, **1991**.
20. **Dalton F.N., Van Genuchten M.Th.**, “The time-domain reflectometry method for measuring soil water content and salinity”, *Geoderma*, vol.38,no.1-4, pp-237-250, **1986**.
21. **Davidson M.W.J., Le Toan T., Borgeaud M., Manninen T.**, “ Measuring the roughness characteristics of natural surfaces at pixel scales: moving from 1 metre to 25 metre profiles”, *Proceedings of IGARSS '98: Remote Sensing and Managing the Environment*, pp.1200-1202, **1998**.
22. **Davidson M.W.J., Le Toan T., Mattia F., Satalino G., Manninen T., Borgeaud M.**, “On the characterization of agricultural soil roughness for radar remote sensing studies”, *IEEE Transactions on Geoscience and Remote Sensing*, vol.38, no.2, pp.630-640, **2000**.
23. **De Loor G.P.**, “The dielectric properties of wet materials”, *IEEE Transactions on Geoscience and Remote Sensing*, vol.GE-21, no.3, pp.364-369, **1983**.

24. **Deoja B.B.**, Dhital M., Thapa B., Wagner A., “Mountain risk engineering handbook”, *International Centre for Integrated Mountain Development*, Kathmandu, Nepal, pp.875, **1991**.
25. **Dhakal A.S.**, Amada T., Aniya M., “Landslide mapping and the application of GIS in the Kulekhani watershed, Nepal”, *Mt. Res. Dev.*, 19(1):3-16, **1999**.
26. **Dobson M.C., Ulaby F.T.**, “Active microwave soil moisture research”, *IEEE Transactions on Geoscience and Remote Sensing*, vol.GE-24, no.1, pp.28-35, **1986**.
27. **Dubois P.C.**, van Zyl J., Engman T., “Measuring soil-moisture with imaging radars”, *IEEE Transactions Geoscience and Remote Sensing*, vol.33, no.4, pp.915-926, **1995**.
28. **Elachi C.**, “Spaceborne radar remote sensing: applications and techniques”, *IEE Press*, New York, p.252, **1987**.
29. **Emerson W.W.**, “Stability of soil crumbs”, *Nature*, vol.183, no.4660, p.538, **1959**.
30. **Ferrazzoli P.**, Paloscia S., Pampaloni P., Schiavon G., Solimini D., Coppo P., “Sensitivity to microwave measurements to vegetation biomass and soil moisture content: a case study”, *IEEE Transactions on Geoscience and Remote Sensing*, vol.30, no.4, pp.750-756, **1992**.
31. **Franceschetti G., Lanari R.**, “Synthetic Aperture Radar Processing”, CRC Press, Boca Raton (FL), **1999**.
32. **Franceschetti G.**, Migliaccio M., Riccio D., Schirinzi G., “SARAS: a Synthetic Aperture Radar (SAR) raw signal simulator”, *IEEE Transactions on Geoscience and Remote Sensing*, Vol. 30, No 1, January **1992**.
33. **Freeman A.**, “Sar calibration: an overview”, *IEEE Transactions on Geoscience and Remote Sensing*, vol.30, no.6, pp.1107-1121, **1992**.
34. **Frost V.S.**, Stiles J.A., Shanmugan K.S., Holtzman J.C., “A model for radar images and its application to adaptive digital filtering of multiplicative noise”, *IEEE Transactions on Pattern Analysis and Machine Intelligence*, vol.4, no.2, pp.157-166, **1982**.
35. **Fung A.K.**, Dawson M.S., Chen S., Hsu A.Y., Engman E.T., Oneill P.O., Wang J., “A modified IEM model for scattering from soil surfaces with application to soil moisture sensing”, *Proceedings of IGARSS '96: Remote Sensing for a Sustainable Future*, 27-31 May, Lincoln, USA, pp.1297-1299, **1996**.
36. **Fung A.K.**, Li Z., Chen K.S., “Backscattering from a randomly rough dielectric surface”, *IEEE Transactions Geoscience and Remote Sensing*, vol.30, pp.356-369, **1992**.
37. **Gardner W.H.**, “Water Content”, in *Methods of Soil Analysis Part 1: Physical and Mineralogical Methods*, 2<sup>nd</sup> ed. A. Klute, Ed. American Society of Agronomy, Soil Science

- Society of America, Madison, pp.493-544, **1986**.
38. **Goodman J.W.**, “some fundamental properties of speckle”, *J. Opt. Soc. Amer.*, vol.66, no.11, pp.1145-1150, **1976**.
  39. **Hajnsek I.**, Pottier E., Cloude S.R., “Inversion of surface parameters from polarimetric SAR”, *IEEE Transactions on Geoscience and Remote Sensing*, vol.41, no.4, pp.727-744, **2003**.
  40. **Hajnsek J.**, “Inversion of surface parameters (soil moisture & roughness) using polatimetric SAR”, Doctoral thesis, FSU, Jena, Germany, 17 October **2001**.
  41. **Hallikainen M.T.**, Ulaby F.T., Dobson M.C., Elrayes M.A., Wu L.K. “Microwave dielectric behaviour of wet soil, part I: empirical-models and experimental-observations”, *IEEE Transactions on Geoscience and Remote Sensing*, vol.23,no.1,pp.25-34, **1985**.
  42. **Henderson F.M., Lewis A.J.**, “Manual of Remote Sensing Vol.2: Principles and Applications of Imaging Radar”, 3<sup>rd</sup> ed., R.A. Ryerson, Ed. John Wiley & Sons, New York, **1998**.
  43. **Hoekstra P., Delaney A.**, “Dielectric Properties of Soils at UHF and Microwave Frequencies”, *Journal of Heophysical Research*, vol.79, no.11, pp.1699-1708, **1974**.
  44. **Iodice A., Natale A., Riccio D.**, “A polarimetric two-scale model for soil moisture retrieval”, *IEEE International Geoscience and Remote Sensing Symposium. IGARS 2010*, pp.1265-1268, **2010**.
  45. **Iodice A., Natale A., Riccio D.**, “Retrieval of Soil Surface Parameters via a Polarimetric Two-Scale Model Model in Hilly or Mountainous Areas”, in *Proceedings of SPIE 2011*, Prague, **2011-B**.
  46. **Iodice A., Natale A., Riccio D.**, “Retrieval of Soil Surface Parameters via a Polarimetric Two-Scale Model”, *IEEE Transactions on Geoscience and Remote Sensing*, vol. 49, no. 7, pp. 2531-2547, July **2011-A**.
  47. **Jackson T.J.**, “Profile soil moisture from surface measurements”, *Journal of the Irrigation and Drainage Division, American Society of Civil Engineers*, vol.106(IR2), pp.81-92, **1980**.
  48. **Jackson T.J., Schmugge T.J.**, “Vegetation effects on the microwave emission of soils”, *Remote Sensing of Environment*, vol.36, pp.203-212, **1991**.
  49. **Jacome A., Bernier M., Chokmani K., Gauthier Y., Poulin J., De Sève D.**, “Monitoring volumetric surface soil moisture content at the La Grande Basin Boreal Wetland by radar multi polarization data”, *Remote Sensing*, 5(10), 4919-4941, **2013**.
  50. **Jenny H.**, “Factors of soil formation”, originally published: 1941, McGraw-Hill, New York. With new foreword by R.Amundson, Dover Publications, p.271, New York, **1994**.

51. **Jester W., Klik A.**, “Soil surface roughness measurement – methods, applicability, and surface representation”, *Catena*, vol.64, no.2-3, pp.174-192, **2005**.
52. **Joshi J.**, Maitan S., Morita K., Omura H., “Landslide hazard mapping in the Nallu Khola watershed, Central Nepal”, *J. Nepal Geol. Soc.*, 21:21-28, **2000**.
53. **Koyama C. N.**, “Quantitative Estimation of Surface Soil Moisture in Agricultural Landscapes using Spaceborne Synthetic Aperture Radar Imaging at Different Frequencies and Polarizations”, Doctoral Thesis, Köln, Germany, **2012**.
54. **Lal R.**, “Soil structure and sustainability”, *Journal of Sustainable Agriculture*, vol.1, no.4, pp.67-92, **1991**.
55. **Lee J.S.**, “Speckle analysis and smoothing of synthetic aperture radar images”, *Computer Graphics and Image Processing*, vol.17, no.1, pp.24-32, **1981**.
56. **Lee J.S.**, Ainsworth T.L., Chen A.J., “Improved sigma filter for speckle filtering of SAR imagery”, *IEEE Transactions on Geoscience and Remote Sensing*, vol.47, no.1, pp.202-213, **2009**.
57. **Lee J.S.**, Grunes M.R., de Grandi G., “Polarimetric SAR speckle filtering and its implication for classification”, *IEEE Transactions on Geoscience and Remote Sensing*, vol.37, no.5, pp.2363-2373, **1999**.
58. **Lee J.S.**, Grunes M.R., Mango S.A., “Speckle reduction in multipolarization, multifrequency SAR imagery”, *IEEE Transactions on Geoscience and Remote Sensing*, vol.29, no.4, pp.535-544, **1991**.
59. **Lee J.S.**, Grunes M.R., Schuler D.L., Pottier E., Ferro-Famil L., “Scattering-model-based speckle filtering of polarimetric SAR data”, *IEEE Transactions on Geoscience and Remote Sensing*, vol.44, no.1, pp.176-187, **2006**.
60. **Lee J.S.**, Jurkevich L., Dewaele P., Wambacq P., Oosterlinck A., “Speckle filtering of synthetic aperture radar images: a review”, *Remote Sensing Reviews*, vol.8, no.4, pp.313-340, **1994**.
61. **Liang X.**, Lettenmaier D.P., E.F. Wood, Burges S.J., “A simple hydrologically based model of land surface water and energy fluxes for GSMs”, *J. Geophys. Res.*, vol.99, no.D7, pp.14,415-14,428, **1994**.
62. **Lopes A.**, Touzi R., Nezry E., “Adaptive speckle filters and scene heterogeneity”, *IEEE Transactions on Geoscience and Remote Sensing*, vol.28, no.6, pp.992-1000, **1990**.
63. **Low A.J.**, “the study of soil structure in the field and the laboratory”, *Journal of Soil Science*, vol.5, no.1, pp.57-79, **1954**.

64. **Mattei E.**, De Santis A., Di Matteo A., Pettinelli E., Vannaroni G., “Electromagnetic parameters of dielectric and magnetic mixtures evaluated by time-domain reflectometry”, *IEEE Transactions on Geoscience and Remote Sensing Letters*, vol.5, no.4, pp.730-734, **2008**.
65. **Montgomery D.R., Dietrich W.E.**, “A physically based model for the topographic control on shallow landsliding”, *Water Resour Res.*, 30(4):1153-1171, **1994**.
66. **Moreira A.**, Mittermayer J., Scheiber R., “Extended chirp scaling algorithm for air- and spaceborne SAR data processing in stripmap and ScanSAR imaging modes”, *IEEE Transactions on Geoscience and Remote Sensing*, vol.34, no.5, pp.1123-1136, **1996**.
67. **Mortland M. M.**, “Specific surface and its relationship to some physical and chemical properties of soil”, *Soil Science*, vol. 78, no. 5, pp. 343-347, **1954**.
68. **Natale A.**, “Electromagnetic Models for the Retrieval of Surface Parameters through SAR Images”, PhD thesis, University “Federico II” of Naples, a.a 2010/**2011**
69. **Nezry E.**, Lopes A., Touzi R., “Detection of structural and textural features for SAR images filtering”, *Proceedings of IGARSS '91: Remote Sensing – Global Monitoring for Earth Management*, pp.2169-2172, **1991**.
70. **Njoku E.G.**, Jackson T.J., Lakshmi V., Chan T.K., Nghiem S.V., “Soil moisture retrieval from AMSR-E”, *IEEE Transactions on Geoscience and Remote Sensing*, vol.412, no.2, pp.215-229, **2003**.
71. **Oh Y.**, “Retrieval of the effective soil moisture contents as a ground truth from natural soil surfaces”, *IEEE 2000 International Geoscience and Remote Sensing Symposium, Proceedings. IGARSS 2000*, vol.4, pp.1702-1704, **2000**.
72. **Oh Y., Hong J.Y.**, “Effect of surface profile length on the backscattering coefficients of bare surfaces”, *IEEE Transactions on Geoscience and Remote Sensing*, vol.45, no.3, pp.632-638, **2007**.
73. **Oh Y., Kay Y.C.**, “Condition for precise measurement of soil surface roughness”, *IEEE Transactions on Geoscience and Remote Sensing*, vol.36, no.2, pp.691-695, **1998**.
74. **Oh Y.**, Sarabandi K., Ulaby F.T., “An empirical model and an inversion technique for radar scattering from bare soil surfaces”, *IEEE Transactions Geoscience and Remote Sensing*, vol.30, no.2, pp.370-381, **1992**.
75. **Pack R.T.**, Tarboton D.G., Goodwin C.N., “ The SINMAP approach to terrain stability mapping”, *Moore DP, Hungr O (eds) Proceedings international congress of the international association for engineering geology and the environment 8(2)*, A.A. Balkema, Rotterdam,

- Netherlands, pp.1157-1165, **1998**.
76. **Peplinski N.R.**, Ulaby F.T., Dobson M.C., “Corrections to “Dielectric Properties of Soils in the 0.3-1.3 GHz Range””, *IEEE Transactions on Geoscience and Remote Sensing*, vol.33, no.6, p.1340, **1995**.
  77. **Ray R.L.**, “Slope stability analysis using GIS on a regional scale: a case study from Dhading, Nepal”, *MSc. Thesis, Vrije Universiteit Brussel, Belgium*, pp-98, **2004**.
  78. **Ray R.L., De Smedt F.**, “Slope stability analysis on a regional scale using GIS: a case study from Dhading, Nepal”, *Env. Geol.*, 57:1603-1611, doi: 10.1007/s00254-008-1435-5, **2009**.
  79. **Ray R.L., Jacobs J.M.**, “Landslide Susceptibility Mapping using remotely sensed soil moisture”, *IEEE International Geoscience and Remote Sensing Symposium, IGARSS 2008*, vol.III, pp.47-50, **2008**.
  80. **Rees G.**, “Physical Principles of Remote Sensing”, Cambridge University Press, Cambridge, **2001**.
  81. **Reigber A.**, “Airborne polarimetric SAR tomography”, University of Stuttgart, Germany, **2001**.
  82. **Ren W., Tateiba M.**, “Dielectric mixing formula for multiphase mixtures”, in *Proceedings of IGARSS '98: Remote Sensing and Managing the Environment*, pp.2089-2091, **1998**.
  83. **Saha A.K.**, Gupta R.P., Arora M.K., “GIS-based landslide hazard zonation in the Bhagirathi (Ganga) Valley, Himalayas”, *Int. J. Remote Sens.*, 23(2):357-369, **2002**.
  84. **Sarkar S., Kanungo D.P.**, “An integrated approach for landslide susceptibility mapping using remote sensing and GIS”, *Photogramm Eng. Remote Sens.*, 70(5):617-625, **2004**.
  85. **Satalino G.**, Pasquariello G., Mattia F., Davidson M., Le Toan T., Borgeaud M., “Soil moisture retrieval using SAR data and a priori roughness information”, *Proceedings of IGARSS '01: Scanning the Present, Resolving the Future*, pp.3111-3113, **2001**.
  86. **Scheffer F., Schachtschabel P.**, *Lehrbuch der Bodenkunde*, 15. Aufl. / Neubearb. Und erw. Von H.-P. Blume, Spectrum Akad. Verlag, Heidelberg, p. 593, **2002**.
  87. **Shaver T.M.**, Peterson G.A. Ahuja L.R., Westfall D.G., Sherrod L.A., Dunn G., “Surface soil physical properties after twelve years of dryland no-till management” *Soil Sci. Soc. Am. J.*, vol.66, no.4, pp.1296-1303, **2002**.
  88. **Shi J.**, Wang J., Hsu A.Y., O'Neill P.E., Engman E.T., “Estimation of bare surface soil moisture and surface roughness parameter using L-band SAR image data”, *IEEE Transactions Geoscience and Remote Sensing*, vol.35, no.5, pp.1254-1266, **1997**.

89. **Sidle R.C., Ochiai H.**, “Landslide: Processes, Prediction, and Land Use”, *American Geophysical Union, Water Resources Monograph*, pp.312, **2006**.
90. **Skirikar S.M.**, Rimal L.N., Jäger S., “Landslide hazard mapping of Phewa Lake catchment area, Pokhara, Central West Nepal”, *J. Nepal Geol. Soc.*, 18:335-345, **1998**.
91. **Skolnik M.I.**, “Introduction to radar systems”, 3rd ed., McGraw-Hill Book Company, Singapore, p.581, **1981**.
92. **Snell F. D.**, Snell C. T., Reich I., “The nature of soil to be deterged and its bonding to the surface”, *Journal of the American Oil Chemists Society*, vol.27, no.2, pp.62-68, **1950**.
93. **Stewart B.A., Summer M.E.**, “Soil crusting: chemical and physical process”, B.A. Stewart and M.E. Summer, Eds., Lewis Publisher, Boca Raton, p.384, **1992**.
94. **Stratton J.A.**, “Electromagnetic Theory”, McGraw-Hill Book Company, p.615, New York, **1941**.
95. **Thapa P.B., Dhital M.R.**, “Landslide and debris flows of 19-21 July 1993 in the Agra Khola Watershed of Central Nepal”, *J. Nepal Geol. Soc.*, 21:5-20, **2000**.
96. **Topp G.C., Davis J.L.**, “Measurement of soil-water content using time-domain reflectometry (Tdr) – A field-evaluation”, *Soil Sci Soc Am J*, vol.49, no.1, pp.19-24, **1985**.
97. **Topp G.C.**, Davis J.L., Annan A.P., “Electromagnetic Determination of Soil Water Content: Measurements in Coaxial Transmission Lines”, *Water Resources Research*, vol.16, no.3, pp.574-582, **1980**.
98. **Touzi R., Lopes A.**, “The principle of speckle filtering in polarimetric SAR imagery”, *IEEE Transactions on Geoscience and Remote Sensing*, vol.32, no.5, pp.1110-1114, **1994**.
99. **Ulaby F.T.**, Dobson M.C., Bradley G.A., “Radar reflectivity of bare and vegetation-covered soil”, *Advance in Space Research*, vol.1, no.10, pp.91-104, **1981-B**.
100. **Ulaby F.T.**, Moore R.K., Fung A.K., “Microwave remote sensing active and passive volume II – Surface Scattering and Emission Theory”, 1<sup>st</sup> Edition, Ds. Simonett, Ed. Addison-Wesley Publishing Company, Inc., Reading, Massachusetts 01867, p.1064, USA, **1982**.
101. **Ulaby F.T.**, Moore R.K., Fung A.K., “Microwave remote sensing active and passive Volume I – Fundamentals and Radiometry”, 1<sup>st</sup> Edition, D.S.Simonett, Ed., Addison-Wesley Publishing Company, Inc. Reading, Massachusetts 01867, USA, p.456, **1981-A**.
102. **Ulaby F.T.**, Moore R.K., Fung A.K., “Microwave remote sensing active and passive Volume III – From Theory to Applications”, D.S.Simonett, Ed., Artech House, Inc. Norwood, Massachusetts 02062, USA, p.2136, **1986**.

103. **Von Hippel A.**, “Dielectric and waves”, New ed., A.S. Labounsky, Ed. Artech House, p.284, Boston, **1995**.
104. **Wang H.P.**, Ouchi K., Watanabe M., Shimada M., Tadono T., Rosenqvist A., Romshoo S.A., Matsuoka M., Moriyama T., Uratsuka S., “In search of the statistical properties of high-resolution polarimetric SAR data for the measurements of forest biomass beyond the RCS saturation limits”, *IEEE Geoscience and Remote Sensing Letters*, vol.3, no.4, pp.495-499, **2006**.
105. **Whalley W.R.**, “Considerations on the use of time-domain reflectometry (TDR) for measuring soil water content”, **Journal of Soil Science**, vol.44, no.1, pp.1-9, **1993**.
106. **Windisch E.J.**, “The hydraulics problem in slope stability analysis”, *Can. Geotech. J.*, 28(6):903-909, **1991**.
107. **Wobschall D.**, “A Theory of the Complex Dielectric Permittivity of Soil Containing Water: The Semidisperse Model”, *IEEE Transactions on Geoscience and Remote Sensing*, vol.15, no.1, pp.49-58, 1977.
108. **Zhenghao S.**, Fung K.B., “A comparison of digital speckle filters”, *Geoscience and Remote Sensing Symposium. IGARSS '94. Surface and Atmospheric Remote Sensing: Technologies, Data Analysis and Interpretation*, International, vol.4, pp.2129-2133, August 8-12, **1994**.